Pore-Level Interpretation of Methane Hydrate Growth and Dissociation with Deionized and Saline Water

Master Thesis in Reservoir Physics

By
Eirik Iden

Department of Physics and Technology
University of Bergen

May 2017

Abstract

Natural gas hydrates are solid crystalline compounds composed of water and gas molecules, located in vast amounts around the world, in subsurface permafrost and oceanic environments. With an increasing demand of energy worldwide, methane production from natural gas hydrates may play an important role to ensure future energy sustainability. Research on methane hydrate on pore-level may contribute to a greater understanding of the fundamentals and characteristics of hydrate formation and production schemes. This thesis presents a series of experiments conducted in a two-dimensional synthetic micromodel. The main objective of the experiments was to determine and interpret methane hydrate characteristics on pore-level using microscopy, during hydrate formation and dissociation with different water solutions. In the experiments, deionized water and saline water of 2.0, 3.5 and 5.0 wt% sodium chloride (NaCl) were used. The saturation changes for water, gas and hydrate were estimated to determine water and gas behavior in each experiment.

There were conducted 16 successful hydrate formations, where ten were primary formations and six were secondary formations. During primary hydrate formation, the temperature and pressure values were fixed, and hydrate growth was induced by forcing agitation on water and gas in the micromodel. The temperature was in the range 1.0-4.1°C, and the pressure was in the range 80.0-110.0 bar. During secondary hydrate formation, the temperature was approximately 4.0°C, and the pressure was increased to above the hydrate stability line. Primary hydrate formation was faster and more homogeneous than secondary hydrate formation, independent of water salinity. Hydrate growth occurred mainly within the gas, but was one time observed to occur in the water phase. Initial hydrate growth occurred on the water-gas interface at the pore walls and continued to grow in the gas towards the pore center. Salt was the limiting factor when hydrate was being formed with saline water of 3.5 wt% NaCl and higher, and in these experiments hydrate required greater driving forces to form. The hydrate formation rate was observed to decrease with increasing salinity.

There were performed 13 controlled hydrate dissociations by either pressure reduction or thermal stimulation. The patterns of hydrate dissociation by depressurization were the opposite of the patterns of hydrate dissociation by thermal stimulation. When hydrate was dissociated by depressurization, hydrate generally dissociated from the center of the pores towards the water-gas interface at the pore walls. Further dissociation was favored when the hydrate was in direct contact with free gas bubbles. When hydrate was dissociated by thermal stimulation, hydrate generally dissociated from the water-gas interface at the pore walls towards the center of the pores. The experiments showed that with high connectivity between the hydrates, hydrate dissociated more uniformly. The saturation profiles gained from images showed that dissociation by thermal stimulation was more uniform than dissociation by pressure reduction.

Hydrate was dissociated by reducing the pressure in increments of 0.7 bar or by increasing the temperature in increments of 0.1°C. The stepwise pressure and temperature technique showed that hydrate dissociated over a range of pressure and temperature steps. The required number of pressure and temperature steps from initial hydrate dissociation to complete hydrate dissociation, increased with increased salinity. This is believed to be due to a continuous decrease in salinity in the local water phases when pure water was liberated from the dissociating hydrate structure. The hydrate phase became more stable towards the low-saline water phases, and as a consequence of pore water freshening, the hydrate phase required lower pressures and higher temperatures to dissociate. Local hydrate saturations within the gas and isolated hydrate saturations in the pore space were observed to remain, while the surrounding hydrate dissociated. These local hydrate saturations seemed to become stable toward local low-saline water, and are believed to be the main reason why dissociation was prolonged for saline water.

Acknowledgments

First of all I would like to express my gratitude to my supervisor Associate Professor Geir Ersland for providing such an interesting topic for my thesis. Thank you for giving me valuable input during the process and for both great scientific and trivial discussions. Your good spirits and positive and accommodating manner have been a great encouragement. Likewise, I am thankful to Professor Arne Graue for facilitating my work at the Department of Physics and Technology, and to Associate Professor Martin Fernø and Dr. Marianna Steinsbø for giving good and constructive experimental advice.

I would also like to thank PhD candidate Stian Almenningen for being more than helpful for the last year. Your guidance in the experimental work and useful advice on this topic have been both invaluable as well as timesaving. Thank you.

Thanks too, to the kind personnel at the mechanical workshop for efficiently assisting in fixing damaged equipment.

Further, I would like to thank my fellow students for a friendly and productive working environment. The five last years have been memorable with much laughter both on and off topic.

Finally, I would like to thank my family and friends for the unconditional support. I would like to give special thanks to my mother Ellen Kavli Iden and Dr. scient. Eirik Hauger for your contributions to the thesis, and to Maren Skibeli Joa for always believing in me.

Table of Contents

Introduction

The energy from natural gas hydrates is potentially one of the most important resources in the future. Gas resources from natural gas hydrates have been estimated to be in the range of 10^{13} m^3, which is double the amount of conventional fossil fuels (i.e. oil, gas and coal) found in the world (Kvenvolden, 1988). It is estimated that 97% are found in ocean sediments, while only 3% are on land and almost exclusively in areas with thick permafrost (Makogon, 2010). The gas stored in 1 m^3 solid hydrate expands to 164 m^3 of gas and 0.8 m^3 of water at standard conditions. Methane is known to be the cleanest fossil fuel, only leaving carbon dioxide and water on combustion. It is predicted that the energy demand worldwide will increase with 48% from 2012 to 2040 (U.S. Energy Information Administration, 2016). Natural gas hydrates is potentially a new energy resource, and for this reason the interest in natural gas hydrate has increased the past decades, especially in countries like Japan, India, Taiwan and China, nations seeking to be self-sustained in energy with natural occurrences of natural gas hydrates in subsea sediments offshore on continental margins.

Natural gas hydrates are solid crystalline compounds composed of water and gas molecules existing at high pressures and low temperatures. Water molecules are interconnected through hydrogen-bonds creating a cage like structure which can encapsulate gas molecules that stabilize the structure. The gas molecules are often referred to as guest molecules or hydrate formers, and are typically methane, ethane and carbon dioxide, where methane is the most abundant hydrate former. Natural gas hydrates exist all over the world and are typically located in permafrost regions and marine environments where the pressure and temperature conditions are thermodynamic stabile for hydrate.

At the University of Bergen, Department of Physics and Technology a research project has been initiated to increase the knowledge of methods for gas hydrate extraction. The purpose of this study is to investigate methane (CH_4) hydrate formation and dissociation patterns as a function of salinity at pore scale, and compare it against hydrate formation and dissociation with deionized water. Three different salinities have been used during the experiments, 2.0, 3.5 and 5.0 wt%. Salt is a hydrate inhibitor and will affect the stability conditions of gas hydrate, and it is expected that hydrate will dissociate at higher pressures and lower temperatures with increasing salinity. The effects of decreased salinity during dissociation are studied on pore scale to identify dissociation kinetics. The hydrate stability will shift towards more stable conditions when hydrates start to dissociate, and the effects of pore-water freshening on further hydrate dissociation are one of the key questions that this work address. Hydrate dissociation has been performed by pressure depletion and thermal stimulation. Since pressure depletion is considered as the most promising production technique, it has been placed more emphasis on this method during the experiments. Understanding the processes of formation and dissociation and how fluids are mobilized on a pore scale can give essential knowledge for development of gas hydrates as a resource.

1 Fundamentals

1.1 Natural gas hydrates

1.1.1 The water molecule

The water molecule consists of one oxygen atom and two hydrogen atoms (H-O-H), where the oxygen atom is the vertex for the two hydrogen atoms forming an angle of 104.5° between the two hydrogen atoms. With its eight electrons the oxygen atom has the electronic configuration $1s^2 2s^2 2p^4$ and is missing two electrons to complete the valence shell. The hydrogen atom has one electron with the electronic configuration $1s^1$. Thus, the two hydrogen atoms create covalent bonds with the oxygen atom completing the valence shell for the oxygen atom. Due to the difference in electronegativity between hydrogen and oxygen atoms, the electron pairs in each covalent bond will lie closer to the oxygen atom. The electronegativity for oxygen and hydrogen is 3,44 and 2,20, respectively (Allred and Rochow, 1958). Each water molecule has two negative charges, created by two lone pairs of electrons, and two positive charges, created by the sharing of electrons with protons. The end result is a permanent polar water molecule with a partial positive charge between the hydrogen atoms and a partial negative charge from the oxygen atom (Sloan, 2008). This charge distribution contributes to hydrogen bonding, where the positive pole on one water molecule is attracted to a negative pole on another water molecule. A single water molecule can create four hydrogen bonds, either by donating two hydrogen atoms or accepting two bonds from the lone pair electrons surrounding the oxygen, as shown in Figure 1.

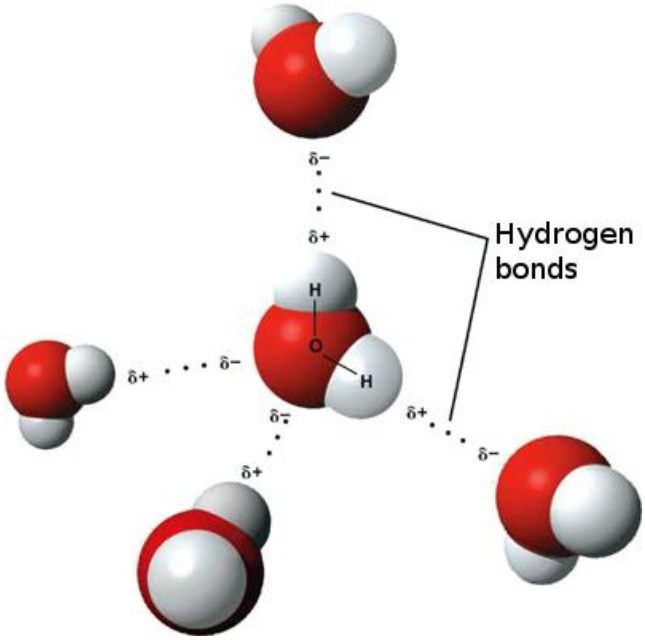

Figure 1: Hydrogen bonding creating a tetrahedral (109,5°) arrangement around the central water molecule (WordPress, 2011). The distance between the neighbor oxygen in the crystal is 2.74 Å at 0 K.

The strength of a hydrogen bond (ca. 5 kcal/mol) is stronger than a typical van der Waals bond (ca. 0.3kcal/mol) and 20 times weaker than a covalent chemical bond (ca. 100 kcal/mol) (Stillinger, 1980). Because the energy required for breaking a covalent bond is substantially greater than the energy required for breaking a hydrogen bond, only hydrogen bonds are considered between neighboring

molecules when hydrates are being formed or dissociated. Van der Waals bonds are insignificant relative to hydrogen bonds.

Hydrate is often compared to ice due their similar properties. The most common form of ice is hexagonal ice, where each water molecule is hydrogen bonded to four other water molecules, forming a tetrahedral arrangement with an O-O-O angle of 109,5°. The tetrahedral structure forms nonplanar puckered hexagonal rings, rather than planar sheets. In comparison, hydrate structures consist of about 85% water on a molecular basis with similar tetrahedral arrangement as ice. Studies show that hydrate hydrogen bonds average only 1% longer than those in ice and that the tetrahedral angles only differ by 3.7° for structure I and 3.0° for structure II (Sloan, 2008). The difference in bulk and shear velocity for ice and hydrates is small, making it hard to distinguish between the two facies during seismic interpretations. The mechanical strength in hydrate is 20 times stronger than the mechanical strength in ice, which increases with decreasing temperatures (Durham et al., 2003). The thermal conductivity is five times lower for hydrates than the thermal conductivity for ice, because guest molecules colliding within water cavities weaken the hydrogen bonds.

1.1.2 Hydrate structures

Natural gas hydrates are built up with hydrogen-bonded water cavities that encage guest molecules in order to stabilize. Depending on the type of guest molecule and polyhedral, different well-defined hydrate structures will form, as illustrated in Figure 2. The basic building block for most hydrates is the pentagonal dodecahedron with its twelve pentagonal faces, denoted 5^{12}. Another cavity is the tetrakaidecahedron which has twelve pentagonal and two hexagonal faces denoted $5^{12}6^2$. Structure I (sI) is made up of two small (5^{12}) cavities and six large ($5^{12}6^2$) cavities, where the vertices are linked together (Sloan, 2003). This structure is the most common hydrate in nature, and has 46 water molecules per unit cell. If the small cavities are joined together through the 5^{12} faces the hexakaidecahedral cavity is formed. This cavity consists of twelve pentagonal faces and four hexagonal faces denoted $5^{12}6^4$. Structure II (sII) is made up of 16 small cavities (5^{12}) and eight large cavities ($5^{12}6^4$) and has 136 water molecules per unit cell. Structure H (sH) is made up of three small cavities (5^{12}), two intermediate cavities ($4^35^66^3$) and one large cavity ($5^{23}6^8$) and has 30 water molecules per unit cell. Because sH is built up with intermediate cavities, it is considered a more complex structure, which requires two different sizes of molecules to stabilize. The reason the 5^{12} building block joins together with the other cavities, is that it cannot fill its own space within without causing hydrogen bond strain resulting in a collapse, which is a key factor for the forming of such structures (Sloan, 2003). Specifications for each hydrate structure can be found in Table 1.

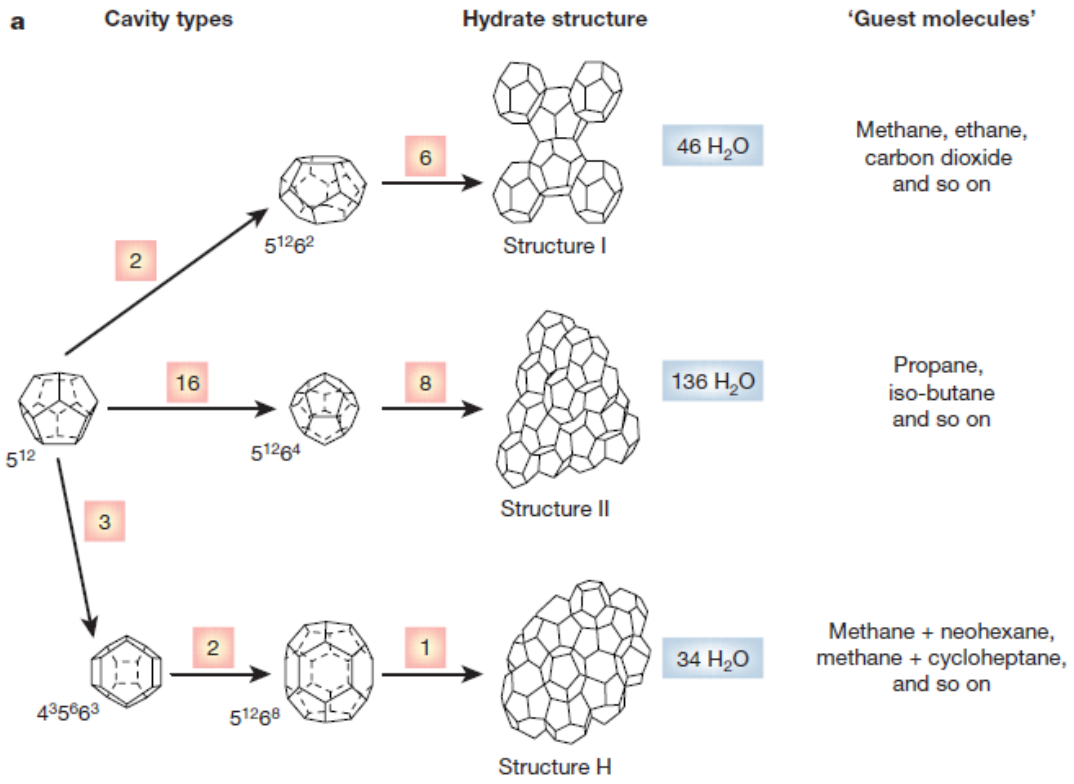

Figure 2: An overview of the different cavity types that combine to create the hydrate structures sI, sII and s, and their respective stabilizing guest molecules (Sloan, 2003).

Table 1: Hydrate structures and their specifications: cavity, description, number of cavities per unit cell, average cavity radius, coordination number and number of waters per unit cell. The coordination number refers to the number of oxygens at the periphery of each cavity. Average cavity radiuses for structure H are estimated from geometric models. (Sloan, 2003)

Hydrate crystal structure	**I**		**II**		**H**		
Cavity	Small	Large	Small	Large	Small	Medium	Large
Description	5^{12}	$5^{12}6^2$	5^{12}	$5^{12}6^4$	5^{12}	$4^3 5^6 6^3$	$5^{12}6^8$
Cavities per unit cell	2	6	16	8	3	2	1
Average cavity radius (Å)	3.95	4.33	3.91	4.73	3.91	4.06	5.71
Coordination number	20	24	20	28	20	20	36
Waters per unit cell	46		136		34		

1.1.3 Hydrate guest molecules

Natural gas hydrates will only form when there is a presence of guest molecules, trapped in the water cavities. Van der Waals interactions between the guest molecule and cavity prevent the cavity from collapsing. For this reason, the chemical composition and size of the guest molecule have an impact on the stability of the structure. The guest molecule has to be small enough to fit into the cavity, but at the same time large enough to stabilize the cavity. The ratio of molecular to cavity diameter for the molecule has to lie between 0.76 to 1.0 (Sloan, 2008). The hydrate will be more stable for stronger guest-water attractions (Kvamme, 2016). Figure 3 illustrates the different simple hydrate structures (only one guest molecule) formed by the various gas molecules for structure I and structure II. No hydrates are formed if the gas molecule has a radius smaller than 3.5Å or higher than

7.5 Å. Gas molecules between 4.2-6 Å can stabilize structure I hydrates, while gas molecules between 3.5-4.2 Å and between 6-7 Å can stabilize structure II hydrates.

Methane (CH_4), with an average radius of 4.36 Å, can stabilize the small cavities and occupy the large cavities of structure I. The large cavity in structure II is too large for methane to stabilize it, so methane will always form structure I. Ethane (C_2H_6), hydrogen sulfide (H_2S) and carbon dioxide (CO_2) are other natural gases that form structure I. Structure II can be formed by gas molecules such as nitrogen (N_2), propane (C_3H_8) and isobutane (C_4H_{10}). Propane (C_3H_8) and isobutane (C_4H_{10}) are too large to enter the small cavities in structure II, so smaller gas molecules such as methane and ethane will aid them, creating binary guest mixtures (Sloan, 2003).

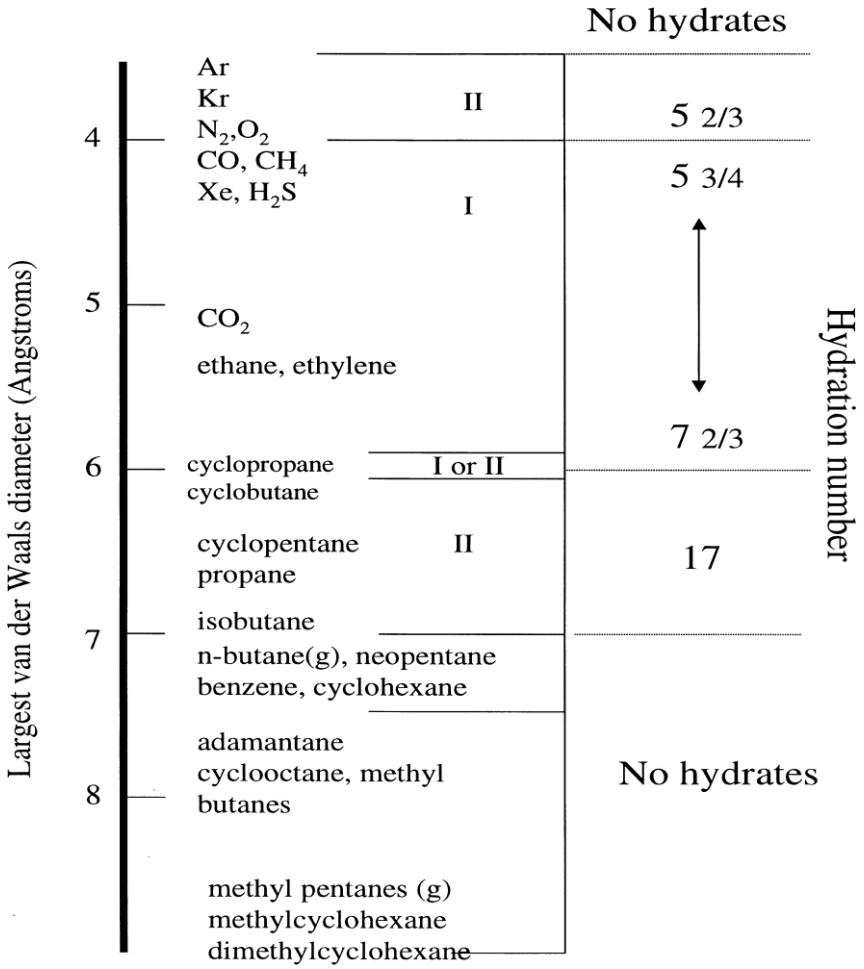

Figure 3: A correlation between the guest size (Å), structure (sI and sII) for the most common single guests (Ripmeester, 2000)

With respect to the chemical composition of the guest molecule, two classifications have been used. Jeffrey and McMullan (1967) proposed that the guest molecules were defined by four groups: 1) hydrophobic compounds, 2) water-soluble acid gases, 3) water soluble polar compounds or 4) water soluble ternary or quaternary alkylammonium salts. The other classification used is a combination of chemical composition and size where the guest molecules formed is one of the following: 1) mixed hydrate, 2) double hydrate, 3) help-gas hydrate or 4) simple hydrate (Von Stackelberg, 1956). Methane is a hydrophobic compound and will mostly be classified as a simple hydrate, as methane hydrates are more abundant in nature. Structure H will always be defined as a double hydrate as it needs two different guest molecules to stabilize.

1.1.4 Hydrate stability conditions

In general, a basic thermodynamic driving force is required for formation to commence, which for natural gas hydrates are low temperatures and high pressures. The range may vary depending on type of guest molecule present in the hydrate. The temperature and pressure range has to be to the left of the equilibrium curve for hydrate formation to occur. In this thesis methane hydrate formation and dissociation was studied with respect to different salinities. Salt-ions works as a hydrate inhibitor (discussed more in detail in section 1.1.8), moving the equilibrium curve further to the left, as illustrated in Figure 4. With higher salinities, the smaller the hydrate formation zone becomes (Makogon, 2010).

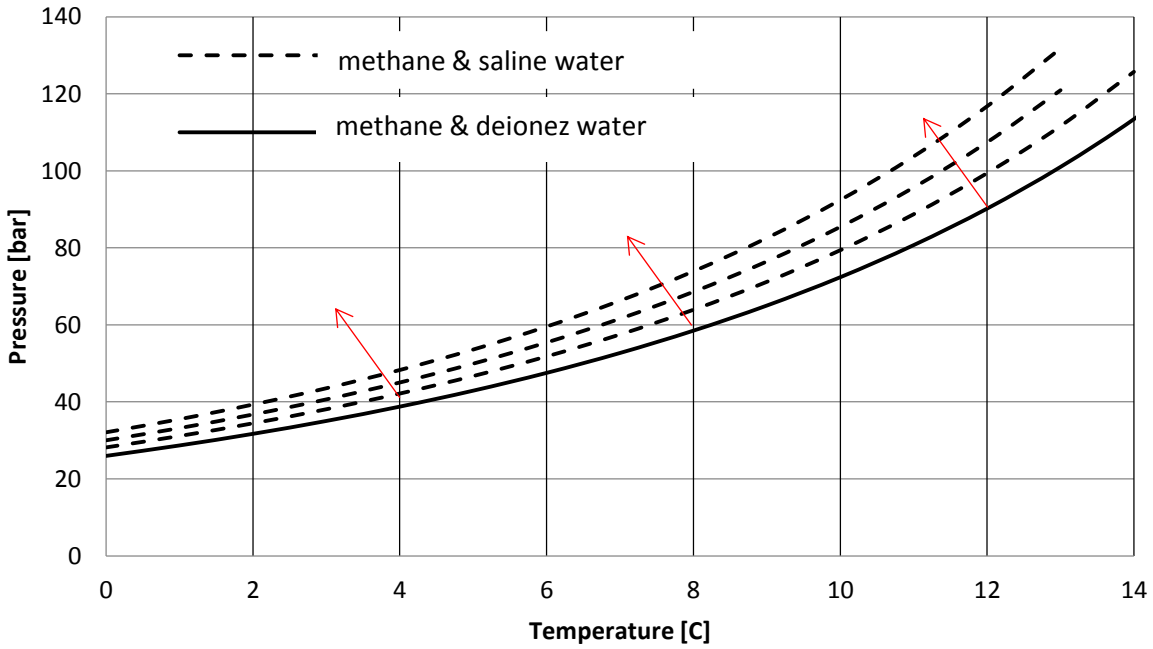

Figure 4: Pressure vs. temperature for methane hydrate stability conditions for salinities 0, 2.0, 3.5 and 5.0 wt% NaCl in bulk phase created by CSMGem (Colorado School of Mines, 2015). Increased salinity shifts the hydrate line upwards.

1.1.5 Hydrate kinetics

Hydrate kinetics is considered the most challenging aspect in understanding the nature of hydrates, and key factors for this are hydrate formation and dissociation.

Hydrate Formation

Hydrate formation will mostly occur on the water-gas interface because the hydrate component concentrations greatly exceed the mutual fluid solubility (Sloan, 2003). Figure 5 illustrates how the hydrate formation process is influenced by gas consumption over time. The hydrate formation process can be divided into nucleation, induction time and growth.

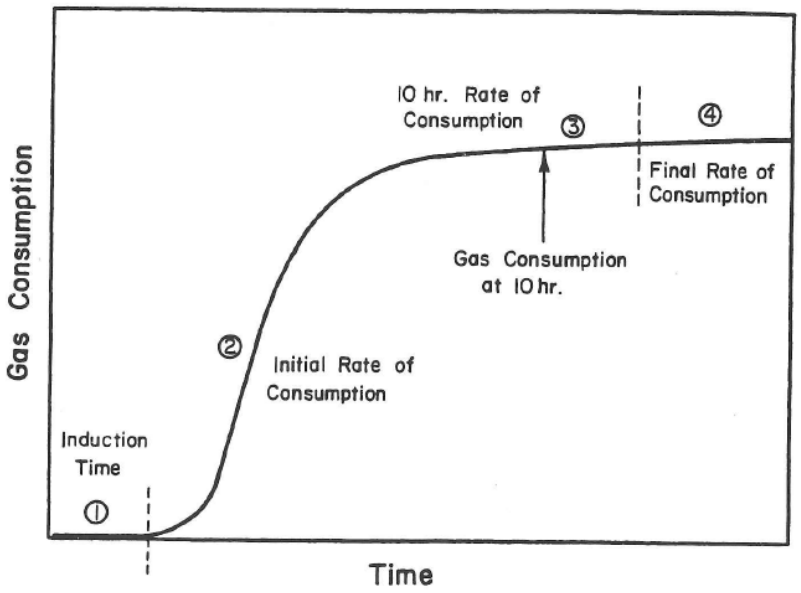

Figure 5: An illustration of gas consumption vs. time for hydrate formation. Pressure and temperature are held constant during the process (Sloan, 2008).

Nucleation

Hydrate nucleation is the process where small hydrate crystals grow and disperse in an attempt to achieve critical size for continued growth, and this process occurs in the left corner of Figure 5. The two basic concepts of nucleation are homogeneous nucleation (HON) and heterogeneous nucleation (HEN). HON is a three-dimensional solidification process in the absence of impurities where many molecules collide with each other. Since there are too many molecules in such a process, the collisions can happen simultaneously, and clusters may increase in sequences until the critical cluster size is reached. Before achieving the critical size, the clusters may either grow or shrink as a result of density and composition fluctuations (Sloan, 2008). Therefore the nucleation process can be interpreted by the minimization of Gibbs free energy, which is a competition between the surface excess free energy and the volume excess free energy (Kvamme, 2016), expressed:

$$\Delta G = \Delta G^{surface} + \Delta G^{phase\ trans.} = 4\pi r^2\gamma + \frac{4}{3}\pi r^3 \rho_N^H \Delta g^{phase\ trans.} \leq 0 \tag{1.1}$$

where ΔG is the total excess free energy, γ is the interfacial tension [J/m^2], r is the crystal radius [m], ρ_N^H is the molecular density [mole/m^3] and $\Delta g^{phase\ trans.}$ is the intensive change in Gibbs free energy related to the phase transition [J/mole]. If the free change of phase transition overcomes the penalty from creation of new surface area, the critical size may be attained and monotonic growth occurs. By differentiating equation 1.1 and setting the result to zero the critical Gibbs free energy, ΔG_{crit}, can be obtained:

$$\Delta G_{crit} = 4\pi r_c^2/3 \tag{1.2}$$

where r_c is the critical radius, which represents a minimum size required for the hydrate crystal to grow. Below the critical radius, a new crystal may either grow or re-dissolve. The critical Gibbs free energy represents the energy that must be beaten to form a cluster for critical size.

In reality, it is impossible to have a solution completely free of impurities, so in a usual case the nucleation is heterogeneous. HEN takes into account the presence of a foreign body or surface, and is a two-dimensional solidification process. Considering the aspect of free energy, a hydrate nucleus is more likely to grow on a two-dimensional surface than on a three-dimensional surface-free volume

of water. Because of the presence of a foreign body, the contact angle between the hydrate crystal and the surface has to be considered, and equation (1.2) is therefore modified to:

$$\Delta G'_{crit} = \phi \Delta G_{crit} \tag{1.3}$$

where ϕ is a fraction between 0 and 1 related to the contact angle, causing the critical Gibbs free energy for HEN to be smaller or equal to HON. Therefore, HEN is more likely to occur in nature (Sloan, 2008).

Even though HEN is more common, Englezos et al. (1987) observed that if a solution reached uniform supersaturation before the appearance of the nuclei, nucleation can occur everywhere in the liquid phase. This implies that HON is a possibility, and that hydrate formation is not necessarily restricted to the water-gas interface. Other nucleation hypotheses are proposed in theory, which are discussed in more detail in section 1.1.7.

Induction time

Induction time, marked as 1 in Figure 5, can be defined as the period from hydrate stability until the appearance of detectable hydrate clusters, capable of massive growth (Kashchiev and Firoozabadi, 2003). Whereas hydrate nucleation is a microscopic event, the induction time is a macroscopic phenomenon even though hydrate nucleation will dominate much of the timespan. Hydrate will most likely not form during the induction time because of metastability. Because the induction time may vary from minutes to hours, even though the system is kept constant, it is considered a stochastic event. The time delay/difference is the result of the rearrangement of the hydrate interfaces and the rearrangement throughout the hydrate, as well as the effects from foreign particles. Englezos et al. (1987) observed that at large driving forces the induction time was shorter, while at small driving forces the induction time was longer.

Growth

Hydrate growth will commence after the hydrate crystal nucleation and induction time. The growth period is governed by hydrate kinetics coupled with mass transfer and heat transfer (Englezos et al., 1987). The growth rate is highly dependent on the availability of water and guest molecule, as can be seen in Figure 5. Initially, the growth rate is high because the density of the gas molecules is higher than the density in the vapor phase. After a given time, the lack of either water or gas molecules will cause the growth rate to decrease, and eventually cease of. As hydrate formation is an exothermic process, local temperature changes caused by hydrate growth may counteract the growth.

Hydrate dissociation

Hydrate dissociation is an endothermic process, and can be performed by removing one of the hydrate components (hydrogen bonds and/or van der Waals interaction forces). Depressurization, thermal stimulation, chemical additives, or a combination of these, are different methods to dissociate hydrate. Depressurization and thermal stimulation both move the hydrate outside the hydrate stability zone, while chemical additives move the equilibrium curve (Kvamme, 2016). Dissociation is a key factor to produce hydrates, and in this thesis a combination of thermal stimulation and depressurization will be used to visualize the hydrate behavior.

1.1.6 Driving forces for nucleation

The driving force for hydrate nucleation is a key component to understand the hydrate formation process. Several driving forces partake in the nucleation process, but in general it can be described as the total change in Gibbs free energy expressed:

$$\Delta g^{exp} = \Delta g^{rx} - \Delta g^{pd} \tag{1.4}$$

where Δg^{exp} is the experimental molar Gibbs free energy, a function of temperature T, pressure P, chemical potensial μ and fugacity f, and Δg^{rx} and Δg^{pd} is the molar Gibbs free energy for the reactants and products, respectively.

Figure 6 represents a hydrate formation as a function of subcooling with an equilibrium curve (AB) and the supersaturation curve (CD). In the region to the right of curve AB the driving force is low and no nucleation will occur. Following the line PS, moving into the metastable region, the driving force is increased and nucleation may or may not arise. If a system is within the labile region, to the left of the curve CD the driving force is high and there is a high probability of hydrate nucleation.

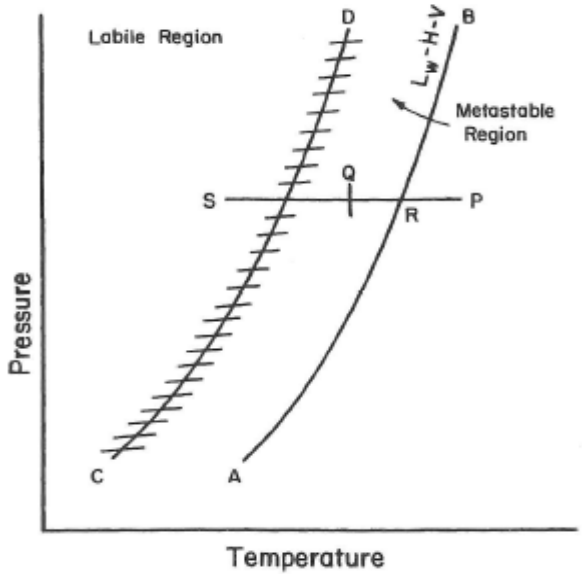

Figure 6: Pressure vs. temperature for hydrate formation, represented with hydrate stability regions (Sloan, 2008).

1.1.7 Hydrate nucleation theories

Due to the uncertainty regarding hydrate nucleation, several theories have been proposed to explain the mechanisms that contribute to the nucleation process. The main focus is on the interactions on molecular level on the vapor-liquid interface. Labile cluster nucleation, nucleation at the interface, and local structuring nucleation are three hypotheses that are of interest and will be discussed further (Sloan, 2008).

The labile cluster nucleation hypothesis is based on the idea that clusters of water with guest molecules grow to achieve critical radius and eventually form hydrates. The steps of the model are illustrated in Figure 7, where (A) pure water exists without guests occupying its cavities and in the form of labile ring structures of pentamers and hexamers. (B) By dissolving guest molecules in the pure water, labile clusters form which again combines to form unit cells. (C) The labile clusters agglomerate either on the liquid or the vapor side of the interface, creating further disorder. (D) At last, when the size of the agglomerate reaches a critical size, primary nucleation and growth begins.

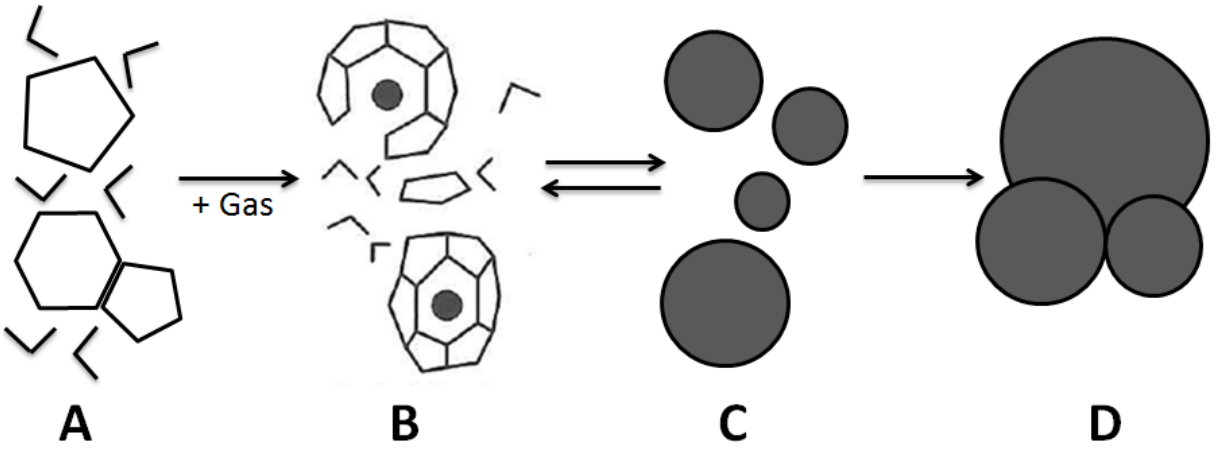

Figure 7: Labile cluster nucleation hypothesis, modified from (Sloan, 2008). A) Initial condition: Pressure and temperature in hydrate forming region, but no labile clusters. B) Labile clusters: Formation of labile clusters. C) Agglomeration: Labile clusters agglomerate by sharing faces. D) Primary nucleation and growth: Growth commences.

The hypothesis is developed around two key fundamentals:

- Clusters combine to form unit cells dependent on the coordination number (number of water molecules surrounding a guest molecule). Clusters with coordination number 20 and 24 are required for 5^{12} and $5^{12}6^2$ cavities, forming structure I. To form structure II, the 5^{12} and $5^{12}6^4$ cavities require gas components with coordination number 20 and 28, respectively.
- Nucleation may commence for either of the structures when the labile clusters are available for both types of coordination numbers. However, nucleation will not occur if the water is occupied by clusters of only one coordination number. In such a case, the hydrogen bonds have to be rearranged, transforming the clusters into the correct fit.

The nucleation at the interface hypothesis is based on the idea that nucleation takes place towards the vapor interface through adsorption characteristics. As gas molecules are transported to the water-gas interface, they get adsorbed on the water surface. The water cavities do not have to be completed before the adsorption can take place. Further, the gas migrates to a suitable location for adsorption through surface diffusion where water molecules first form partial cages around the gas before completing the cages. At this stage labile clusters agglomerate on the vapor side of the surface until a critical size is reached and growth occurs. The progress from small water clusters to large hydrate masses is a constant battle between each cluster, where some agglomerate and others disintegrate, fighting to achieve critical size (Sloan, 2008). Simulations performed by Kvamme (2002) estimate that the growth rate is twice as large on the vapor surface as on the liquid surface.

The local structuring nucleation hypothesis looks at the nucleation mechanisms of gas hydrates in the bulk water phase by use of molecular simulations. The though behind the hypothesis is that guest molecules arrange themselves in a configuration similar to clathrate hydrate because of thermal fluctuation. The stochastic process causes the water molecules around local guest molecules to be perturbed compared to that in the bulk water phase. If the number of local guest molecules is high enough, a critical nucleus can be attained, and the hydrate cluster may grow.

Even though the hydrate nucleation theories mentioned above have been studied for several years, the nucleation and formation process remains experimentally unverified today. The stochastic and microscopic nature of the process makes it difficult to validate, so it may be plausible that a “correct” method is a combination of the different theories.

1.1.8 Hydrate inhibition

Hydrate inhibition can prevent/control hydrate formation and dissociation, and may be divided into thermodynamic inhibitors, kinetic inhibitors and anti-agglomerates.

Thermodynamic inhibitors alter the equilibrium conditions (see Figure 4 as an example), for hydrate formation by reducing the chemical potential. Water molecules will always favor the phase that has the lowest chemical potentials, so higher pressures and lower temperatures are required for hydrate formation. Alcohols, glycols and salts are the most common thermodynamic inhibitors. Alcohols and glycols lower the water activity as (i) a direct consequence of hydrogen bonding with the water molecules, and by (ii) organizing the water into solvent clusters, which compete with the guest molecules. Salts interact with the water molecule dipoles with stronger Coulombic bonds than both hydrogen bonds and the van der Waals forces, resulting in favorable bonding between the water molecules and salt ions rather than hydrate structures. Salts also decrease the solubility of potential hydrate guest molecules, known as “salting out” (Sloan, 2008). Consequently, more subcooling is required to overcome structural changes and cause hydrate formation. The salt used in this thesis is sodium chloride (NaCl) (>99.5%), which is a well-known thermodynamic inhibitor.

Kinetic inhibitors and *anti-agglomerates* are both inhibitors in form of polymers that can delay and ultimately prevent hydrate formation (Kvamme, 2016). Kinetic inhibitors are polymers of low molecular weight, which infiltrate the liquid phase creating space between the water molecules denying them to cluster together. This is known as sterical hindrance. Anti-agglomerates are polymers with attached groups that are good hydrate formers.

1.1.9 The “Memory Effect”

The “memory effect” is an expression used in relation to the thermal history of hydrates. The assumption is that hydrates keep a memory of their structure in the free water when melted at *moderate* temperatures at a given pressure. Therefore, a hydrate system that has already been formed and dissociated will regenerate hydrate more easily than a system with no previous hydrate history. However, the memory effect can perish if the hydrate system is heated sufficiently above the hydrate formation conditions. Two hypotheses are proposed as a reason for the memory effect (Sloan 2008):

- The hydrate structure remains as a residual structure of partial hydrate cages or persistent hydrate crystallites in the solution.
- Dissolved gas remains in the solution.

The induction time and the nucleation process have been studied in relation to the memory effect. Wu and Zhang (2010) created hydrates in several tests for the same system and observed that the induction time and the nucleation pressure decreased for each test due to the presence of residual structures, which acted as seeds for further formation. Ohmura et al. (2003) observed that if the system had a similar thermal history, the induction time varied for each formation due to the stochastic nature of hydrates. However, the induction time increased with an increase of the highest temperature at which the system was kept in advance. This can validate that the memory effect can be destroyed if the system is kept too long out of the hydrate formation region. For the purpose of this thesis, it is important that the system is cleaned between the experiments with different salinities so that the system is not influenced by previous water-gas conditions.

1.2 Natural gas hydrates in nature

1.2.1 Origin of gas hydrates

Natural gas hydrates are found worldwide in regions where the pressure and temperature conditions are thermodynamic stabile for hydrate, as illustrated in Figure 8. More than 90 sites have been directly or indirectly identified to contain natural gas hydrate deposits (Hester and Brewer, 2009). Direct identification refers to deposits that have been sampled from ocean drilling and remote-operated vehicle expeditions, while indirect identification refers to mainly seismic data (bottom simulator reflector). Makogon (2010) stated that as many as 230 natural gas hydrate deposits have been discovered. Of the natural gas hydrate deposits, it is estimated that 97% are found in ocean sediments, while only 3% are on land and almost exclusively in areas with thick permafrost.

Natural gas hydrate is either biogenic or thermogenic. Biogenic hydrate is formed from anaerobic bacterial decomposition of organic matter, while thermogenic hydrate originates from thermal cracking of organic material. Based on today's mapping from approximately 80 years of studies, it is estimated that 99% of the gas hydrates in nature are biogenic (Kvamme, 2016). Biogenic hydrate mainly creates methane hydrate, making it the most abundant in nature.

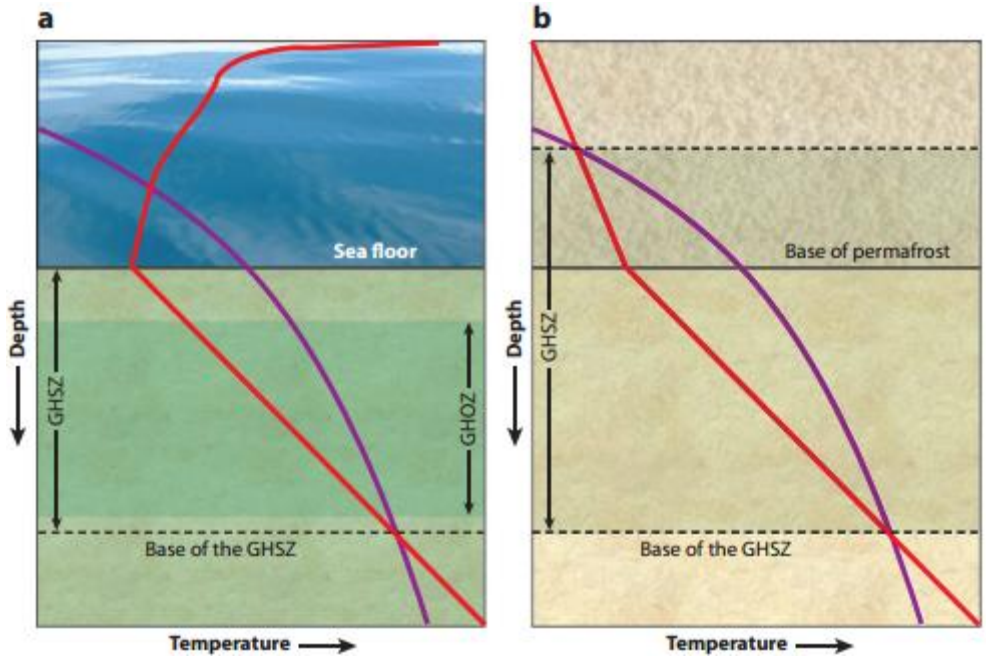

Figure 8: Gas hydrate stability zone (GHSZ) for (a) marine and (b) permafrost settings. The red and purple line represents the ambient temperature profile and the hydrate stability curve as a function of depth, respectively. (Hester and Brewer, 2009)

For marine systems, the hydrate stability zone (GHSZ) typically lays hundreds of meters below the sea floor with sea water above ranging from 300-600 m, and with a general temperature range from 2 to 20°C. Hydrate formation is limited to the gas hydrate occurrence zone (GHOZ), which is caused by sulfate reduction and anaerobic oxidation of methane just below the sea floor, and this limitation reduces the availability of methane. The GHSZ for permafrost systems typically exists at around 100-300 m depth and may extend hundreds of meters below the base of permafrost, where the general temperature ranges from -10 to 20°C. Under these conditions, a two-phase ice + gas equilibrium is present until pressures are great enough to allow for hydrate formation. The GHSZ extends through the base of permafrost until temperatures exceed hydrate stability, resulting in a gas + liquid two-phase region (Hester and Brewer, 2009).

Even though natural gas hydrate is widespread around the world and only occurs in sediments characterized by specific pressure and temperature conditions, the deposits are not necessarily ubiquitous within the hydrate stability zone (Ruppel, 2011). Lack of sufficient gas or free water in sediments can limit the gas hydrate formation. Also, most of the gas trapped in hydrates are located in low permeable and low saturation (<10% of pore volume) marine sediments, and is near impossible to detect without drilling.

1.2.2 Classification of gas hydrate deposits

To evaluate natural gas hydrate production schemes, Moridis and Collett (2003) proposed a classification of hydrate deposits. Depending on the geologic and reservoir conditions, the natural gas deposits are divided into three main classes:

1. A hydrate layer overlying a two-phase fluid zone with water and free mobile gas.
2. A hydrate layer overlying a mobile water zone (e.g. aquifer).
3. A hydrate layer with no underlying fluid zones.

Class 1 requires the least amount of energy (changes in temperature and pressure) to dissociate the hydrate, and is the most desirable system for production because the base of the GHSZ coincides with the bottom of the hydrate-bearing layer. Class 2 and 3 may be well within the hydrate stability zone caused by the absence of a gas zone and any fluid zone, respectively. As a consequence, these scenarios required more energy to produce gas, and this is not favorable, but still possible. Typical for many oceanic hydrate deposits, the hydrate zone is dispersed, has a low saturation (<10%) and has no free fluid phases in close vicinity. This type of hydrate deposit was later presented as a fourth class (Moridis, 2011), and concluded to not be promising for production.

1.2.3 Gas hydrate production scenarios

Gas may be recovered from gas hydrate by three main dissociation scenarios: (a) thermal stimulation, (b) depressurization and (c) thermodynamic inhibition. These production scenarios are illustrated in Figure 9.

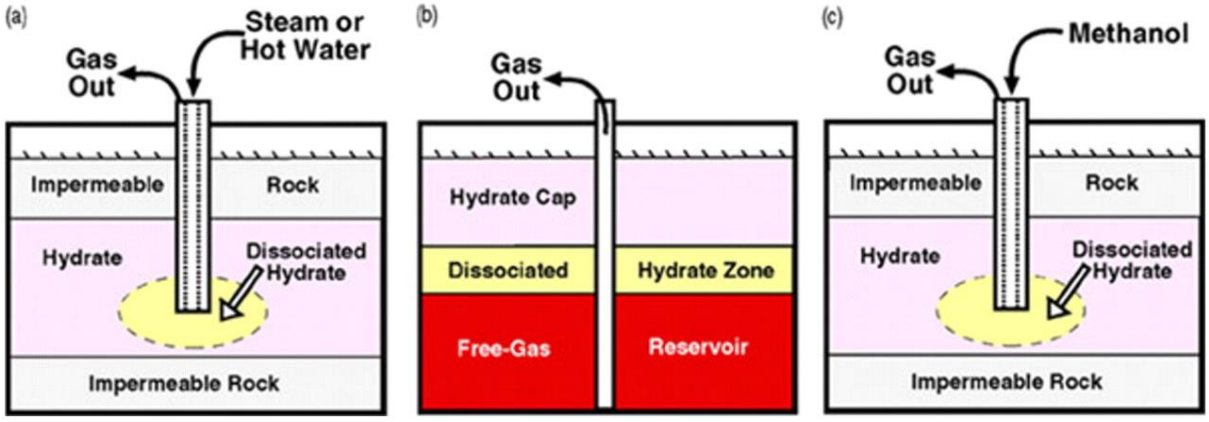

Figure 9: Schematic of the three production mechanisms (Collett, 2002).

Thermal stimulation can be performed by injection of heated fluids (e.g. steam or hot water) or potentially direct heating of the formation (e.g. electrical heating of cables in production pipelines). Depressurization is performed by producing free gas so that the pressure decreases, and the hydrate eventually dissociates. Both these methods are based on moving the hydrate conditions outside the hydrate stability region. By injection of thermodynamic inhibitors, such as alcohols or glycols, into the reservoir, the hydrate stability condition will decrease and gas production may commence. In this

thesis controlled dissociation by depressurization or thermal stimulation will be conducted in combination with the thermodynamic inhibitor NaCl.

Numerical simulations have been performed for depressurization and thermal stimulation with respect to the different hydrate deposit classes mentioned in 1.2.2 (Moridis and Collett, 2003). Depressurization was favorable for class 1, while for class 2, a combination of both depressurization and thermal stimulation would result in the best outcome. For class 3, it was more favorable with thermal stimulation through single well systems, because of the low permeability conditions.

In general, depressurization is seen as the most promising production scenario as it is more economical and energy efficient than both thermal stimulation and thermodynamic inhibition. Thermal stimulation will lead to a relatively slow dissociation, and the endothermic nature of gas hydrate dissociation will partially counteract the warming of the formation (Ruppel, 2011). The high use of hydrate inhibitors, such as methanol, may come with a high environmental cost (Collett, 2002).

The production schemes presented, all involves geomechanical challenges. Often the deposits that are suitable targets for production, have poorly consolidated sediments usually characterized by limited shear strength (Moridis, 2011). Hydrate is known to be a strong cementing agent, and dissociation may cause the structural strength in the sediments to decrease. Hydrate bearing sediments in near vicinity of the well bore have the highest risk of collapsing. Also, the endothermic nature of gas hydrate dissociation may cause the reformation of ice and/or gas hydrate, which may prevent gas extraction.

A more recent production scheme is based on the sequestration of CO_2 to produce methane gas. Exposing CO_2 to the methane hydrate will result in spontaneous conversion, where the methane gas is liberated and CO_2 hydrate is created (Graue et al., 2008). Methane gas is produced without adding heat to the process and with no associated water production. This production scheme may also offer stable long-term storage of greenhouse gases.

2 Literature survey

The following literature survey addresses previous research on hydrate formation and hydrate dissociation in synthetic porous media, cores and bulk phase. Studies on hydrate formation and hydrate dissociation are discussed in relation to results in this thesis in section 4.1 and sections 4.2-4.3, respectively.

2.1 Hydrate formation in micromodels

The first direct pore-scale observations of hydrate formation was demonstrated by Tohidi et al. (2001), using a synthetic 2D glass micromodel with an etched pore network. They formed hydrate from free gas (CH_4), from gas (CO_2) dissolved in water and from a soluble liquid hydrate former (tetrahydrofuran, C_4H_8O). They discovered that hydrate can form with the dissolved CO_2 without the presence of a free gas phase. Hydrate formed by the free gas began at the water-gas interface, where gas bubbles were encapsulated by the free water. Formation primarily occurred in the center of the pores and not on the pore walls, because a thin water film remained there, surrounding the grains. However, hydrates could be cemented to the grains if the grains were small, or a sufficient proportion of the pores were already filled with hydrate.

Further investigation of methane hydrate formation has been performed by Katsuki et al. (2007), visually observing growth patterns at different degrees of subcooling. They used a micromodel made of two quartz glass plates which were welded together. Within the model, microchannels were carved in straight channels of 100 μm and arranged in a grid pattern of 200 μm intervals. The porous medium was filled with presaturated water (CH_4) and gaseous methane, and kept at a constant pressure (101 bar), which formed hydrate. At low degrees of subcooling, hydrate formation occurred at the interface between the liquid water and gaseous methane, creating faceted hydrate crystals. The faceted hydrate crystals bridged the pore spaces, and may have formed physical bonds with the walls of the porous medium, and they also grew into the liquid water. The crystal growth into the liquid water was explained by methane molecules being transferred from the gaseous methane not enclosed by the hydrate film. At high degrees of subcooling hydrate formation appeared dendritic. The dendritic hydrates did not bridge the channels because of the absence of additional methane supply.

Studies on hydrate formations, with emphasis on morphology, have been conducted by Ohmura et al. (2004) and Ohmura et al. (2005). Ohmura et al. (2004) formed CO_2 hydrate in bulk conditions at different degrees of subcooling with a constant pressure of 34 bar, and Ohmura et al. (2005) formed CH_4 hydrate in bulk conditions with varied pressures at a constant temperature of 273,5K. Both studies had similar results as Katsuki et al. (2007), where for low driving forces (low degree of subcooling and low pressure) hydrate crystals were observed as faceted. For high driving forces (high degree of subcooling and high pressure) the faceted hydrate crystals were replaced by dendritic crystals.

More recent observations of hydrate formation in synthetic porous media have been made by Hauge et al. (2016). They looked at CO_2 and CH_4 hydrate growth in a high-pressure silicon micromodel, similar to the micromodel which is used in this thesis. It was observed that local fluid distribution and fluid connectivity within the pore network had influence on the growth patterns for hydrate. Initial hydrate growth under static conditions was slow, so agitation was used as a tool to provoke the growth. In gas-filled pores the hydrate growth was observed in the following pattern:

1) Initial thin hydrate film growth between the water-gas interfaces

2) The hydrate film grew thicker alongside the pore wall and eventually towards the center of the pore.
3) Redistribution (shrinking and growing) of hydrate over time

In water-filled pores hydrate grew if the free gas was partially displaced by water. Observations of the hydrate growth rate indicated that growth along the grain wall was fast, while growth towards the pore center was slow. Since water accumulated in the pore corners, creating thick water films, there was sufficient accessibility of water, which allowed fast hydrate formation along the walls. Hydrate formation towards the pore center relied on water migration from the pore corners and was therefore slow.

Equilibrium conditions

Husebø et al. (2009) investigated the effects of salinity on hydrate stability during methane hydrate formation in Bentheim sandstone cores with core analysis and MRI imaging. The cores were saturated with approximately 50% brine, with salinities ranging from 0.1 to 5.0 wt% NaCl, before methane was introduced, and the cores were pressurized to 10.1 MPa and 8.2 MPa and cooled to 4.0°C. The experiments indicated a longer induction time and less hydrate formation with increasing initial salinity. Once methane hydrate was formed, the surrounding free water increased in salinity, which postponed further formation. They concluded that for initial salinity higher than 4.0 wt% NaCl, salinity was the limiting factor for further hydrate formation, whereas for lower salinities, the porous media was the limiting factor, rather than the salinity.

The capillary effect on methane hydrate phase equilibria in porous media has been investigated by Turner et al. (2005) and Uchida et al. (2004). Turner et al. (2005) performed a sensitivity calculation of methane hydrate equilibrium shifts in an Adriatic sandstone pore network with an average pore radius of 550 Å (0.055 µm). Results showed that the temperature shift was less than 0.2% or -0.55 K at 237.15 K for pore radii greater than 600 Å (0.06 µm), and thereby negligible. The equilibrium shifts for hydrate in the pore network was compared with equilibrium data for hydrate bulk phase, and showed no difference. Uchida et al. (2004) measured the hydrate phase equilibrium conditions by the means of thermal decomposition in Berea sandstone, with grain size ranging from 50-200 µm. They observed that the decomposition temperatures in the porous network shifted lower than decomposition temperatures in bulk hydrates, and that the pore size distribution had the main effect on hydrate equilibrium conditions. Hydrates first formed in the largest pores saturated with water. If hydrate growth commenced in the small pores first, further growth was inhibited.

2.2 Hydrate dissociation on pore scale and core scale

Tohidi et al. (2001) thermally dissociated tetrahydrofuran hydrates, carbon dioxide hydrates and methane hydrates in a silica-glass micromodel. The melting of methane hydrate caused parts of the hydrate to shrink in size, some of which broke free and became mobile within the liquid phase. After the dissociation was complete, small crystalline structures remained in the liquid phase, even though the temperature was higher than the hydrate phase boundary for the system. The carbon dioxide hydrates were completely dissociated, returning all hydrate crystals to single-phase liquid conditions. No gas bubbles were observed during the dissociation. Dissociation of tetrahydrofuran hydrates led to a slurry of fine crystals, before the system was returned to a liquid state.

Methane hydrate dissociation was visually observed through micromodels made of quartz plates by Katsuki et al. (2008). (Specifications of the model were the same as described in Katsuki et al. (2007).) They performed dissociation by the means of depressurization and thermal stimulation and provided image sequences of the events. Direct pore observations showed that dissociating hydrate crystals

released methane molecules, creating methane bubbles, which formed vapor slugs that occupied the pore channels. For thermal stimulation the bubbles of methane were initially formed on the hydrate crystal, but eventually diffused through the liquid water to an adjacent methane slug. Depressurization formed bubbles of methane directly in the liquid phase and grew to larger slugs. Not all of the dissociation resulted in formation of a vapor methane phase on the hydrate crystal surface. This was explained by the temperature dependences of methane solubility in liquid water. Methane concentrations in liquid water, when in equilibrium with hydrate crystals, will increase with increasing temperature, but will decrease with increasing temperature, when in equilibrium with the fluid methane phase. The temperature difference between the equilibrium cases would cause methane to diffuse through the water phase to a gas bubble.

On the core scale, dissociation of sedimentary methane hydrates has been performed with various salinites. An experiment using 3.5 wt% NaCl, was performed by Almenningen et al. (2016), observing the volume of methane produced from Bentheim sandstone cores during pressure depletion. The cores were depressurized over several pressure steps of 0.07 MPa, until most of the hydrate had melted and the methane was produced. Approximately 10% of the hydrate melted at the first pressure step, and complete dissociation required 10-15 pressure steps. They believe that water liberated from the hydrate during dissociation contributes to a decrease in salinity of the free water, making the hydrate phase more stable towards the water phase. The micromodel work performed in this thesis will be compared with similar studies previously performed on the core scale using Bentheim sandstone.

3 Methodology

All of the hydrate formation and dissociation have been conducted at the Department for Physics and Technology at the University of Bergen. The setup used in the laboratory is a modification of previous work done by master and PhD students, as illustrated in Figure 10. An elaborate description of the micromodel is given in section 3.1.1 and 3.1.2. Experimental procedures for hydrate formation and dissociation are presented in section 3.1.3 and 3.1.4, respectively. In section 3.2, key specifications and limitations for the micromodel are presented.

3.1 Experimental setup

A microscope (Nikon SMZ1500) connected to a camera (Nikon D7100) made it possible to visually observe hydrate behavior during formation and dissociation directly in the micromodel. The camera was able to retrieve a clear picture trough the reflected light from the light source (Photonic LED F1 cold light 5500K). All of the observations were documented continuously during every process, either by interval pictures or film. To gain a better view of the micromodel during experiments a monitor was connected to the camera.

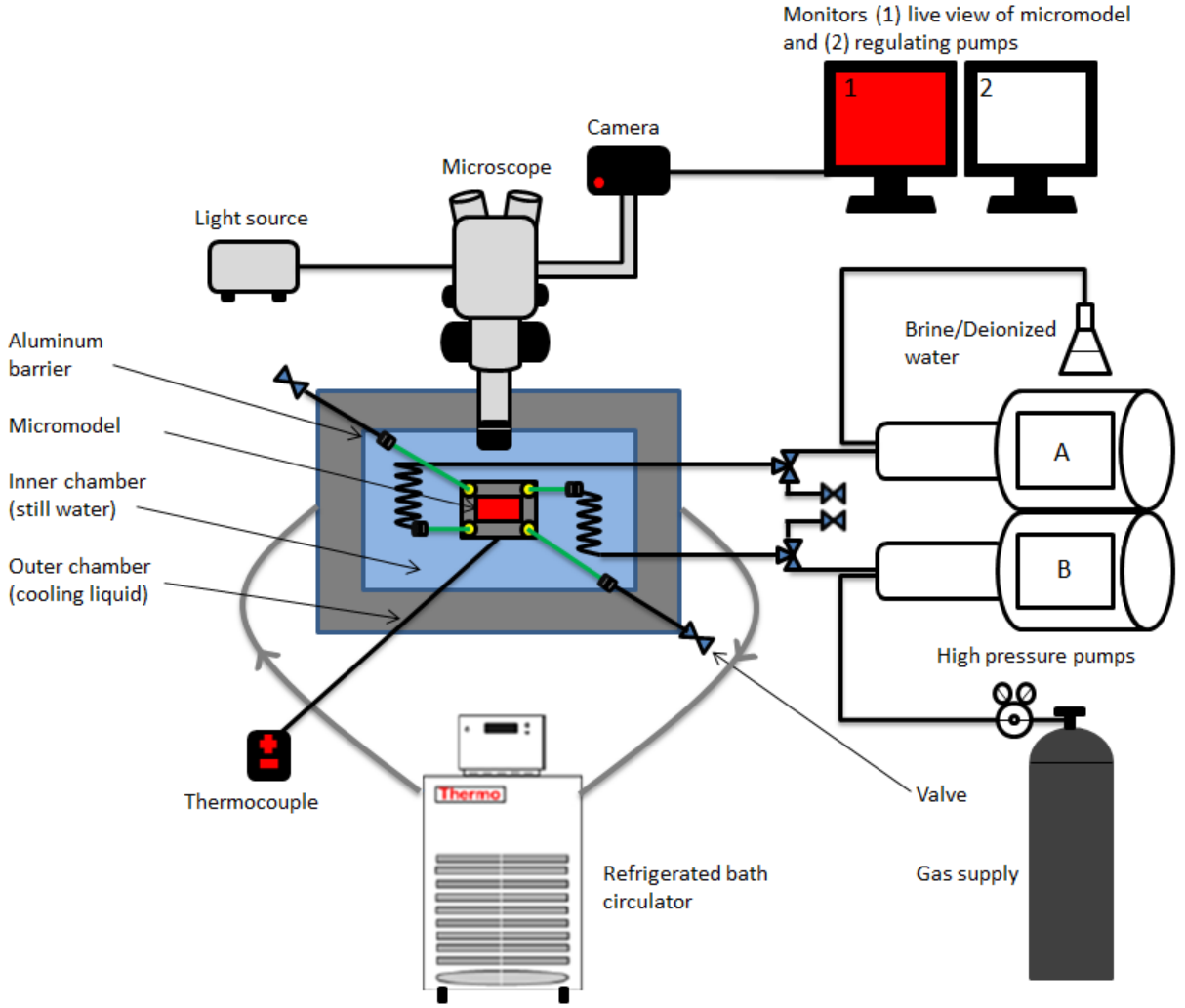

Figure 10: Experimental setup for hydrate formation and dissociation. A lid was placed on top of the cooling chamber. The red color represents the pore network of the micromodel. The green lines represent the 1/16" PEEK tubing.

A Quizix Q5200 pump system, which has two pumps working independent of each other, was used to inject fluids into and reject fluids out of the micromodel. Pump A was filled with either deionized water or brine, and pump B was filled with methane gas (>99.5%). The high pressure micromodel, indicated by the color red, was assembled in the center of the cooling chamber, surrounded by distilled water. The micromodel and the pump were connected together by a combination of 1/16" PEEK (polyetheretherketone) and steel tubing as well as 1/8" steel tubing. To create an optimal flow path through the micromodel, the pumps were connected in opposing corners creating a diagonally pathway. This ensured that the whole model was saturated with both methane gas and deionized water/brine. The two remaining ports were available so that the model could be flushed/cleaned between experiments. These ports were also used to create agitation in the system. All of the ports were controlled by valves placed outside the chamber.

To achieve the required temperature for hydrate formation, a refrigerated bath circulator (Thermo Scientific Neslab RTE 17) was connected with rubber tubing to a specially designed cooling chamber. The cooling chamber was made up of an outer chamber and an inner chamber, only separated by an aluminum barrier. Water was circulated through an inlet on one side via an elevated outlet on the opposing side, so that the whole outer chamber was filled up. By adding an antifreeze liquid, the water was kept from freezing in the outer chamber and in the circulator. The cooling chamber was mostly made up of Plexiglas, with the exception of the aluminum barrier. The aluminum barrier, with a higher thermal conductivity than the Plexiglas, surrounds the inner chamber, causing the heat to be directed to the still water rather than to the surroundings. To ensure that heat was transported through the aluminum barrier, the cooling chamber was placed on a block of Styrofoam (low thermal conductivity) and taped with isolating tape. Previous experiments performed with similar setups, indicated that temperature fluctuations in the still water was caused by temperature fluctuations in the surroundings (ventilation system was turned off during the night). Therefore, as a precaution, a lid was placed on top of the cooling chamber during experiments. This kept the temperature stable, as well as preventing foreign particles entering the still water. The temperature was measured directly beneath the micromodel in the still water by a thermocouple (HH506RA Omega Multilogger), and was continuously under observation.

The 1/16" steel tubing submerged in the still water was coiled, acting as reservoirs, so that the water and gas had the acquired temperature conditions before entering the micromodel. This was possible because of the low flow rates into the model. It was critical that the tubing connecting the micromodel to pump B only contained methane gas during the experiment, or else hydrate plugging could occur.

3.1.1 The micromodel

The micromodel used in the experiments is shown in Figure 11. It is classified as a high pressure micromodel with a capacity up to 150 bars, and is produced by Pharmafluidics. The model is 1.7 mm thick and consists of two main parts, a silicon wafer and a borosilicate glass wafer. By using standard photolithography techniques, a two-dimensional pore network is etched into the silicon wafer (Buchgraber et al., 2012b). Thereafter, the silicon wafer is anodically bonded to the glass wafer, isolating the flow path and allowing direct observation of the pore network (Hornbrook et al., 1991). As a result of the bonding, a thin oxide layer is created on the pore structure surface, making the micromodel water-wet. The micromodel is a replica of a Berea sandstone pore network, and has an average pore size in the order of 100 μm.

The construction procedure is based on (Buchgraber et al., 2012a, Hornbrook et al., 1991), and outlined below:

- A thin section of a porous medium is photographed at high enough magnification to capture the grain details. The photo consists of black and white pixels, which represent the pores and the rock matrix, respectively.
- The image is digitized at a high enough resolution to ensure a continuous flow path. For this to happen, in most cases, the image has to be altered by manipulating tools.
- An image mask is constructed by determining the exact size of the flow path image. This is done by defining the height and width of each pixel.
- The image is now transferred and etched onto the silicon wafer. At this stage it is essential that the silicon wafer is dry. Once the silicon wafer is dry, it is prepared by coating it with a photo-resist material. Afterwards the image mask is placed on the coated side of the wafer and exposed to ultraviolet light, resulting in the exact transfer of the image mask to the wafer. The silicon wafer is then etched with a DRIE (Deep Reactive Ionic Etching) technique, creating a two-dimensional vertical profile, with the same height throughout the model.
- Finally, four holes (ports) are drilled on the backside of the model, before the two wafers are bonded anodically together. As an extra precaution, due to high pressure, the bottom of the micromodel is coated with epoxy, which increases its strength and reduces the chance of it being cracked.

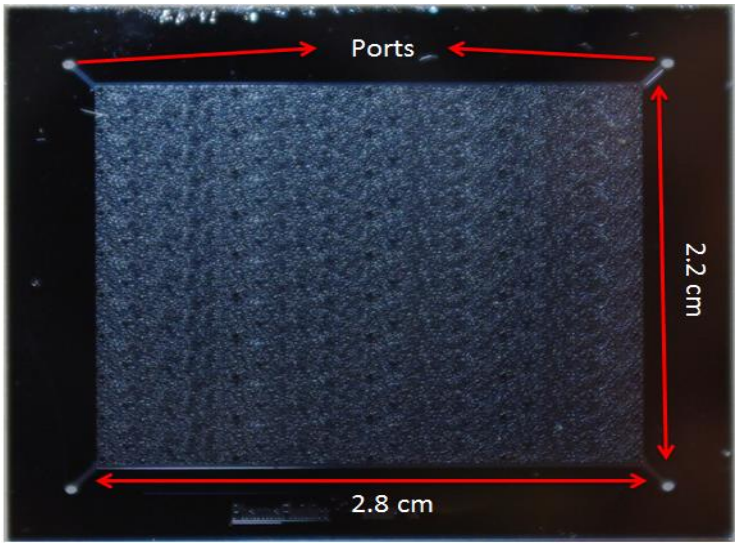

Figure 11: Top view of the micromodel with the etched pore network in the center. The vertical depth etched by DRIE is 25µm. Notice that the ports on the longest side of the rectangle are connected to a channel from one side to the other to ensure flow through the model.

3.1.2 Assembling the model

The micromodel was mounted between two aluminum frames (steel casing), produced by Pharmafluidics, as sketched in Figure 12. The assembly was an important component in the experimental setup, as it ensured that the micromodel was kept still at all times, and it also made sure that the micromodel had a continuous flow path from the ports to the rest of the setup, especially to the pumps. The following four steps were taken when the micromodel was assembled:

1. The four nano tubing guiders with rubber packings were placed in the lower aluminum frame. The lower aluminum frame had a rectangular 1,7mm indent which fitted the micromodel's outer dimensions.
2. The micromodel was carefully placed in the indent, only resting on the rubber packings. It was placed so that the ports of the micromodel had a clear path through the guiders, ensuring a continuous flow path.
3. The upper aluminum frame was attached to the lower aluminum frame with eight 3 mm screws. First the screws were finger-tightened and then fully tightened with a momentum key set at 1Nm torque. This specific torque was recommended so that the micromodel would not crack under high pressure. The screws were tightened in opposing pairs so that an equal amount of strain was applied the micromodel in all corners.
4. Finally, the PEEK tubes were connected to the nano guiders by nano tubing fittings, as illustrated in Figure 13.

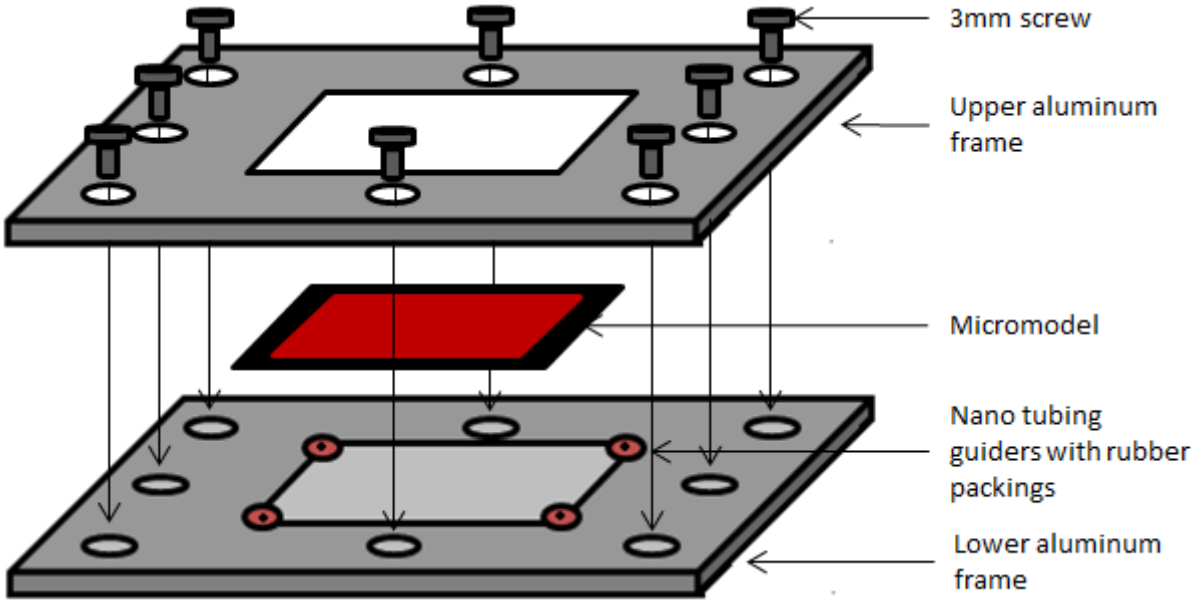

Figure 12: Sketch of the how the model was assembled. The red rectangle represents the etched pore network. The upper aluminum frame and lower aluminum frame is approximately 0.47 cm and 0.97 cm thick, respectively.

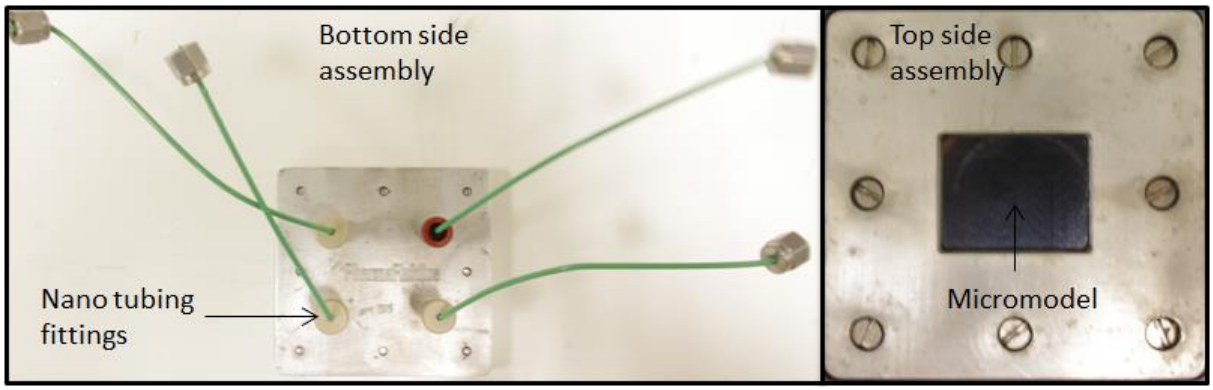

Figure 13: Final bottom and top side of the steel casing, with the micromodel assembled in the center, and ready for experiments.

3.1.3 Formation methane hydrate procedure

After the micromodel had been assembled in the steel casing and connected to the PEEK tubing, it was submerged in the chamber. Distilled water was filled into the chamber covering the micromodel, and both pumps were filled with their respective fluids. The micromodel was then cleaned/flushed with deionized water/brine (liquid) from pump A, by keeping the three remaining outlet valves open. After all the remaining gas (air and methane) and previous water solutions were removed, the outlet valves were closed, and the pore network was assumed saturated with liquid. The liquid and the micromodel were then pressurized to 40-50 bar with pump A before all valves were closed. Subsequently, the methane gas was pressurized to 10-15 bar above the micromodel pressure, and the valve from pump B was opened. Since the methane pressure in pump B was higher than the liquid pressure in the micromodel, the gas displaced the liquid in the coiled tubing before invading the micromodel. This was done to prevent the possibility of hydrate plugging in the tubing. After an approximately 50-50 saturation of methane and liquid was achieved, the micromodel was ready to be pressurized and cooled to the acquired hydrate formation conditions, mostly 83 bar and 4.0°C. During the cooling period the camera was set to take interval pictures to monitor the development.

Both pumps kept the pressure stable with an *independent constant pressure operation* configuration, and the refrigerator bath circulator kept the temperature constant. The fluids inside the micromodel were now capable of static hydrate formation. If hydrate formation did not occur over a two-day period, agitation was forced to the system. Agitation was performed by two different methods:

1. Opening the valve connecting the micromodel to the water pump, redirecting some water and gas from the model into the tubing (not into the pump).
2. Slightly opening one of the two closed valves that connected the model to atmospheric conditions, before quickly closing it again.

The pressure difference between the micromodel and the tubing/outside caused water and gas to be redistributed and agitated. Method 1 was preferred over method 2, and was always performed first in order to keep the fluid distribution (ratio of water and gas) similar to the initial distribution. When agitation was performed, the pressure inside the micromodel was always higher than outside the micromodel, so that no external fluids entered the micromodel. As soon as the micromodel was agitated, the hydrate formation was recorded by the camera. Once hydrate formation had occurred, the hydrate behavior was monitored over time by interval photos.

3.1.4 Dissociating methane hydrate procedure

Methane hydrate was dissociated either by pressure depletion or thermal stimulation by increasing the temperature in the cooling bath.

Primary hydrate formation always occurred 30-50 bar above the dissociation pressure, so the micromodel had to be depressurized. The pressure was decreased to approximately three bar above the dissociation pressure conditions (see Figure 4), and subsequently it was decreased further in increments of 0.7 bar to observe the detailed dissociation patterns. For each interval, recordings of 5-20 minutes were taken at first, the time depending on the fluid behavior in the model. This was followed by taking images every second minute. Pressure depletion was performed by pump B when there was brine in the micromodel, ensuring that there was no alteration of the salinity. When the micromodel was pressure-depleted with dionized water, either one of the pumps was used.

Dissociation by thermal stimulation was performed with a constant pressure of 40, 50 or 60 bar. Once the pressure had stabilized over a sufficient period, the temperature was raised to 2°C below the stability condition, and further increased in increments of 0.1°C, until a complete dissociation had

occurred. The monitoring of the dissociation by thermal stimulation was similar to the one used for pressure depletion.

3.2 Specifications and limitations for the micromodel

3.2.1 Optic specifications

Since the experimental work is based upon microscope images, it is important to identify how the optics can distinguish between the different media in the micromodel. Figure 14 represents a typical image taken from the micromodel saturated with fluids and gas hydrate.

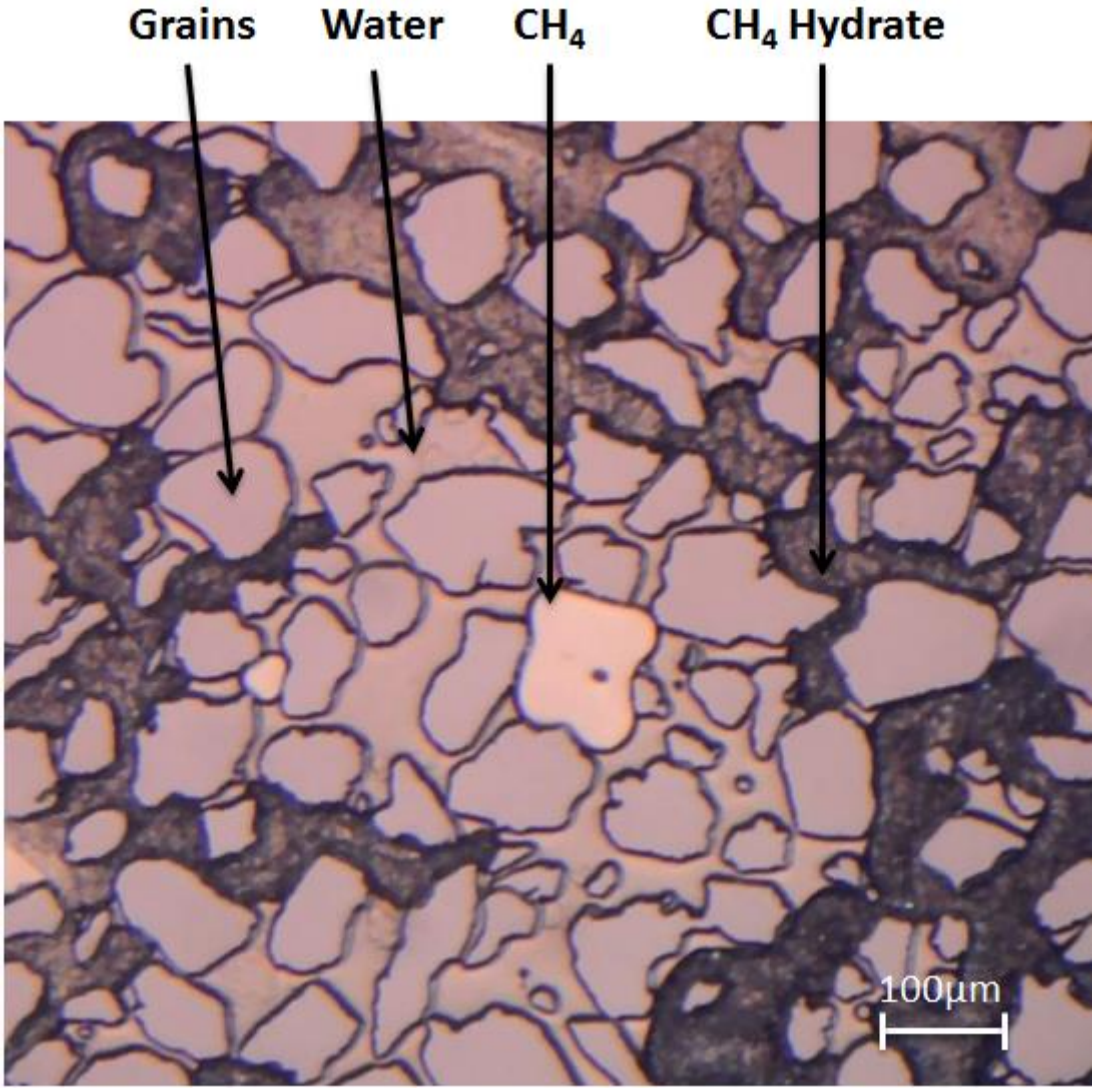

Figure 14: View of the micromodel through the microscope. Four different media are present: Grains (silicon), water, methane gas and methane hydrate (hydrate film). Note the scale of the image in the bottom right corner.

The refractive index describes how light propagates through a medium, and it also gives an indication of the amount of light that is reflected on different surfaces. If two non-absorbing media have different refractive indices, they can be distinguished visually. Consequently, if two non-absorbing media have the same refractive index, it is not possible to distinguish between them (Bylov and Rasmussen, 1997). Table 2 gives an overview of the different media present in the micromodel, methane gas, water, methane hydrate, borosilicate glass and silicon.

Table 2: Refractive indices for media represented in the micromodel

Media	**Refractive index *n***	**Reference**
Methane gas	1.000	(TheEngineeringToolBox, n.d.)
Water	1.333*	(TheEngineeringToolBox, n.d.)
Methane hydrate (structure I)	1.346	(Bylov and Rasmussen, 1997)
Borosilicate glass	1.517	(Polyanskiy, 2016)
Silicon	3.500	(Jin et al., 2010)

**The refractive index will increase slightly with increasing salinity, but is negligible for the experiment.*

Methane gas, water and methane hydrate are the media of most interest. The gas and water phases can be detected above or below the hydrate films by evaluating the refractive indices (Almenningen et al., 2016, Flatlandsmo, 2015). The difference between the refractive index of water and hydrate is small (0.013), causing nearly no light to be reflected at the interface between them. Consequently, most of the light will travel through both phases and be reflected back to the microscope by the silicon wafer. On the other hand, the difference between the refractive index of gas and hydrate (0.346), or between water and gas if the hydrate film is coated with a water layer (0.333), is significant. In this case, much of the light will be bent and reflected at the interface between the phases, spread so that the hydrate will appear darker. Small amounts of light will return to the microscope as the hydrate film will distort the reflection. The gas phase may lie either under or over the hydrate film.

The black line surrounding the gas phase in Figure 14 is not hydrate, even though it is darker. Since the pore network is water-wet, a curved water-gas interface will develop, and less light will be reflected back to the microscope. There are also black lines surrounding the grains. These appear as a consequence of light creating shadows. If there is a hydrate phase close to the grains, it is hard to determine whether it actually is hydrate or a shade.

Image color and brightness

The color and brightness of the images may vary depending on whether the produced image is from a photo or a video. In most cases, the photos appear brighter and bluer while the videos appear darker and redder. The most important measure to ensure viable and clear images was having correct camera settings. The two camera settings most frequently used, were an aperture of F13, a shutter of 1.6” and auto ISO for photos, and an aperture of F13, a shutter of 1/30” and 2000 ISO for videos. The white balance (warm or cold image) was set to 5500K, which represents daylight. This combination made it possible to achieve clear and detailed images, but as a consequence the images were sensitive to small interferences.

The color and brightness of the images are also influenced by the internal light source, external light source, magnification of the microscope and the still water in the inner chamber. *The internal light source* consisted of two main light rays, representing the red and blue part of the visible spectrum. The two light rays were directed through the lens from opposing sides and reflected back to a mirror in the lens (Nothnagle et al., 2016). Once the light rays overlapped each other the image became white and clear. If the angles of the reflected light rays were slightly changed, the photos and videos obtained would become bluer and redder. The angle could be changed due to irregularities on the surface, such as bulging of the micromodel. Bulging could be caused by tension on the silicon and glass wafers due to high pressure. The micromodel was assembled in the center of the steel casing, and the upper aluminum frame is tightened to the lower aluminum frame, which could result in extra strain on the outer edges of the micromodel, making it bulge. Observations made with the microscope showed that the outer parts of the micromodel were bluer while the center was redder.

The external light source is mainly the light from the laboratory, which may create darker parts (shadows) on the edges of the images.

The magnification of the microscope has a zoom ratio of 15X, ranging from 0.75X to 11.25X. The ratios used in this thesis were 3X and 6X. Compared to the higher zoom, the lower zoom often resulted in whiter images and less shadow surrounding the grains in the micromodel, but the edge of the image often became darker. Due to these observations, the higher zoom was preferred in order to retrieve more detailed images.

When the reflected light rays from the microscope passes through *the still water*, a light-shadow is created, as illustrated in Figure 15. Spreading of the light in the water due to impurities may influence the brightness, color and focus of the picture. Typical impurities observed were dust particles. As the temperature was increased or decreased in the still water, the image often became blurry due to vapor, so the focus had to be changed. For this reason, a thin water layer above the micromodel is favorable for a clear image.

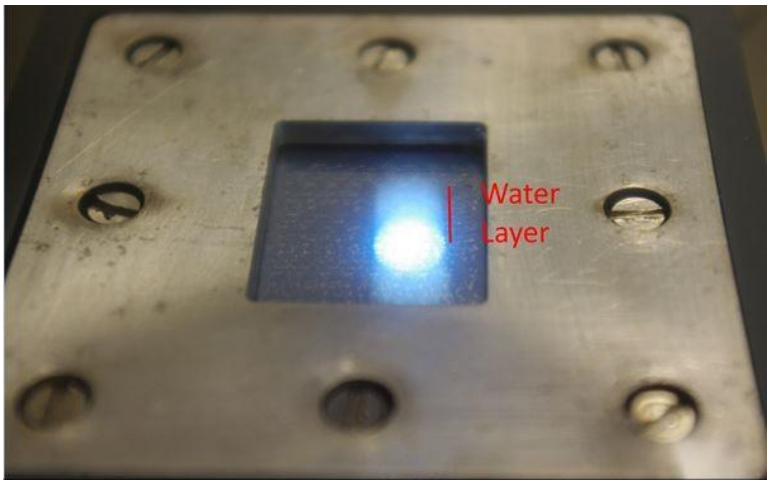

Figure 15: Microscopic view from outside the micromodel. The two light rays overlap to gain focus in depth. The water shade represents the water thickness.

Water films

Thin water films were observed coating the glass wall of the micromodel, on top of gas, as illustrated in Figure 16. The water film may look different depending on its thickness, and in most cases the films were thicker in the center and thinner at the edges. It seemed as if the water films were drained during fluid movement in the micromodel. Gas is expected to lie on top of water due to gravitational effects. For this reason it is impossible to verify whether gas actually displaces water completely, or if it just lies on top of the water as a thin film.

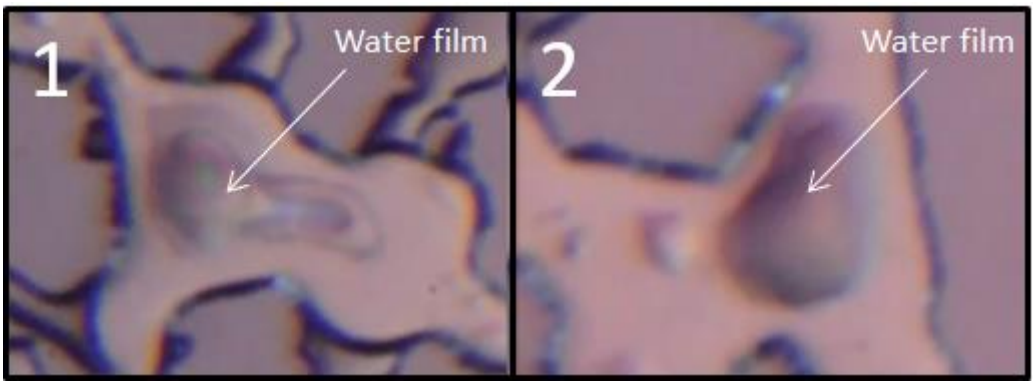

Figure 16: Two example of water films being present in the porous media.

Salt crystals

As illustrated in Figure 17, the light blue-green color phases in the porous media were believed to be salt crystals. The salt crystals were observed surrounding the hydrate phase (1A) and on the water-gas interface (1B), and were only observed when brine was used for the experiments. To verify the observations, a picture was taken of pure salt (2). The color resemblance between pure salt and salt crystals observed in the porous media, indicates that it indeed may be salt crystals.

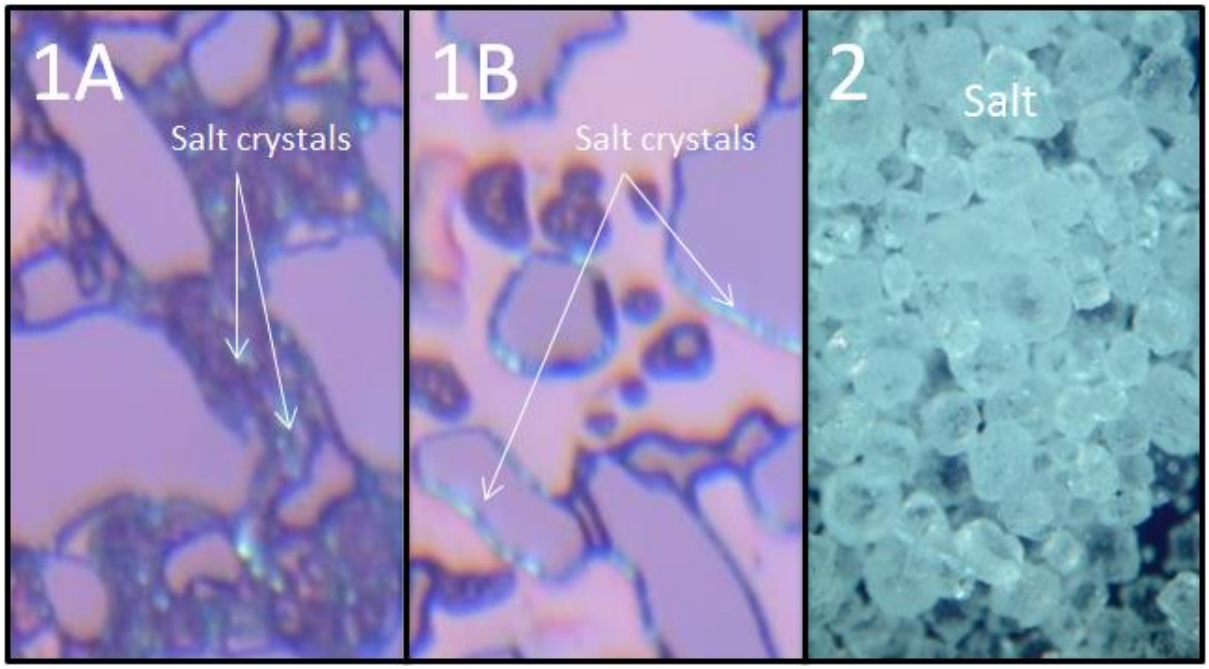

Figure 17: Salt crystals surrounding hydrate (1A) and on the water-gas interface (1B), compared against pure salt (2).

3.2.2 Thermal uncertainty

The temperature inside the micromodel was measured indirectly by a thermocouple, which was placed beneath the aluminum barrier in as close proximity as possible. Therefore the heat transport from the still water through the aluminum casing and the micromodel had to be evaluated. Since the aluminum casing was tightened at a specific torque, a thin water film may also be present in the indent below the micromodel. The thermal conductivity for water, borosilicate glass, silicon and aluminum are presented in Table 3.

Table 3: Thermal conductivity of different media for the evaluation of heat transport.

Media	**Thermal conductivity [W/mK]**	**Reference**
Water	0.609 (27°C)	(Lillestøl et al., 2001)
Borosilicate glass	1.14	(Azom, 2009)
Silicon	148 (27°C)	(EL-CAT, n.d.)
Aluminum	237 (25°C)	(Lillestøl et al., 2001)

Water and borosilicate glass have a thermal conductivity significantly lower than silicon wafer, and will therefore act as isolators within the micromodel, while most of the heat transport will go through the silicon wafer. From the thermocouple to the micromodel, the thin water layer in the indent of the aluminum frame may act as an isolator, while the aluminum frame itself, with high thermal conductivity, will transport heat well. The thin water layer will therefore be the limiting factor. Assuming that the thin water layer is so thin that it can be neglected, the temperature inside the micromodel and in the still water should be equal. The micromodel was totally surrounded by water, and the heat transport will be defined by the thermal conductivity for aluminum and silicon, which are high. Because the temperature inside the micromodel was measured indirectly, the local temperature variations in the model were difficult to measure.

3.2.3 Volume uncertainty

The difference in the tubing volume and the pore volume of the micromodel has to be taken into account for each experimental run. Table 4 shows the approximate total volume of the tubing.

Table 4: Volume approximation of the tubing in the experimental setup.

Tubing	**Inner dimeter [cm]**	**Length of tubing [cm]**	**Volume [ml]**
PEEK tubing	0.08	40	0.8
1/16” steel tubing	0.10	399	12.5
1/8” steel tubing	0.15	425	30.0
		Total volume	**43,3**

The pore volume of the micromodel is estimated with the following equation:

$$V_p = HLW\phi \tag{3.1}$$

where V_p is the pore volume, H is the height, L is the length, W is the width, and ϕ is the porosity. The porosity was found by the method explained in section 3.3, and was estimated to be 0.47±0.04. Using the micromodel dimensions from Figure 11, the pore volume was estimated to be 0.0072±0.0006ml. The volume of the tubing was several orders larger than the volume of the micromodel, so it was essential that the tubing was completely saturated with the appropriate liquid and gas. The micromodel is a two-dimensional pore network with vertical walls, and does not have curved walls, as in a Berea core sample would. For this reason the porosity is larger in the micromodel than in the Berea core sample.

3.3 Two-dimensional saturation estimations

Two-dimensional saturation changes were estimated to evaluate the fluid distribution and fluid redistribution during hydrate formation and dissociation. Previous observations have determined that hydrate becomes black/darker through a microscopic view (Tohidi et al., 2001, Flatlandsmo, 2015). Therefore, the hydrate saturation was estimated under the assumption that hydrate was visually observed as grey-black in the micromodel. Two important matters had to be considered with regard to the estimations. The first concern was that hydrate is only seen as black in gas and not in water. Hydrate films can form in the water, but they may not be visible through the microscope. The second concern was that it was impossible to determine the saturation in depth in the pore network since the microscope only gives a 2D perspective. Hydrate films may both lie above and below the gas and water. Flatlandsmo (2015) estimated that hydrate appear black if the hydrate film was of a certain thickness (>1.5µm), and if the hydrate film was very thin, the hydrate becomes transparent. With a depth of 25µm in the micromodel the 3D saturation might be very different.

An example of the procedure to determine the porosity and saturation in the porous media is presented in Figure 18. Using *paint.net*, a graphics editor program, water, gas, hydrate and grains were located in the micromodel and colored. Grains were colored with green, and water, gas and hydrate were colored with blue, red and black, respectively. Each image contains a total amount of pixels, and each color represents a certain amount of the total pixels. The porosity was estimated using equation 3.2, and the water, gas and hydrate saturations were estimated using equation 3.3.

$$\phi = \varepsilon_{\phi} = \frac{\varepsilon_{total} - \varepsilon_{grains}}{\varepsilon_{total}} \tag{3.2}$$

$$S_{w,g,h} = \frac{\varepsilon_{\phi} - \varepsilon_{w,g,h}}{\varepsilon_{\phi}} \tag{3.3}$$

where ε is the amount of pixels, and $S_{w,g,h}$ is the saturation of water, gas and hydrate, respectively. Not all of the pixels in the image were colored, and this resulted in a residual pixel amount. The amount of pixels for gas, water and hydrate had to be normalized to account for the residual pixel amount, so that the sum of the water, gas and hydrate saturations was equal to one. Using the residual pixel amount, the uncertainty of every saturation measurement was estimated to be ±0.05.

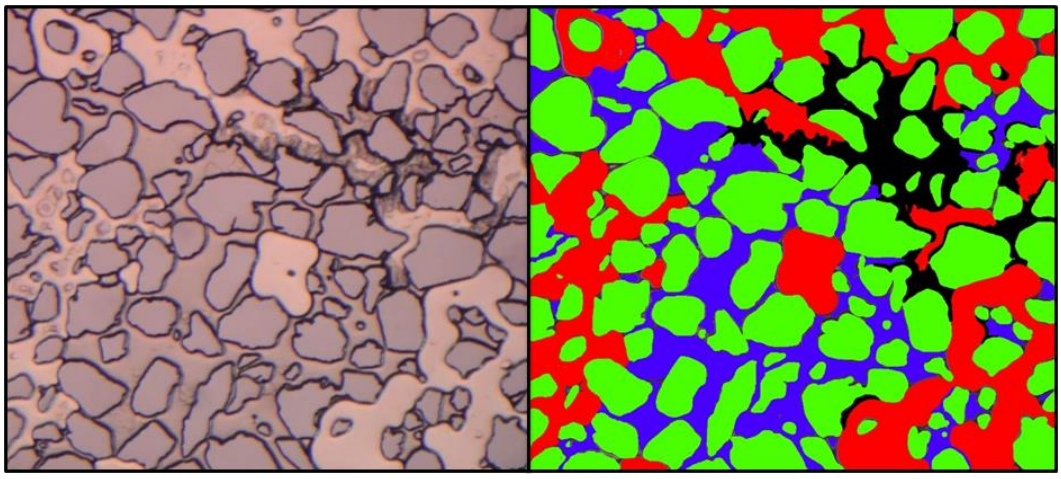

Figure 18: Illustration of how the two-dimensional saturation was estimated. Grains are colored green, water is colored blue, gas is colored red, and hydrate is colored black.

4 Results and discussion

The main objective of this thesis is to map methane hydrate formation and dissociation patterns with regard to different saline solutions (NaCl) at pore-level. Deionized water and saline water with 2.0, 3.5 and 5.0 wt% NaCl have been used. Hydrate has been dissociated by depressurization and by thermal stimulation to observe if there are any different patterns between the methods. Research on hydrate formation and dissociation at pore-level is important, because fundamental knowledge of hydrate behavior under different conditions can be useful for possible natural gas hydrate production in the future. Pore-level interpretations may for example enhance experimental results on core-level and provide key inputs for hydrate simulations. The experimental results for hydrate formation are presented in section 4.1. The experimental results for hydrate dissociation by depressurization and hydrate dissociation by thermal stimulation are presented in sections 4.2 and 4.3, respectively. These three sections include three subsections each: Image sequences of the formation and dissociation experiments, saturation profiles of the image sequences, and interpretation of the observations made of the image sequences.

The experimental methane hydrate formations and dissociations are presented in a nine “field of view” image sequence for the different salinities. “Field of view” image refers to a section (image crop) of the photo or video where methane hydrate formation and dissociation occur. The sequences are organized by increasing salinity, starting from 0 wt% NaCl and ending at 5.0 wt% NaCl. The methane hydrate formation sequences are presented in time intervals, starting from the first observed growth of methane hydrate, and ending when the growth has ceased or decreased significantly. Sequences for methane hydrate dissociation by pressure reduction are presented with decreasing pressure, and sequences for methane hydrate dissociation by thermal stimulation are presented with increasing temperature. In order to observe the 2D saturation changes for each sequence, the saturation of methane hydrate, water and gas has been estimated for every image.

4.1 Hydrate formation

In this thesis there were performed a total of 20 methane hydrate formations in micromodels, whereof nine with 0 wt% NaCl, three with 2.0 wt% NaCl, four with 3.5 wt% NaCl and five with 5.0 wt% NaCl. All the formation experiments are summarized in Table 5. The four first attempts were performed with a micromodel that had previously been used to form bacterial flora. These experiments were unsuccessful as hydrates did not form, likely due to contamination of oil and/or calcite particles. For the 16 remaining experiments, a new micromodel was used, and hydrate formation was successful for every attempt. Out of the successful hydrate formations there were ten primary hydrate formations and six secondary hydrate formations. The pressure and temperature for primary formation varied depending on the salinity, but were initially held at 83.0 bar and 4.0°C. If hydrate did not form, the pressure was increased, and/or the temperature was decreased, until agitation was successfully forced on the system. The pressure for secondary formation was highly dependent on the salinity, and varied significantly. The temperature for secondary formation was approximately 4.0°C. Static formation condition refers to when there was no flow of methane and water through the micromodel, although there may have been redistribution of methane and water due to increased and decreased pressure. Agitation formation condition refers to when methane and water in the micromodel were intentionally released from the micromodel, or redirected through the tubing. The agitation process is described in detail in section 3.1.3. Four of the successful hydrate formations are presented as image sequences in section 4.1.1, where each one represents a different saline solution. The uncertainties of the values are discussed in appendix 7.1.

Table 5: Methane hydrate formation attempts for 0 – 5.0 wt% NaCl.

Exp.	Salinity ±0.01 [wt%]	Pressure ±1.4 [bar]	Temperature ±0.2 [°C]	Formation condition	Type of formation	Formation	Leakage [ml/h]
1	0	83.0	3.0	Static	Primary	No	0.017
2	0	83.0	3.1	Static	Primary	No	0.017
3	0	85.0	3.2	Static	Primary	No	0.017
4	0	84.0	3.0	Static	Primary	No	0.017
5	0	110.0	0.4	Static	Primary	Yes	0.019
6	0	110.0	2.4	Agitation	Primary	Yes	0.019
7*	0	46.5	4.1	Agitation	Primary	Yes	0.019
8	0	45.0	4.1	Static	Secondary	Yes	0.019
9	2.0	83.4	4.1	Agitation	Primary	Yes	0.013
10*	2.0	45.5	4.1	Static	Secondary	Yes	0.013
11	2.0	47.3	4.0	Static	Secondary	Yes	0.013
12	3.5	83.7	1.4	Agitation	Primary	Yes	0.036
13*	3.5	52.5	4.1	Static	Secondary	Yes	0.036
14	3.5	60.0	4.1	Static	Secondary	Yes	0.036
15	3.5	83.0	1.3	Agitation	Primary	Yes	0.012
16	5.0	80.0	1.3	Agitation	Primary	Yes	0.007
17	5.0	88.8	1.3	Agitation	Primary	Yes	0.007
18	5.0	88.8	1.3	Agitation	Primary	Yes	0.007
19*	5.0	83.4	1.2	Agitation	Primary	Yes	0.007
20	5.0	50.0	3.9	Static	Secondary	Yes	0.007

**The formations being presented as image sequences.*

4.1.1 Image sequences for hydrate formation

Following are four image sequences for hydrate formation, presented in Figures 19 to 22. Primary hydrate formations with deionized water and water salinity of 5.0 wt% NaCl, are presented in Figure 19 and Figure 22, respectively. Secondary hydrate formations with water salinity of 2.0 and 3.5 wt% NaCl are presented in Figure 20 and Figure 21, respectively. The hydrate formation sequences are presented in time intervals, starting from the first observed growth of hydrate and ending when the growth has ceased or decreased significantly. The experiments were performed to observe the general formation pattern, and to detect any similarities or dissimilarities between primary and secondary formation. The experiments were also conducted to see if there were any differences between the patterns of formation with deionized water and formation with saline water. The observed trend for formation development was that hydrate grew from the water-gas interface at the pore walls to the center of the pores. In addition, the connectivity of gas played an important role in how hydrate was being formed. A detailed interpretation of the saturation profiles follows in section 4.1.2, and the observations of the image sequences are discussed in 4.1.3.

For the purpose of illustrating the observations in every image sequence, colors have been used to distinguish between gas and water, and general observations. Gas is marked with red, while water is marked with blue. General observations are marked with yellow.

Deionized water

Methane was formed with deionized water by forcing agitation on the system at 46.5 bar with a constant temperature of 4.1°C. The primary hydrate formation process is shown in Figure 19, where initial hydrate formation was observed after one second. The initial hydrate formation occurred on the water-gas interface at the pore walls and hydrate continued to grow along the water-gas interface and towards the center of the pores. Further hydrate growth was fast, and after only ten seconds the hydrate saturation was 0.85. After 180 seconds the final hydrate saturation was 0.95. Since the initial gas saturation was high (0.80), the connectivity of the gas was also high, and it seemed as if the high connectivity of the gas was the cause of the fast hydrate formation. In addition, since the hydrate was formed by agitation, the mobility of the gas and water could be high, which might induce a faster formation. A clear color pattern in the hydrate was observed as formation occurred, indicated by the three yellow circles (2) in Figure 19. As the hydrate grew, it became darker in color, turning from light grey to black, which may indicate thicker hydrate films. After three minutes, the hydrate became lighter in color, turning from black to grey, and this color change may indicate that gas became consumed by water.

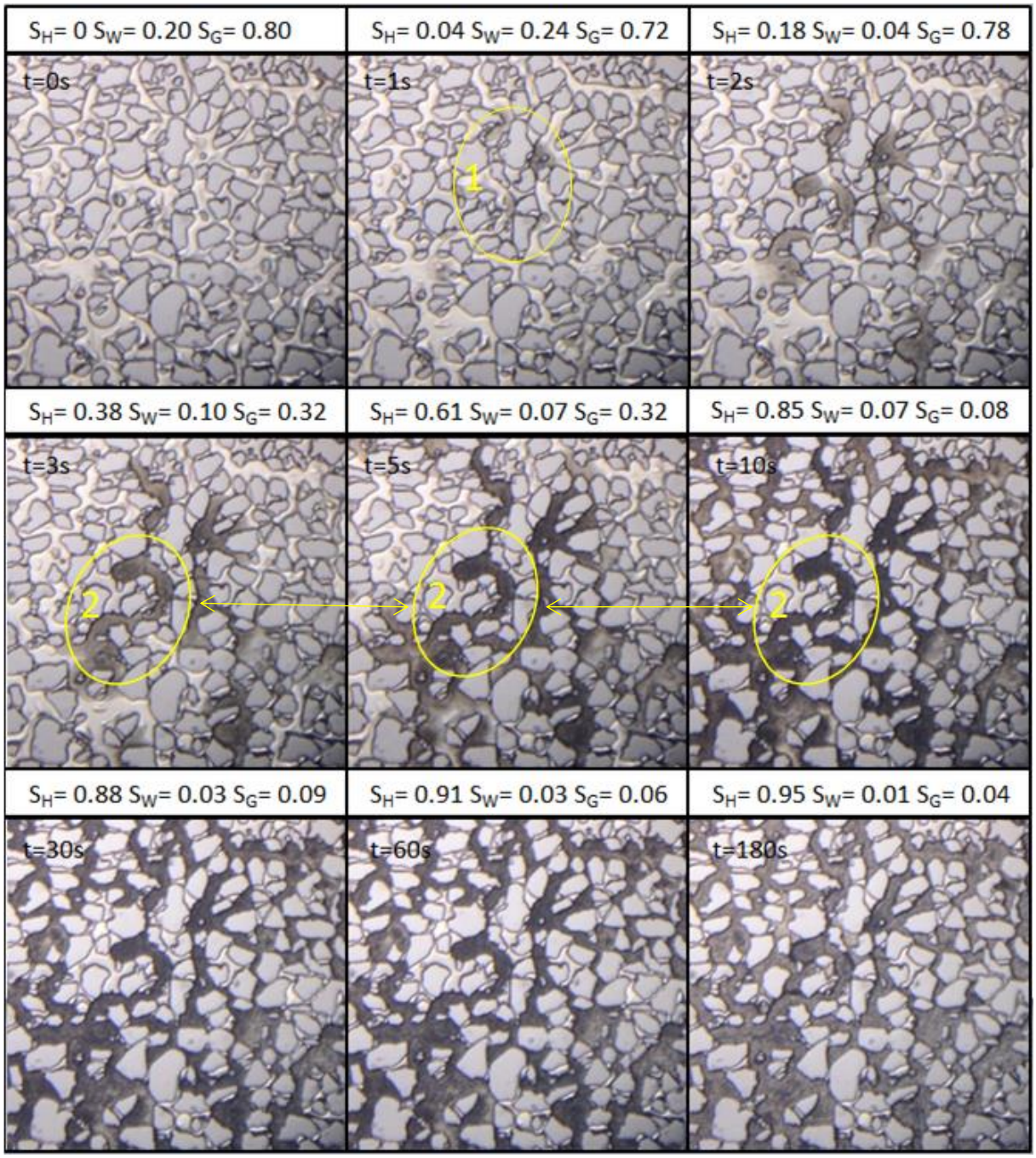

Figure 19: Image sequence for primary methane hydrate formation with deionized water at 46.5 bar with a constant temperature of 4.1°C (Formation experiment 7). Average porosity of 0.49±0.03. Image t=1s shows initial hydrate formation on the water-gas interface, indicated by the yellow circle (1). The three yellow circles (2) in images t=3s to t=10s illustrate that hydrate became darker as the formation continued, which may suggest thicker hydrate films. In images t=30s to t=180s hydrate became lighter, turning from black to greyish.

Water salinity of 2.0 wt% NaCl

Methane hydrate was formed statically with a water salinity of 2.0 wt% NaCl by increasing the pressure from 40 to 50 bar with a constant temperature of 4.1°C. The secondary hydrate formation process is shown in Figure 20, where initial hydrate formation occurred on the water-gas interface at the pore walls of two separate gas bubbles after 20 seconds. After 60 to 100 seconds, the hydrate was observed to grow from the water-gas interface and into the center of the pores. Since the initial water and gas saturation were approximately equal, gas bubbles were separated from each other. Consequently, the gas connectivity was low, and hydrate grew more heterogeneously than homogeneously. After 160 seconds, the hydrate saturation was 0.45, and several gas bubbles were observed remaining as gas rather than becoming hydrate. These free gas bubbles might be a consequence of the low connectivity of the gas. In addition, the hydrate was formed statically, which might limit the gas and water mobility compared to when hydrate was being formed by agitation.

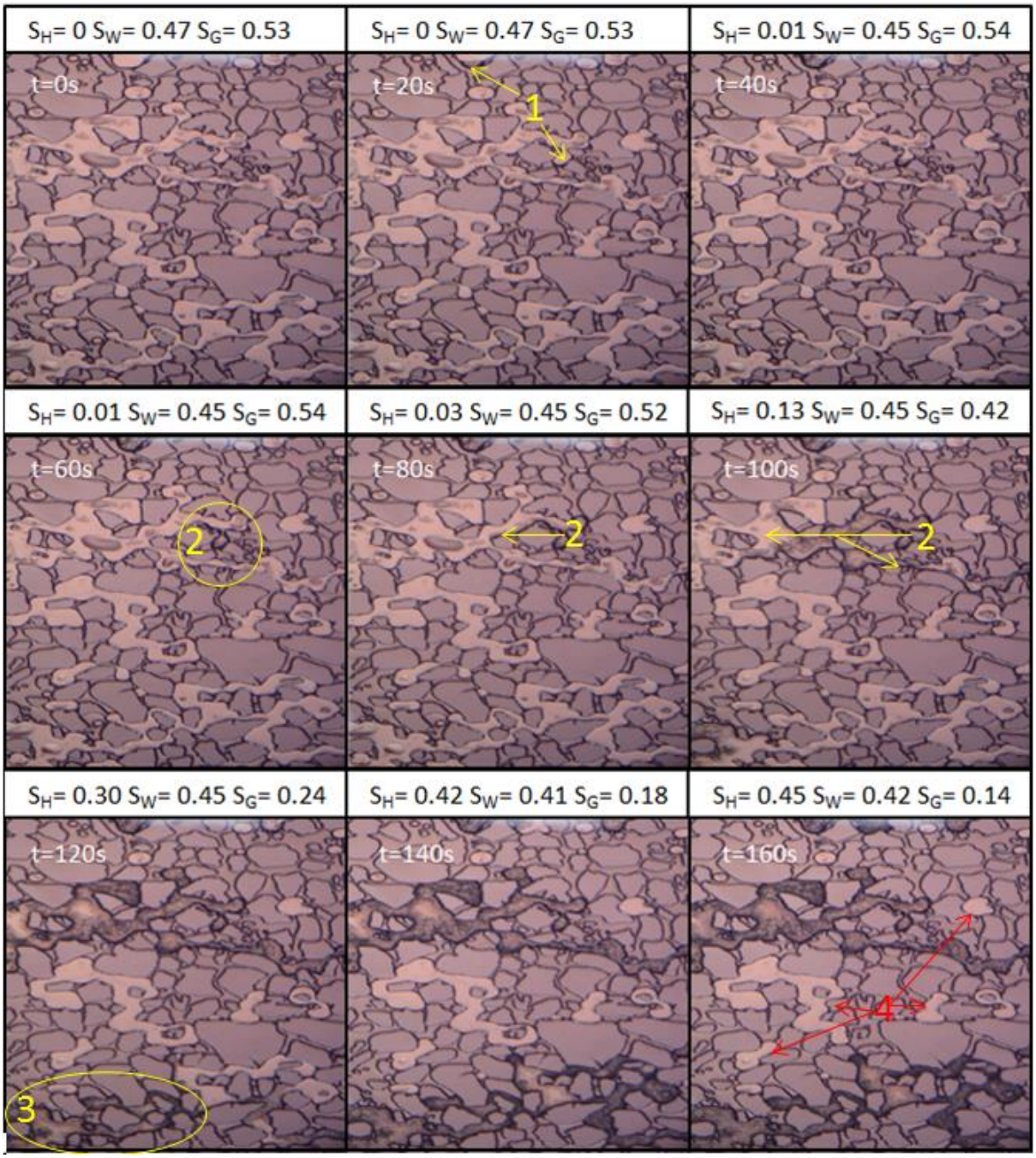

Figure 20: Image sequence for secondary methane hydrate formation with a water salinity of 2 wt% NaCl at 45.5 bar with a constant temperature of 4.1°C (Formation experiment 10). Average porosity of 0.47±0.01. Image t=20 shows initial hydrate formation on the water-gas interface, indicated by the two arrows (1). In images t=60s to t=100s hydrate grew along the water-gas interface before spreading further in the gas, indicated by the number 2. In image t=120s hydrate was observed to grow in a new location, indicated by the yellow circle (3). In image t=160 hydrate growth stagnated and several free gas bubbles remained, indicated by the red arrows (4).

Water salinity of 3.5 wt% NaCl

Methane hydrate was formed statically with a water salinity of 3.5 wt% NaCl by increasing the pressure from 42.5 to 52.5 bar with a constant temperature of 4.1°C. The secondary hydrate formation process is shown in Figure 21, where initial hydrate formation occurred on the water-gas interface near the pore walls after three seconds. Hydrate grew from the water-gas interface and inwards to the center of the pores. The water and gas saturation were initially approximately equal and gas bubbles were separated from each other, similar to what occurred in the secondary hydrate formation in Figure 20. Consequently, the connectivity between the gas bubbles was low. Even though the connectivity was low, most of the gas formed hydrate, and this may be explained by hydrate growth outside the field of view (gas may be connected together outside the field of view). After 240 seconds two gas bubbles still remained, and did not form hydrate. The grains seemed to have trapped the free gas bubbles, which inhibited hydrate growth.

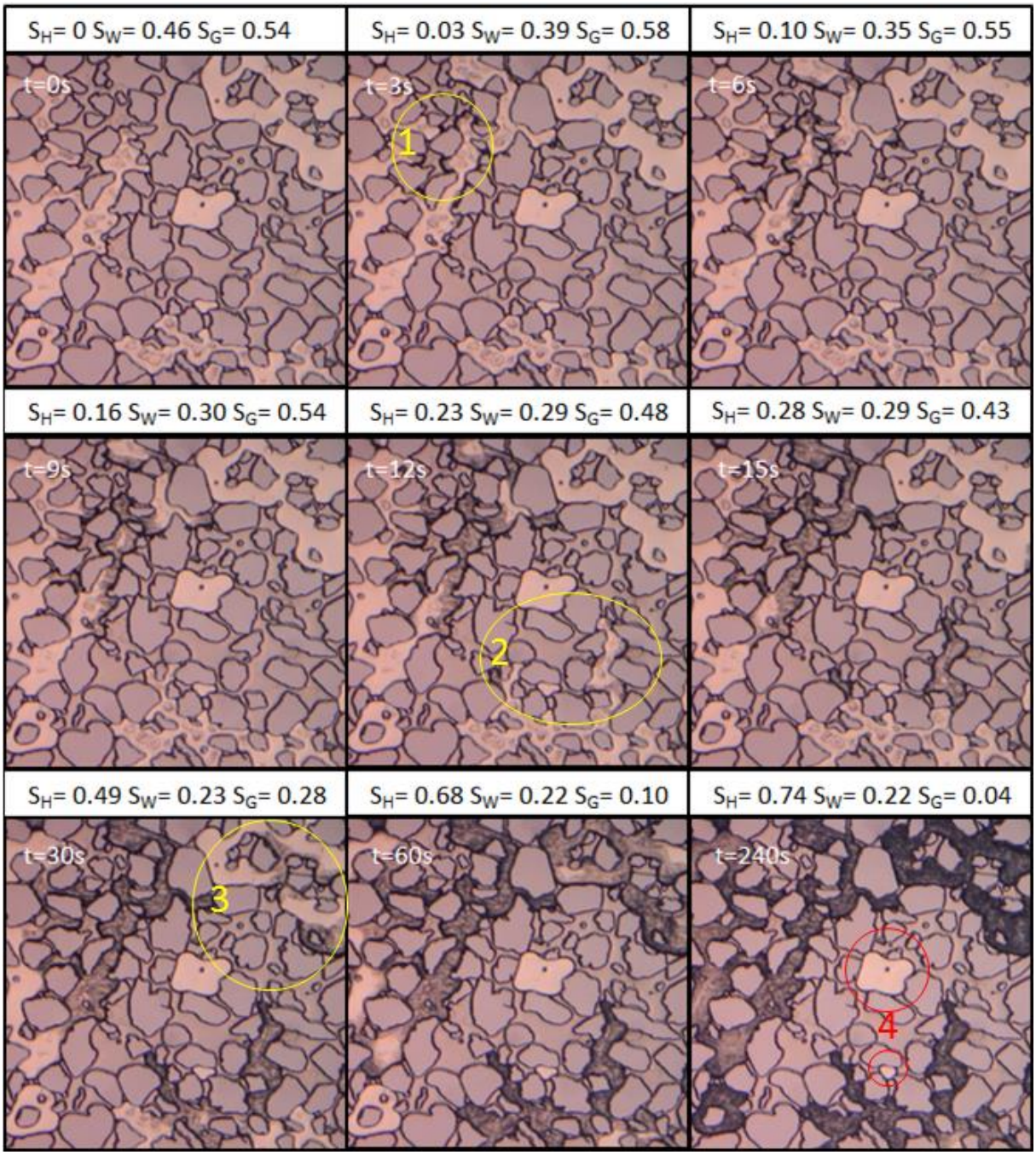

Figure 21: Image sequence for secondary methane hydrate formation with a water salinity of 3.5 wt% NaCl at 52.5 bar with a constant temperature of 4.1°C (Formation experiment 13). Average porosity of 0.47±0.04. Image t=3s shows initial hydrate formation on the water-gas interface, indicated by the yellow circle (1). In images t=12s and t=30s hydrate was observed to grow in two new locations, indicated by the yellow circles (2) and (3). In image t=240s, two free gas bubbles remained, indicated by two red circles (4).

Water salinity of 5.0 wt% NaCl

Methane hydrate was formed with a water salinity of 5.0 wt% NaCl by forcing agitation on the system at 83.4 bar with a constant temperature of 1.2°C. The primary hydrate formation process is shown in Figure 22, where initial hydrate formation was observed on the water-gas interface after five seconds. Because of the presence of several water films on top of the gas, hydrate initially grew from the center of the pores towards the water-gas interface at the pore walls, and vice versa. After ten seconds the hydrate saturation was 0.43, and dendritic formation characteristics were observed at the bottom of the image, indicated by the yellow circle (3) in Figure 22. Since the connectivity of gas was high, hydrate grew in all of the gas, and this resulted in a final hydrate saturation of 0.71. In addition, the mobility of water and gas may have been high, since the hydrate was formed by agitation.

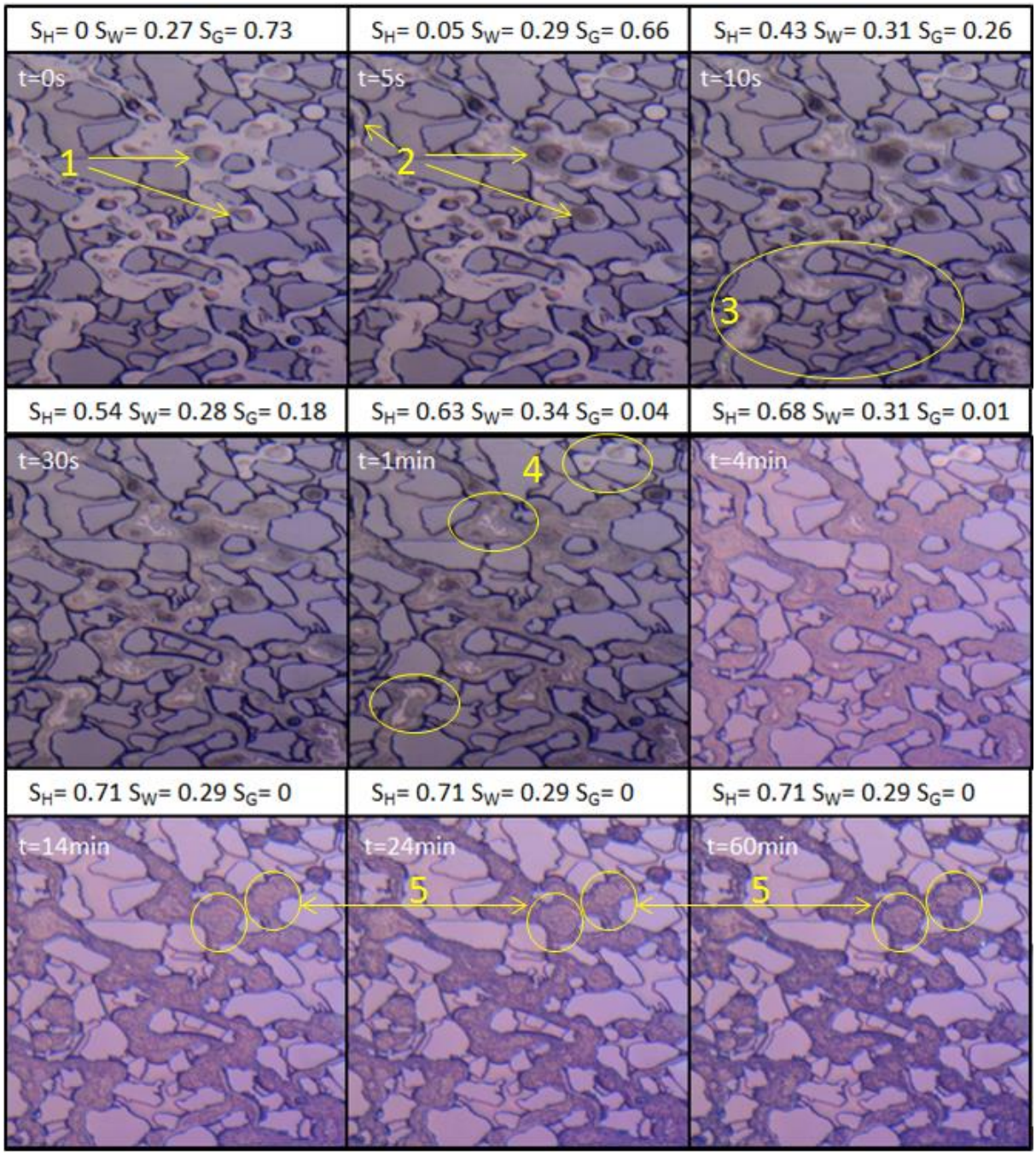

Figure 22: Image sequence for primary methane hydrate formation with a water salinity of 5.0 wt% NaCl at 83.4 bar with a constant temperature of 1.2°C (Formation experiment 19). Average porosity of 0.56±0.02. Several water films were observed in image t=0, and two of them are indicated by two yellow arrows (1). Image t=3s shows initial hydrate formation on the water-gas interface at the pore walls and around the water films, indicated by three yellow arrows (2). In image t=10s, hydrate was observed to grow in a dendritic manner, indicated by a yellow circle (3). In image t=1min, hydrate formation stagnated, leaving some gas, indicated by three yellow circles (4). In images t=14min to t=60min, hydrate was generally observed to become darker, except the areas connected to water films. These became more transparent, indicated by the six yellow circles (5).

4.1.2 Saturation profiles of hydrate formations

Following are four saturation profiles of water, gas and hydrate during hydrate formation, illustrated in Figure 23. These are saturation profiles for the same hydrate formations that were presented above in section 4.1.1.

Both 0 and 5.0 wt% NaCl apply to primary hydrate formations induced by agitation, while 2.0 and 3.5 wt% NaCl apply secondary hydrate formations created under static conditions. When hydrate was formed through agitation, there was a sharp change in the hydrate saturation and accordingly a sharp decrease in the water and gas saturations. The initial formations happened rapidly (<30 seconds) and stagnated over time. When hydrate was formed statically, the hydrate saturation increased gradually before it stabilized, and correspondingly, the water and gas saturations decreased gradually before flattening out. For secondary hydrate formation, the time before considerable hydrate saturation was reached, was slow (>30 seconds).

When hydrate was being formed with saline water of 5.0 wt% NaCl, the initial formation was rapid, but stagnated over time. This may be attributed to hydrate becoming stable towards local high-saline water phases. This observation will be discussed in section 4.1.3.

An interesting observation of the 2D saturation measurements is the relation between the hydrate and gas saturation. The hydrate and gas curves were almost a reflection of each other because most of the visible hydrate was formed in gas. Compared to the gas saturation, the water saturation decreased more randomly and independent of the hydrate saturation. The random decrease in water saturation seemed to be dependent on the initial water saturation and the redistribution of gas and hydrate.

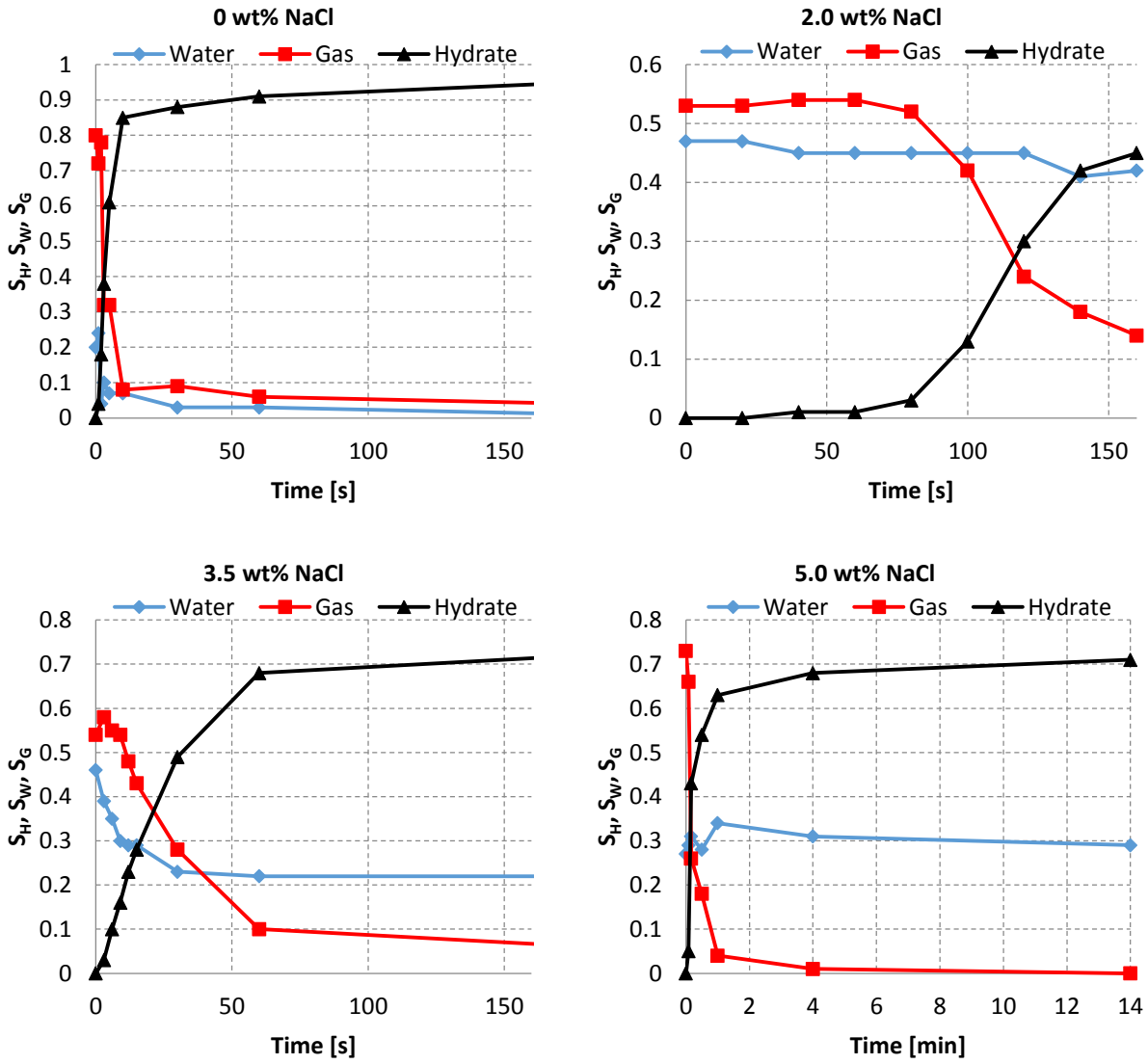

Figure 23: Estimated 2D saturation profiles for water salinities of 0, 2.0, 3.5 and 5.0 wt% NaCl over time when methane hydrate was being formed. Hydrate, water and gas are represented by the colors black, blue and red, respectively.

4.1.3 Interpretation of the observations

In this section, key observations from the image sequences in Figures 19 to 22, as well as observations from the other hydrate formation experiments, will be interpreted. First, hydrate formation patterns will be discussed, then the observed differences between primary and secondary formation, and finally, the differences between patterns of hydrate formation with deionized and saline water.

Hydrate formation patterns

Hydrate formation was initiated on the water-gas interface for all formation experiments, whether the water was deionized or saline. Similar observations have been made for deionized water in glass micromodels (Tohidi et al., 2001, Katsuki et al., 2007) and silicon micromodels (Hauge et al., 2016). Figure 24A illustrates a cross-sectional 3D perspective of the water and gas distribution in the micromodel. Because of the water-wet nature of the pore network and cross-sectional shape of the pores, water will accumulate in the corners of the pores, and gas will be located in the center. A curved water-gas interface will develop along the sides, resulting in thick water films in the corners. The water molecules bound to the water-wet surface may reduce the chemical potential for the molecules in vicinity of the grain (Clennell et al., 1999). Consequently, hydrate films are allowed to form on the water-gas interface because the local accessibility of water is high (Hauge et al., 2016).

After the initial hydrate growth, the hydrate will grow from the pore walls towards the pore center, as illustrated in Figure 24B. The hydrates will most likely grow as films along the water-gas interface and are highly dependent on available water to continue growing. Water may migrate along the hydrate films from the grain surface or neighboring water-filled pores. If there already is a water film on the gas, the hydrate growth may be expedited towards the center of the pores because the water is easily available. The effect of water films on the gas during hydrate formation was observed in Figure 22. Not only was the hydrate growth towards the center of the pores accelerated, but hydrate initially grew in the center of the pores as well. As a consequence, hydrate grew from the pore walls to the center of the pores as well as from the pore center to the pore walls.

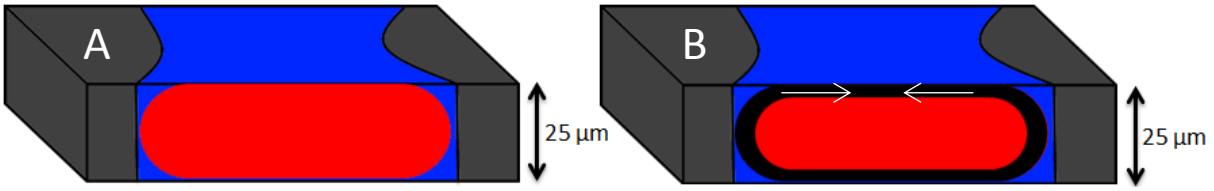

Figure 24: Cross-sectional illustration of the pore network in the micromodel and its fluid distribution (modified from Hauge et al (2016)). The height of the pores is 25µm, while the width may vary. The water-wet nature and cross-sectional shape of the micromodel make water (blue) accumulate in the pore corners and gas (red) center in the pore. Hydrate (black) forms on the water-gas interface.

Hydrate growth in the gas phase

Hydrate growth from the pore walls towards the pore center is illustrated in Figure 25. A free gas bubble was captured by a water film, and later hydrate was formed. The water film migrated from the water-gas interface and propagated further into the center of the gas bubble. When the water film had totally encapsulated the free gas phase, the phase became darker, which indicates hydrate formation.

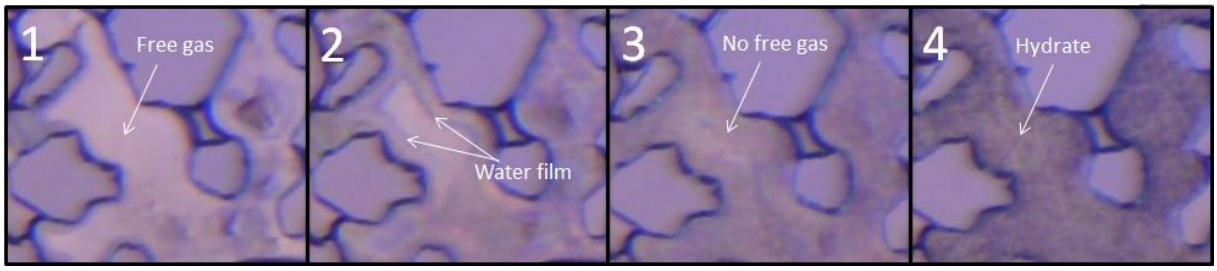

Figure 25: Image sequence where hydrate was observed to grow from the pore wall to the center of the pore (Formation experiment 16). Image 1 shows a free gas bubble just before it was encapsulated by water. Image 2 (8s later) shows the water film migrating from the water-gas interface towards the center of the pores. Image 3 (50s later) shows how the water film totally consumed the gas bubble. Image 4 (2min later) shows that hydrate has been formed.

Hydrate was also observed to grow as a consequence of what seemed like transfer of gas molecules through the water, as illustrated in Figure 26. The slight color change in the water seemed to indicate a channel having developed along the grain, from the hydrate to a gas bubble. First, hydrate started to grow on the water-gas interface surrounding the gas bubble, and finally hydrate was formed throughout the whole gas bubble. The gas molecules may have been transferred from the hydrate phase if the gaseous methane was not yet enclosed by the hydrate films. This observation corroborates results from previous work (Katsuki et al., 2007).

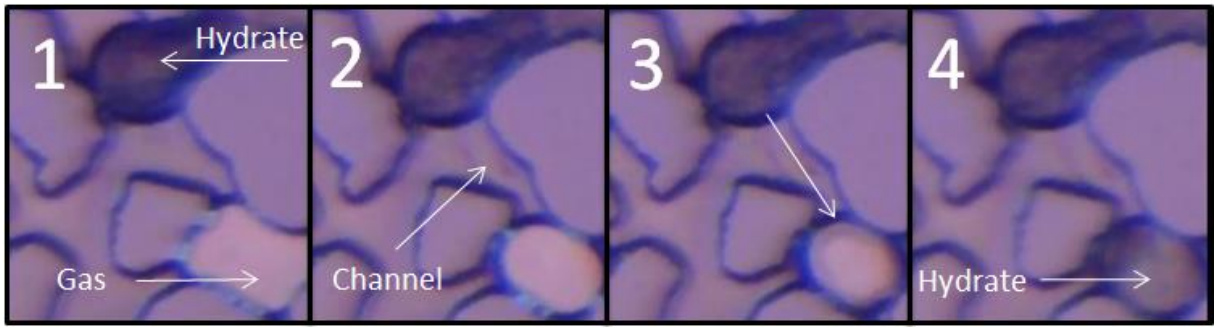

Figure 26: Image sequence where hydrate was observed to grow due to transfer of gas molecules (Formation experiment 17). Image 1 shows hydrate and a gas bubble separated by water. Image 2 (2min later) shows a channel that developed along the grain, from the hydrate to a gas bubble. Image 3 (2s later) shows hydrate forming on the water-gas interface of the gas bubble. Image 4 (10s later) shows hydrate growth in the entire gas bubble.

Hydrate growth in the water phase

A dendritic hydrate growth in the water phase was observed in formation experiment 16, as illustrated in Figure 27. The hydrate crystals seemed to grow from the overlying gas hydrate phase and downwards into the water phase. Initially the hydrate crystals were observed as faceted, but as the growth commenced, the crystals stretched out and gained the characteristic dendritic shape. The crystal growth into the water phase may be a result of methane migration from the overlying hydrate film (Katsuki et al., 2007). Uchida et a. (1999) observed the formation process of hydrate film at the interface between water and CO_2 in a bulk phase, and suggested that hydrate films mainly grow in the water phase. Out of all the experiments performed, this was the only case where hydrate was observed to grow into the water phase. Due to the low temperature (1.3°C) and high salt concentration (5.0 wt% NaCl), the observed growth might be caused by recrystallization of precipitated salt crystals during hydrate formation. Since the growth occurred beneath the water phase, it was hard to identify the actual source.

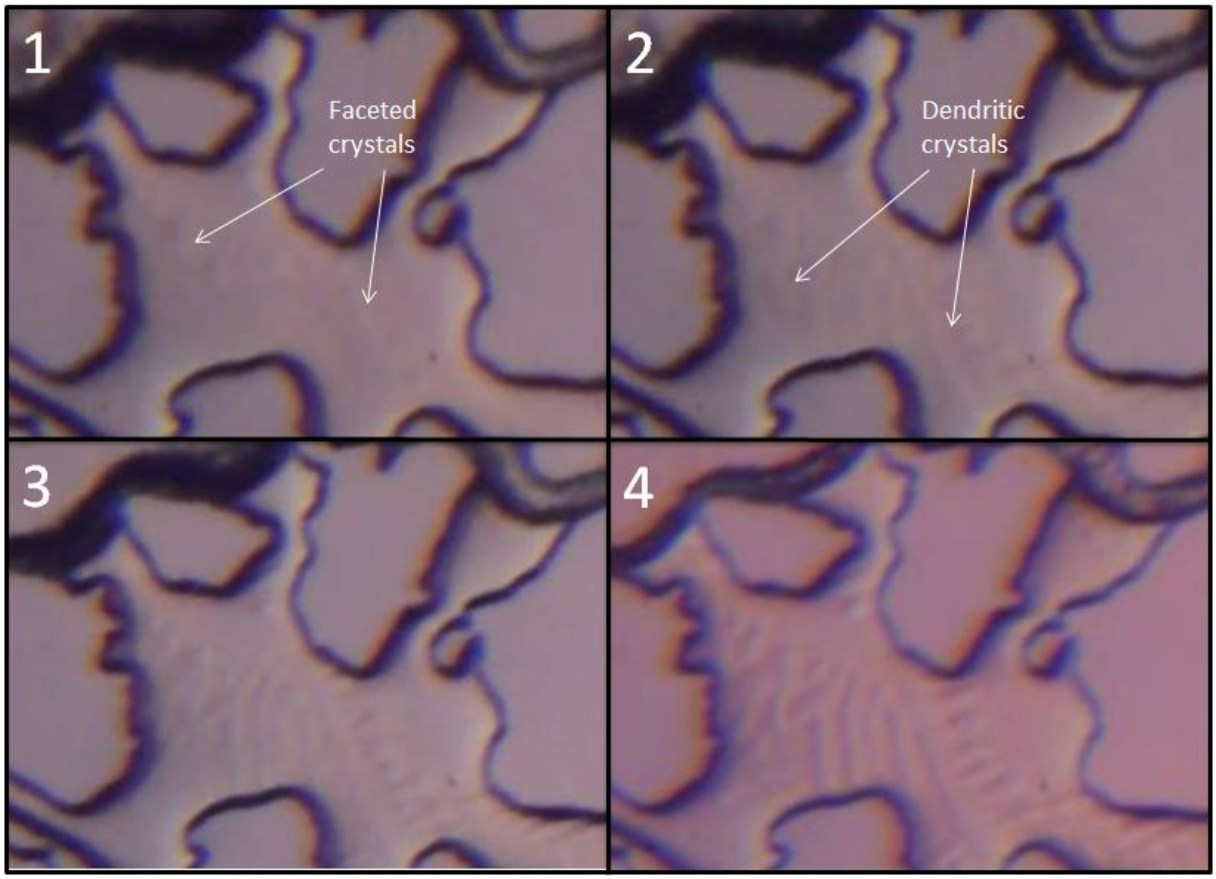

Figure 27: Image sequence where dendritic hydrate or salt crystals was observed to grow in the water phase (Formation experiment 16). The images 1 to 3 are taken within 3 minutes of the initial formation, while image 4 is taken 1 hour after the formation. Image 1 shows the first observed faceted crystals in the water phase. In images 2 to 4 the crystals are gaining a dendritic characteristic.

Complete hydrate recrystallization

In Figure 28, hydrate was observed to completely recrystallize from hydrate in gas to hydrate in water. Water consumed all of the gas in the micromodel, and this resulted in mostly faceted hydrate crystals and some dendritic hydrate crystals. Initially there was a large gas phase, but as the formation commenced, a water film grew around it. When the water film had surrounded the gas phase, hydrate was formed along the edges of the gas phase. It seemed like the gas in the center of the pore became completely consumed, which resulted in a sudden collapse. Consequently, gas was replaced by water. Since the image only represents a 2D view, it was hard to determine whether the water already existed beneath the gas or if it had been transported there due to the hydrate formation. The trend for this specific hydrate formation was that the hydrate films only grew along the grain walls and not in the center of the pores. After three hours, the hydrate film became coarser and considerably thinner than in its initial state, which might be due to the water slowly consuming the gas. After ten hours, all of the gas was completely consumed in the water phase and recrystallized. This was observed throughout the entire micromodel.

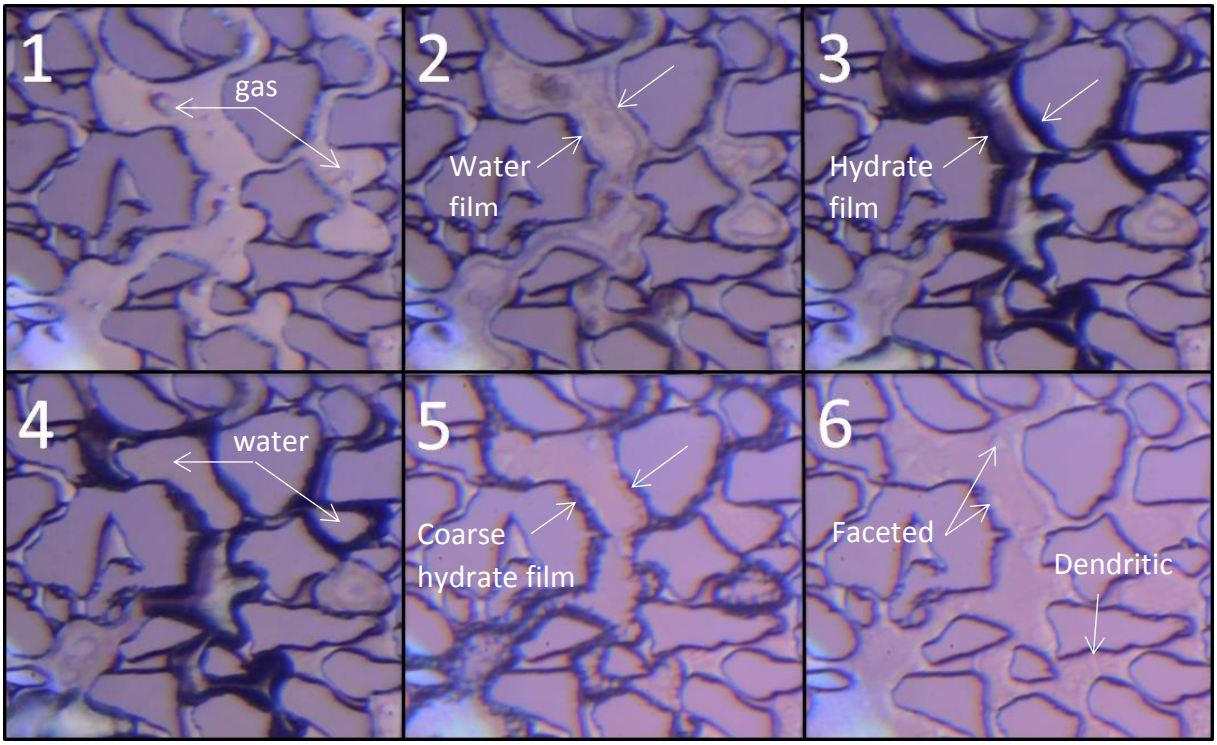

Figure 28: Image sequence where hydrate was completely recrystallized (formation experiment 18). The sequence represents hydrate formation over ten hours, the images 1-4 are taken within a timespan of ten seconds, image 5 is taken after three hours, and image 6 is taken after ten hours. The images 1 to 3 show gas being encapsulated by a water film, and forming hydrate films. Image 4 shows hydrate films along the grains with water in the center of the pores. Image 5 shows the initial recrystallization where the hydrate films became coarser. Image 6 shows complete recrystallization of the hydrate, and both faceted and dendritic hydrate crystals are present.

The observations in Figure 27 and Figure 28, where hydrate grew in water, add more uncertainty to the saturation measurements made in this thesis. When the hydrate saturation was measured, hydrate was only assumed to be located where the images were black, but these observations make it likely that water can lie under gas and that hydrate can grow in water. However, for all the other experiments little to no hydrate growth was observed in water. The 2D saturation measurements were made to gain an idea of how water and gas were redistributed and influenced during hydrate formation and dissociation.

Differences between primary and secondary hydrate formation

During all the secondary hydrate formations, the “memory effect” (described in section 1.1.9) was evident. Secondary hydrate formation refers to when hydrate was formed just after hydrate was dissociated. Hydrate was regenerated at pressures much lower than those required for primary hydrate formation. The “memory effect” also stayed intact when the pressure was reduced, as well as when the temperature was increased. It seems like hydrate not only has a thermal history, but also a pressure history. It was hard to determine whether the hydrate structures remained as residual structures in the micromodel or if some gas had been adsorbed in the water solution prior to dissociation. Most likely, residual structures were left behind in the thick water films in the pore corners. There were no indications that the gas was dissolved in the water phase.

Two differences between primary and secondary hydrate formation were observed, independent of whether the water was deionized or saline:

1. Primary formation was faster than secondary formation.
2. Primary formation was more homogeneous than secondary formation.

After primary hydrate formation, almost all of the visible gas was converted to hydrate, whereas after secondary formation several free gas bubbles remained. Based on the experimental results, the common denominators were how the hydrates were formed and the connectivity of the gas. When the system was agitated, the driving forces and gas connectivity were high. When the system was agitated, there was a high supply of gas, continuously supporting the hydrate growth. In contrast, when hydrate was formed statically, the driving forces and gas connectivity were low. For statical hydrate formation, also the fluid supply was low since no additional gas (or water) was introduced in the system. With low driving forces and low fluid supply, the hydrate growth is highly dependent on, among others, the connectivity of gas and water phases and the diffusivity (Hauge et al., 2016). As observed in Figure 20 and Figure 21, for secondary hydrate formation the gas connectivity was low. Gas connected to where hydrate was initiated, always experienced hydrate growth. In contrast, the gas bubbles not connected to where hydrate was initiated, remained as gas, and they were dependent on mass transfer from the already existing hydrate through the water. The mass transfer may be inhibited by the hydrate films on the interface between gas and water (Kvamme et al., 2007). Also, during hydrate growth, all regions on the initial film are competing for the available molecules in order to obtain further growth (Kvamme et al., 2007). Consequently, hydrate growth may be restricted to the initial location rather than spread to the isolated gas phases, due to low connectivity and restricted diffusion. In addition, the endothermic nature of hydrate formation may counteract the formation in a higher degree for low driving forces than for high driving forces.

Difference between patterns of hydrate formation with deionized and saline water

In the experiments two distinct differences were recognized between primary hydrate formation with deionized water and saline water. First and foremost, primary hydrate formation with saline water of 3.5 wt% NaCl and higher, required greater driving forces than formation with deionized water and water with a salinity of 2.0 wt% NaCl. For each experiment the pressure and temperature was set to approximately 83.0 bar and 4.0°C, respectively. If hydrate did not form under the initial conditions, the pressure was increased and/or the temperature decreased. On some occasions, agitation had to be forced several times before hydrate nucleation commenced. When the initial salinity was 3.5 wt% NaCl and higher, the salt content of the water seemed to be the limiting factor for hydrate formation. Husebø et al. (2009) observed similar trends during hydrate formation in Bentheim sandstone, and believed that salt in the water phase was the limiting factor if the initial salinity was higher than 4.0 wt% NaCl.

The other difference for primary hydrate formation with deionized and saline water was the formation rate, determined by the color change during hydrate growth. During the formation process, light areas may persist within the dark hydrate crystals, and Tohidi et al. (2001) describes these areas as encapsulated gas bubbles prior to complete conversion to clathrate. For deionized water, the light areas were only observed in hydrate for the first 30 seconds. While for saline water (5.0 wt% NaCl), the light areas were observed in hydrate for the first 14 minutes. When hydrate is formed with saline water, salt ions may precipitate out from the water. These precipitated salt ions can result in local water phases with high salinity along the water-gas interface, and thereby inhibit further hydrate growth. Hydrate was formed significantly faster for deionized water than for saline water, and this suggests that local water phases with high salinity initially inhibited hydrate formation. In Figure 29, hydrate growth was inhibited by salt crystals located in a water pocket surrounding a grain, but hydrate had already grown in the surrounding gas, and subsequently, a hydrate front propagated into the gas and connected to the water pocket. When the hydrate front connected to the water pocket, hydrate immediately started to grow. Since salt does not take part in hydrate formation, it seemed as if the salt had been transported elsewhere in the model.

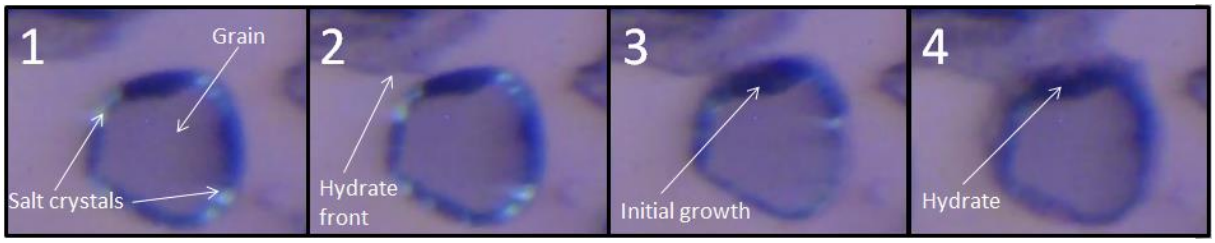

Figure 29: Image sequence where hydrate formation is initially inhibited by salt ions located in a water pocket surrounding a grain (Formation experiment 17). Images 1 to 4 are taken with three seconds intervals over a 12 second period. Image 1 shows salt crystals in the water pocket. Image 2 shows the hydrate front propagating in the gas. Image 3 shows the initial growth, where the hydrate front is connecting to the water pocket. Image 4 shows hydrate growing around the grain, and no salt crystals are observed.

The pattern of secondary formation with deionized water and secondary formation with saline water seemed more similar than the pattern of primary formation with deionized and saline water. Figure 30 shows an image of secondary hydrate formation with deionized water. The image was taken after the formation had stagnated. Here, several gas bubbles remained free of hydrate, and this was similar to what happened during secondary hydrate formation with saline water. The only detectable difference was the initial formation pressure, which increased with increased salinity, as expected.

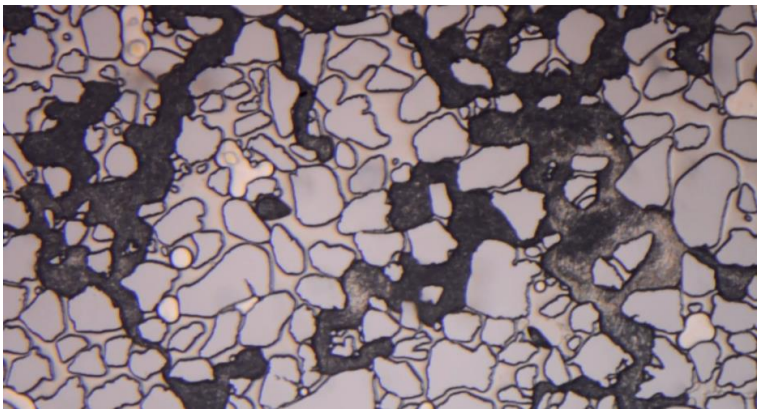

Figure 30: Image 2 minutes after secondary hydrate formation with deionized water at 45.0 bar with a constant temperature of 4.1°C (Formation experiment 8). Several gas bubbles remained as gas and not as hydrate.

4.2 Hydrate dissociation by depressurization

There were performed a total of eight methane hydrate dissociations by depressurization, whereof two with 0 wt% NaCl, two with 2.0 wt% NaCl, three with 3.5 wt% NaCl and one with 5.0 wt% NaCl. All the dissociation by depressurization experiments are summarized in Table 6. A stepwise pressure-reduction technique was used when hydrate was dissociated. The pressure was lowered to approximately three bars above the theoretical depressurization pressure, and then reduced in increments of 0.7 bar. It was observed that hydrate dissociation transpired over a range of pressure values. Since the volume in the micromodel is small, the dissociation process had to be evaluated by studying the images. Consequently, the estimated pressure values may be uncertain. The initial dissociation pressure was identified by locating the significant change in the hydrate saturation. The temperature was kept constant at approximately 4.0°C through the pressure reduction. It was difficult to maintain a constant temperature during the dissociation experiments. When the temperature in the refrigerated bath circulator was changed by 0.1°C, the measured temperature in the still water could increase/decrease by 0.2°C. In addition, the temperature in the still water could fluctuate due to the laboratory room temperature. Four of the hydrate dissociations by depressurization are presented as image sequences in section 4.2.1, and each one represents a different saline solution. The uncertainties of the values are discussed in appendix 7.1. The dissociation pressure-paths from initial dissociation to complete dissociation are illustrated in Figures 51 to 54 in appendix 7.2.

Table 6: Methane hydrate dissociation by depressurization with water salinities of 0 to 5.0 wt% NaCl. The column titled "Pressure steps" in the table refers to the number of pressure steps it took from initial dissociation to complete dissociation.

Exp.	**Salinity ±0.01 [wt%]**	**Initial pressure ±1.4 [bar]**	**Initial dissociation pressure ±1.4 [bar]**	**Complete dissociation pressure ±1.4 [bar]**	**Pressure steps (0.7 bar)**	**Temperature ±0.2 [°C]**
1	0	42	38.6	35.1	6	4.1
2*	0	46.0	38.9	38.2	2	4.1/2
3	2.0	45.6	39.4	38.6	2	4.1
4*	2.0	44.2	42.8	39.3	6	4.0
5	3.5	49.0	44.6	43.0	2	4.3
6*	3.5	49.3	45.1	41.6	5	4.2
7	3.5	48.8	44.9	39.0	9	4.1
8*	5.0	53.3	49.1	42.1	11	3.9

**The dissociations being presented as image sequences.*

4.2.1 Image sequences for hydrate dissociation by depressurization

Following are four image sequences for hydrate dissociation by depressurization, presented in Figures 31 to 34. The saline solution was increased for every sequence, and each sequence is presented with decreasing pressure. If significant changes were observed in the micromodel during one pressure step, the image sequences may contain several images from the same pressure step. The experiments were conducted to observe if there were any differences between the pattern of dissociation with deionized water and the patterns of dissociation with saline water. The observed dissociation trend was that hydrate melted from the center of the pores to the water-gas interface at the pore walls. A detailed interpretation of the saturation profiles and the observations is given in section 4.2.2 and 4.2.3, respectively. In section 4.3 the experimental observations of dissociation by pressure reduction will be compared to the experimental observations of dissociation by thermal stimulation.

Deionized water

Methane hydrate was dissociated with deionized water by reducing the pressure in increments of 0.7 bar and keeping a constant temperature of 4.1°C, as illustrated in Figure 31. The initial pressure was 46.0 bar, and hydrate was completely dissociated when the pressure was 38.2 bar. The initial hydrate saturation was high (0.92), covering almost all of the pore space. Only one free gas bubble was observed in the field of view images. From 46 to 40.3 bar (eight pressure steps) minimal changes in the water, gas and hydrate were observed. At 38.9 bar initial hydrate dissociation occurred in the center of the pores and thereby water and gas were mobilized. Hydrate dissociated from the center of the pores toward the water-gas interface at the pore walls. The connectivity of the hydrate was high, and from 38.9 to 38.2 bar all of the hydrate was dissociated. The final water and gas saturation was approximately equal, which indicates that water and gas have been substantially redistributed. In Figure 31, it is worth noticing the water phase indicated by the blue circle (4), and the hydrate phase indicated by the yellow circle (5). Here, the water seemed to inhibit the hydrate from dissociating. Only when the gas was mobilized and replaced the water, the hydrate dissociated. The mentioned dissociation behavior will be discussed further in section 4.2.3.

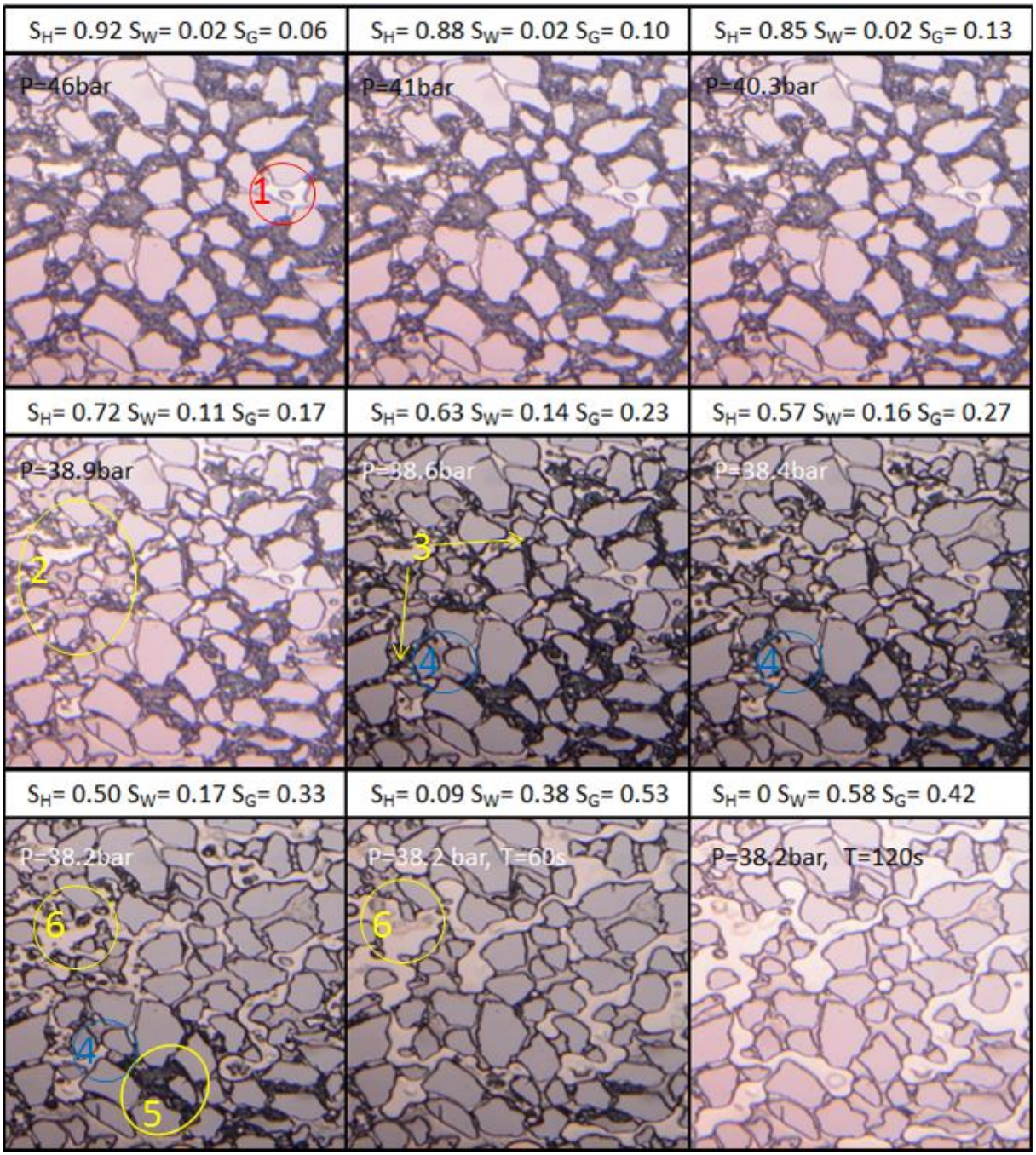

Figure 31: Image sequence for methane hydrate dissociation by depressurization with deionized water with a constant temperature of 4.1°C (Depressurization experiment 2). Average porosity of 0.49±0.02. Image P=46bar shows the initial hydrate distribution in the field of view, where only one free gas bubble is observed, indicated by the red circle (1). In image P=38.9 the hydrate starts to dissociate, indicated by the yellow circle (2). In images P=38.6bar to P=38.2bar, T=120s, hydrate is completely dissociated. The two yellow arrows (3) indicate the directions in which hydrate dissociated. Water is observed to initially inhibit hydrate dissociation, as indicated by the three blue circles (4). The hydrate phase that was inhibited, is indicated by a yellow circle (5). Hydrate was observed to persist in the center of the pores due to water films, as indicated by the two yellow circles (6).

Water salinity of 2.0 wt% NaCl

Methane hydrate was dissociated with saline water of 2.0 wt% NaCl by reducing the pressure in increments of 0.7 bar and keeping a constant temperature of 4.0°C, as illustrated in Figure 32. The initial pressure was 44.2 bar, and hydrate was completely dissociated when the pressure was 39.3 bar. Hydrate was distributed in most of the pores and had an initial saturation of 0.82. Some gas and water was trapped in between grains. After 180 minutes at 42.8 bar, initial hydrate dissociation occurred in the center of the pores and dissociated towards the water-gas interface at the pore walls. After initial hydrate dissociation, the hydrate saturation remained stable at 0.62-0.65 for four pressure steps. Finally, after eight minutes at 39.3 bar, the hydrate saturation plummeted, leaving the water and gas saturation approximately equal. The connectivity of the hydrate was high, and the dissociation was homogeneous throughout the pores. Hydrate was observed to remain in the center of the pores due to water films, as indicated by the two yellow circles (3) in Figure 32. The hydrate films connected to the water films will be discussed further in section 4.2.3.

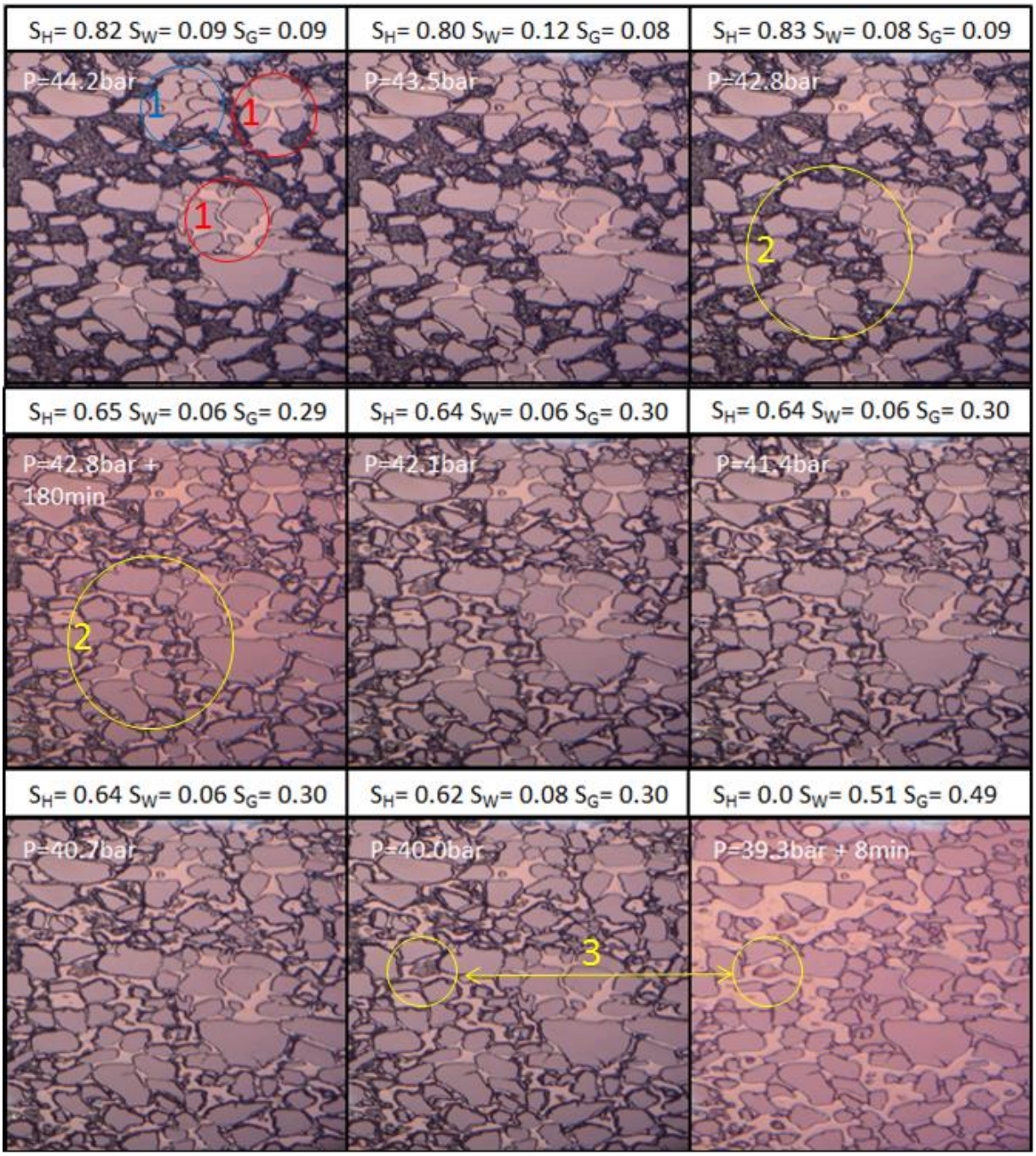

Figure 32: Image sequence for methane hydrate dissociation by depressurization with 2.0 wt% NaCl with a constant temperature of 4.0°C (Depressurization experiment 4). Average porosity of 0.46±0.02. In images P=44.2 to P=42.8 bar, the water, gas and hydrate distribution remain almost constant. Water and two free gas bubbles are observed to be trapped in between the grains, as indicated by one blue (1) circle and two red (1) circles. Image P=42.8bar + 180min shows the initial hydrate dissociation location, indicated by the two yellow circles (2). In images P=40.0 bar and P=39bar + 8min the connection between hydrate films and water films are pointed out, indicated by the two yellow circles (3).

Water salinity of 3.5 wt% NaCl

Methane hydrate was dissociated with saline water of 3.5 wt% NaCl by reducing the pressure in increments of 0.7 bar keeping a constant temperature of 4.2°C, as illustrated in Figure 33. The initial pressure was 49.3 bar, and hydrate was completely dissociated after 7 hours, when the pressure was 41.6 bar. The initial hydrate saturation was high (0.74), but the hydrate was separated into two phases by gas and water. Consequently, the hydrate connectivity was low. Initial hydrate dissociation occurred at 45.1 bar, and then hydrate dissociated from the center of the pores to the water-gas interface at the pore walls. From 45.1 to 41.6 bar, the hydrate saturation decreased steadily from 0.62 to 0.40. At 41.6 bar the hydrate continued to decrease, and after 7 hours all hydrate was dissociated. Because of the low connectivity of the hydrate, dissociation occurred more heterogeneously than homogeneously. Due to the heterogeneous manner, gas and water was redistributed during the hydrate dissociation. Hydrate was even observed to grow during the dissociation process, from ten seconds to eight minutes at 41.6 bar, indicated by the three yellow circles (4) in Figure 33. The hydrate growth is believed to happen because of high salt content in the water, and this will be discussed further in section 4.2.3.

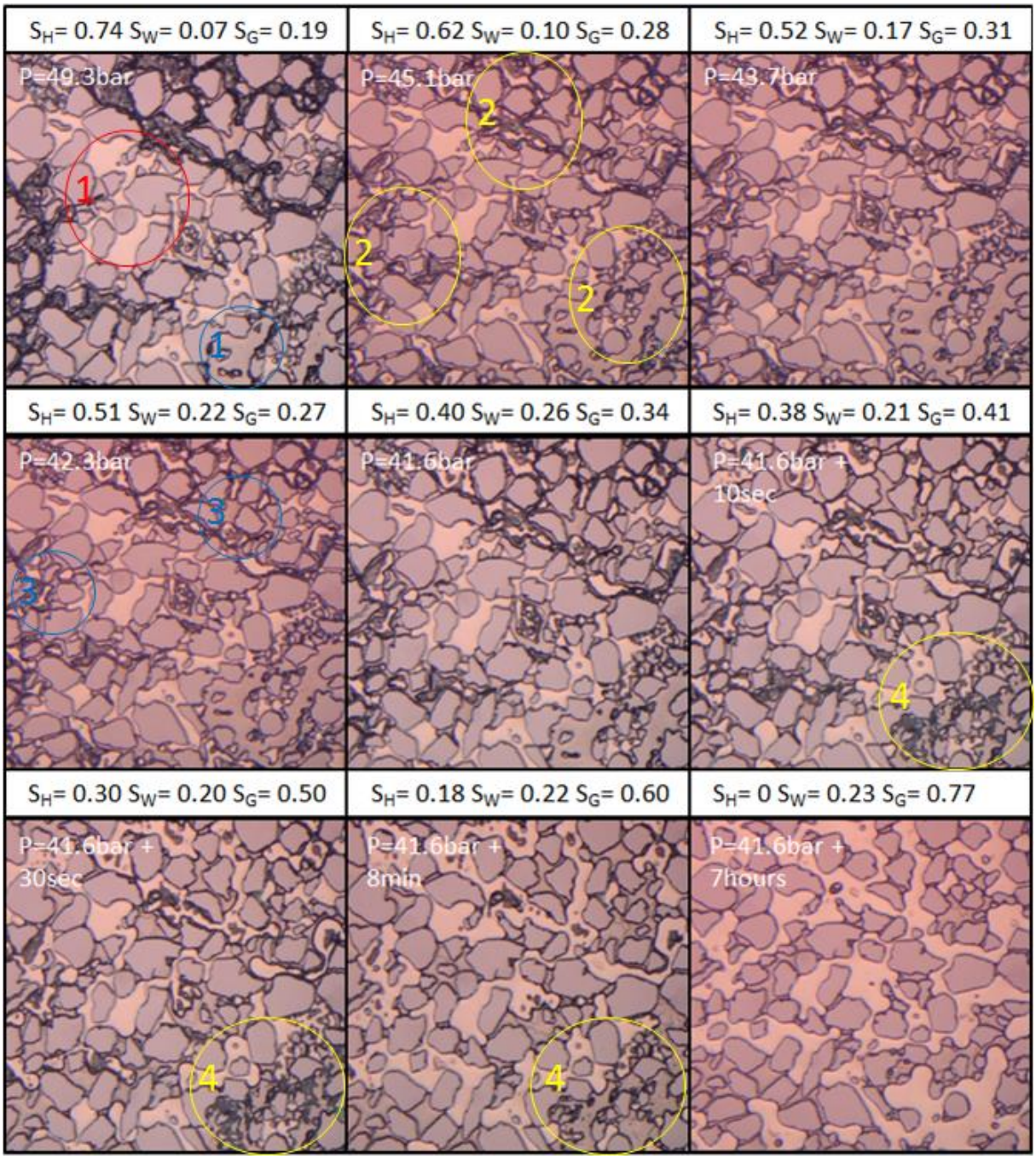

Figure 33: Image sequence for methane hydrate dissociation by depressurization with 3.5 wt% NaCl with a constant temperature of 4.2°C (Depressurization experiment 6). Average porosity of 0.46±0.06. Image P=49.3bar shows the initial hydrate distribution. Gas and water separates the hydrate in two, indicated by the red and blue circles (1). Image P=45.1bar shows the initial hydrate dissociation location, indicated by the three yellow circles (2). In image P=42.3bar, redistribution of water is observed, indicated by the two blue circles (3). In images P=41.6bar + 10sec to P=41.6bar + 8min, hydrate is observed to grow in the corner, as indicated by the three yellow circles (4).

Water salinity of 5.0 wt% NaCl

Methane hydrate was dissociated with saline water of 5.0 wt% NaCl by reducing the pressure in increments of 0.7 bar keeping a constant temperature of 3.9°C, as illustrated in Figure 34. The initial pressure was 53.3 bar, and hydrate was completely dissociated when the pressure was 41.6 bar. Hydrate films were initially scattered in the gas, and several of the hydrate films in the center of the pores remained there until the system had been completely dissociated. From 53.3 to 49.1 bar (six pressure steps), the hydrate saturation was observed to increase rather than decrease. The hydrate saturation seemed to increase due to redistribution of gas and water and due to potential hydrate growth. This observation will be discussed further in section 4.2.3. After 26 minutes at 49.1 bar, initial hydrate dissociation occurred, and the hydrate saturation was reduced from 0.67 to 0.24. The sudden reduction may be caused by the high presence of salt crystals, which increases the required pressure for hydrate to be stable. At the next pressure step (48.4 bar) hydrate was reduced even more (0.24 to 0.07). The dissociation process stagnated and did not dissociate completely before 41.4 bar, ten pressure steps later, when the pressure was 41.4 bar. Due to the scattered nature of hydrate, hydrate was both dissociated from the center of the pore to the pore walls and vice versa. Hydrate patches, left mostly in the center of the gas, seemed to be bound to the hydrate structure and therefore required greater driving forces (reduced pressure) to dissociate.

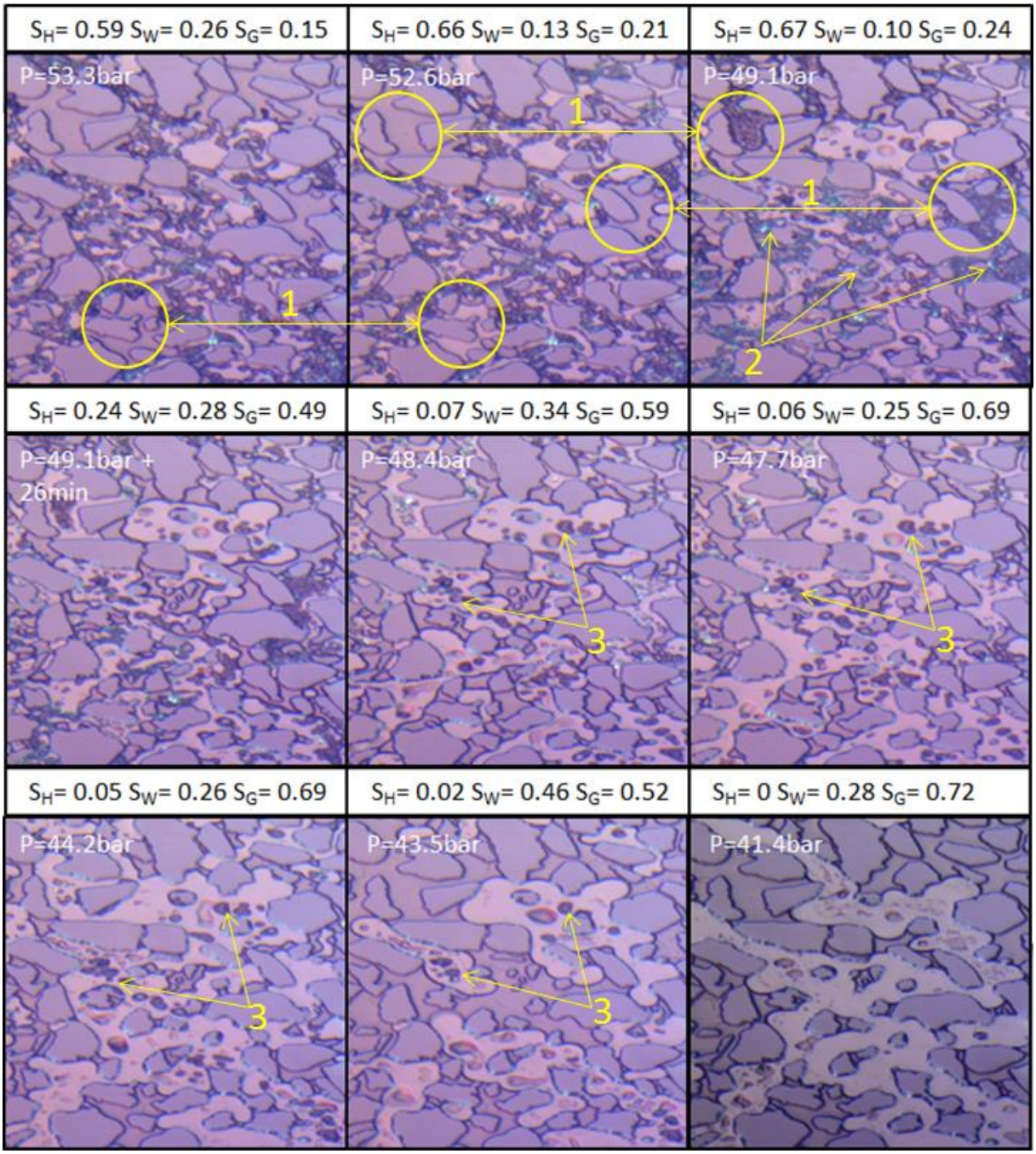

Figure 34: Image sequence for methane hydrate dissociation by depressurization with 5.0 wt% NaCl with a constant temperature of 3.9°C (Depressurization experiment 8). Average porosity of 0.52±0.02. Image P=53.4bar shows the initial hydrate distribution in the field of view, where hydrate is scattered in the gas. From images P=53.3bar to P=52.6bar, the hydrate saturation increases rather than dissociates. Redistribution of water, gas and hydrate, as indicated by the six yellow circles (1), causes the hydrate saturation to increase. In image P=49.1bar, precipitated salt crystals were observed to surround the hydrate, as indicated by the three yellow arrows (2), and this may explain the sudden drop in hydrate saturation. In image P=49.1bar + 26min, initial hydrate dissociation occurs. From images P=48.4bar to P=41.4bar, hydrate continues to dissociate, and hydrate is located in the center of the gas phase, indicated by the eight yellow arrows (3).

4.2.2 Saturation profiles of hydrate dissociation by depressurization

Following are four saturation profiles of water, gas and hydrate during hydrate dissociation by depressurization, illustrated in Figure 35. These are saturation profiles for the same hydrate dissociation by depressurization that were presented above in section 4.2.1.

The water, gas and hydrate saturations seemed to depend on their distribution in the micromodel. In all the cases, except in the case with 5.0 wt% NaCl, hydrate was initially being distributed uniformly in the porous media. The uniform hydrate phase seemed to cause a slight decrease in the hydrate saturation over several pressure steps, before the saturation plummeted during one pressure step. In the case with 5.0 wt% NaCl, the hydrate saturation increased from 0.59 to 0.67 over eight pressure steps, before it dropped to 0.24. After the hydrate saturation drop, some of the initial scattered hydrate remained and decreased steadily until all the hydrate was completely dissociated.

When the hydrate saturation decreased, the gas and water saturation increased. The gas saturation increased and the hydrate saturation decreased almost symmetrically. The water saturation increase was more random, dependent on redistribution of the fluids. After the initial hydrate dissociation with saline water with 2.0 wt% NaCl (42.8 bar) and with 5.0 wt% NaCl (49.1 bar), the gas and water saturation profiles became chaotic. This reflected the redistribution of the fluids.

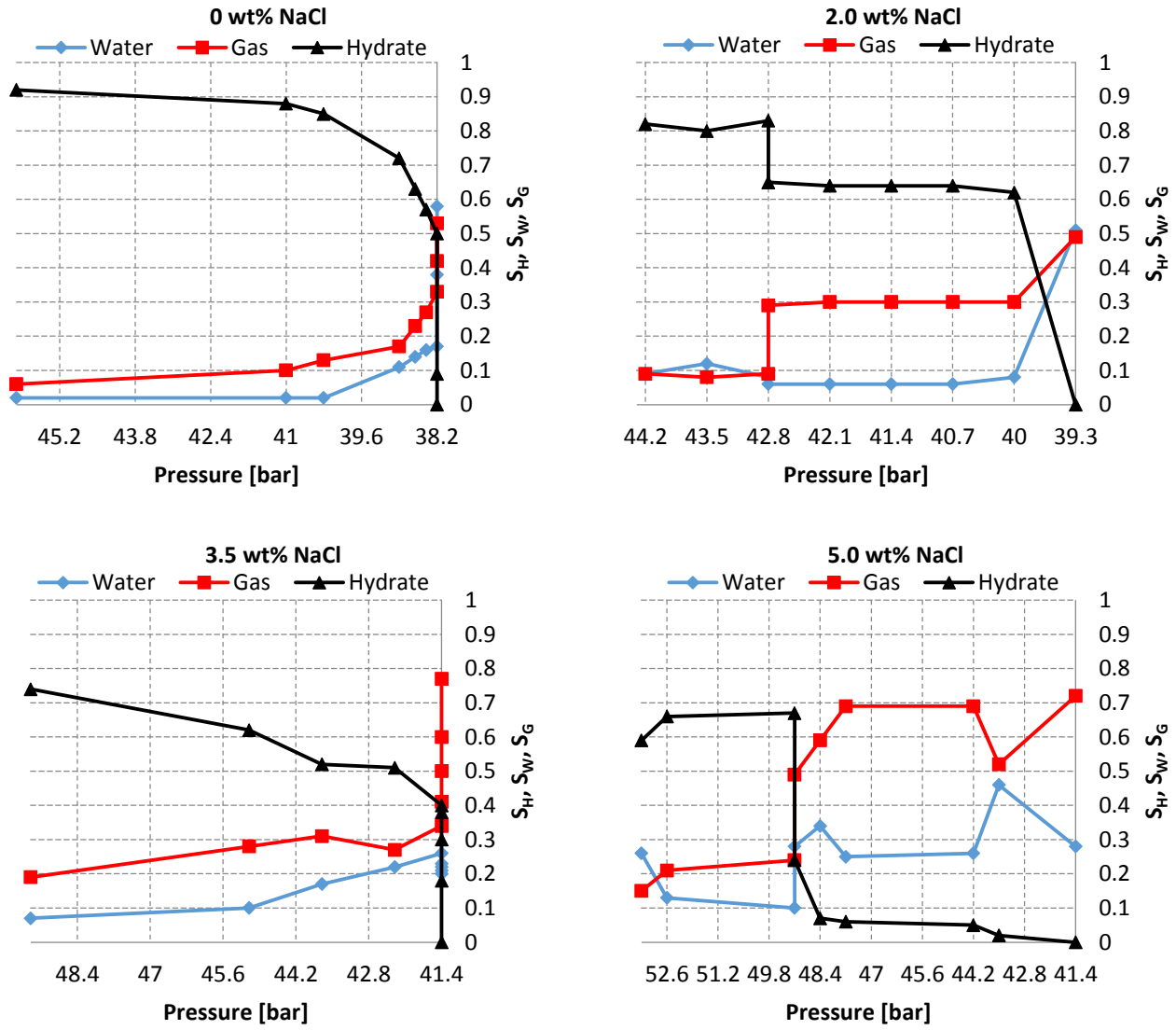

Figure 35: Estimated 2D saturation profiles for water salinities of 0, 2.0, 3.5 and 5.0 wt% NaCl when methane hydrate was being dissociated by depressurization. Hydrate, water and gas are represented by the colors black, blue and red, respectively.

4.2.3 Interpretation of the observations

In this section, key observations from the image sequences in section 4.2.1 will be interpreted. First, the hydrate dissociation patterns during depressurization will be discussed, then the observed differences between hydrate dissociation by depressurization with deionized water and saline water, and last, the effect of water and hydrate films on hydrate dissociation.

Dissociation by depressurization patterns

When hydrate was dissociated by pressure depletion, the dissociation was in general initiated in the center of the pore and continued out towards the water-gas interface at the pore walls. Due to lack of available free water, hydrate films in the center of the pores were most likely thinnest, and thereby easiest to dissociate. Further dissociation of the hydrate on the water-gas interface occurred when hydrate came in direct contact with free gas. Due to the endothermic nature of hydrate dissociation, already dissociated hydrate may prevent surrounding hydrate phases from dissociating. Consequently, heat has to be transferred to the hydrate from its surroundings, and out of the two fluids, water and gas, water has the greater heat transfer. Because of this, hydrate was expected to dissociate in contact with water rather than gas, but the experiments indicated the opposite. Even though hydrate was in direct contact with free water, dissociation did not occur before hydrate was in direct contact with free gas. This behavior is shown in Figure 36 for dissociation with deionized water and in Figure 37 for dissociation with saline water of 3.5 wt% NaCl. The dissociation pattern may be explained by the difference in mobility between gas and water. Dissociation liberates water and gas from the hydrate structure, and this may mobilize the water and gas. Since gas is more mobile than water, it seemed as if the mobilized gas transported heat better than the mobilized water. Gas may also expand (more than water) as a consequence of reduction in pressure. Similar dissociation patterns were observed for methane hydrate in glass micromodels (Katsuki et al., 2008) and silicon micromodels (Almenningen et al., 2016). The dissociation behavior was independent of the salinity of water.

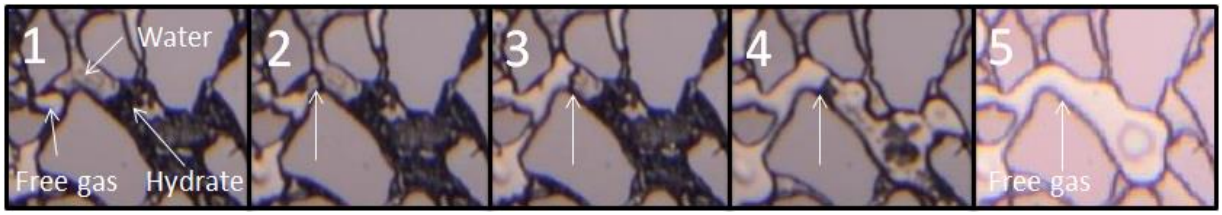

Figure 36: Magnification of image sequence in Figure 31. Image 1 shows hydrate and free gas separated by water at 38.6 bar. The arrows in images 2 to 5 (38.4 to 38.2 bar), illustrate how the free gas is being mobilized and displacing the water. Once the free gas connects with the hydrate, hydrate dissociates.

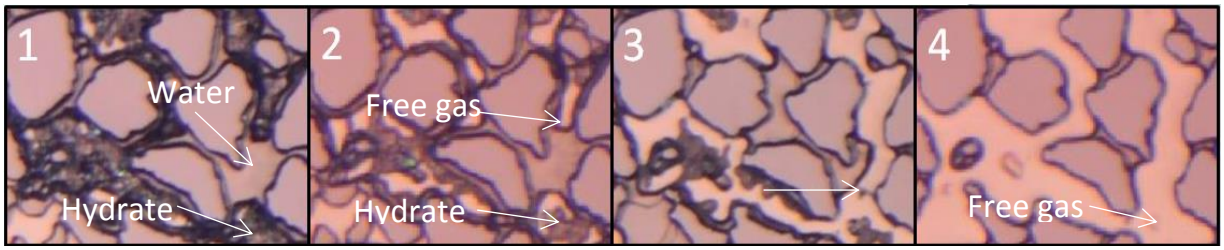

Figure 37: Magnification of image sequence in Figure 33. Image 1 shows the system at 49.3 bar prior to dissociation. In image 2, hydrate initially dissociates at 45.1 bar, and gas is mobilized. In images 3, at 41.6 bar (+30s) and 4, at 41.6 bar (+ 7h), the mobilized free gas connects with hydrate, and hydrate is dissociated.

Connectivity of hydrate within the porous media seemed to play an important role for the dissociation pattern. If the connectivity of the hydrate was high, the dissociation occurred homogeneously. If the connectivity of the hydrate was low, the dissociation occurred heterogeneously. In Figure 31, the water phase was restricting a hydrate phase to dissociate, and the heat had to be transferred through the gas and around the water phase before the hydrate could be dissociated. In contrast, the connectivity of the hydrate in Figure 32 was high, and the hydrate was dissociated homogeneously throughout the pores. The connectivity of the hydrate phase seemed to be more significant with increasing salinity. Following, differences between dissociation by depressurization with deionized water and dissociation by depressurization with saline water will be discussed.

Differences between hydrate dissociation by depressurization with deionized and saline water

The technique of reducing the pressure stepwise during all depressurization experiments showed that dissociation transpired over a range of pressure values. Stepwise pressure reduction with deionized water only took place over two to six pressure steps. In contrast, the number of required pressure steps increased with increased salinity. Dissociation with water salinities of 2.0, 3.5 and 5.0 wt% NaCl took place over two to six, three to nine and eleven pressure steps, respectively. The dissociation pressure steps, with respect to hydrate stability in bulk conditions, are illustrated in Figure 51 to 54 in Appendix 7.2. They show that initial hydrate dissociation occurred just above the theoretical dissociation pressure with deionized water and saline water of 2.0 wt% NaCl, and just below the theoretical dissociation pressure with saline water of 3.5% wt% NaCl. With saline water of 5.0 wt% NaCl, the initial hydrate dissociation took place approximately two pressure steps above the theoretical dissociation pressure. The same pressure reduction technique was used by Birkedal et al. (2014) and Almenningen et al. (2016), dissociating hydrate in Bentheim sandstone cores with saline water of 0.1 wt% NaCl and 3.5 wt% NaCl, respectively. Complete hydrate dissociation with saline water of 0.1 wt% NaCl was reported to occur over three pressure steps, and over ten to fifteen pressure steps with saline water of 3.5 wt% NaCl. Almenningen et al. (2016) also observed that initial hydrate dissociation occurred above the theoretical dissociation pressure for every experiment. Due to the visual uncertainty (identifying initial hydrate dissociation visually), the observed pressures reported in this thesis are uncertain. Hence, the number of pressure steps reported by Birkedal et al. (2014) and Almenningen et al. (2016), are probably more accurate.

The prolonged dissociation process may be explained by the salt content of the free water surrounding the hydrate. When hydrate forms, salt ions are excluded from the hydrate-forming water and may increase the salt concentration in the local water phase surrounding the hydrate. When hydrate dissociates, the process is reversed, which means that released water from hydrate crystals dilutes the local water and decreases the salinity. Consequently, the remaining hydrate may become stable towards the local low-saline water rather than towards the general high-saline water. The water should eventually contain the same amount of salt because water and salt are highly miscible.

Local high-saline water is believed to be the reason hydrate could grow during hydrate dissociation. In Figure 38, hydrate was dissociated with a water salinity of 3.5 wt% NaCl. Hydrate was observed to grow over an eight-minute period when the pressure was reduced from 42.3 to 41.6 bar. The pressure of 41.6 bar is approximately 4.4 bar below the theoretical dissociation pressure at 4.2°C with saline water of 3.5 wt% NaCl and approximately 2.0 bar above the theoretical dissociation pressure at 4.2°C with deionized water. Hydrate films seemed to grow from the water-gas interface displacing the surrounding water. As the hydrate films were growing, salt crystals were observed to

surround the hydrate films. After eight minutes most of the hydrate films had dissociated, which may be because the salinity in the surrounding water had become uniform.

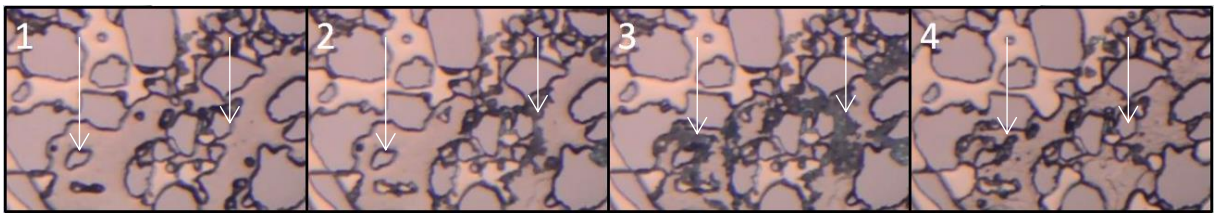

Figure 38: Magnification of image sequence in Figure 33, where hydrate growth took place over 8 minutes during dissociation at 41.6 bar and with a constant temperature of 4.2°C. Image 1 shows the water and hydrate distribution before hydrate started growing. In images 2 to 3, hydrate films were growing from the water-gas interface displacing the water, and salt crystals were observed surrounding the hydrate. In image 4, hydrate films have been dissociated.

During hydrate dissociation in Figure 34 (5.0 wt% NaCl), redistribution of hydrate and/or hydrate growth was observed. This has been magnified in Figure 39. The pressure was reduced from 52.6 to 49.1 bar (five pressure steps), and hydrate was observed to displace water. This observation indicates that hydrate was either redistributed, or that hydrate films grew from the water-gas interface, displacing the water. Rees et al. (2011) suggested that stimuli in hydrate-bearing deposits are very likely to cause hydrate to redistribute in porous networks, and thus cause changes in the physical properties of the sediments. Since the micromodel is a synthetic porous media, physical properties of the porous media will not change significantly. However, redistribution of hydrate may change the local thermodynamical stability conditions between water and hydrate, and between gas and hydrate. Hydrate displacing water, as shown in Figure 39, was most likely caused by redistribution, since a gas phase was observed beneath the hydrate once the hydrate had been dissociated. Hydrate seemed to grow in the surrounding gas because of the hydrate redistribution. Precipitated salt salt was observed surrounding the hydrate, similar to the observation in Figure 38. The salt crystals may also be why hydrate grew as a result of the redistribution.

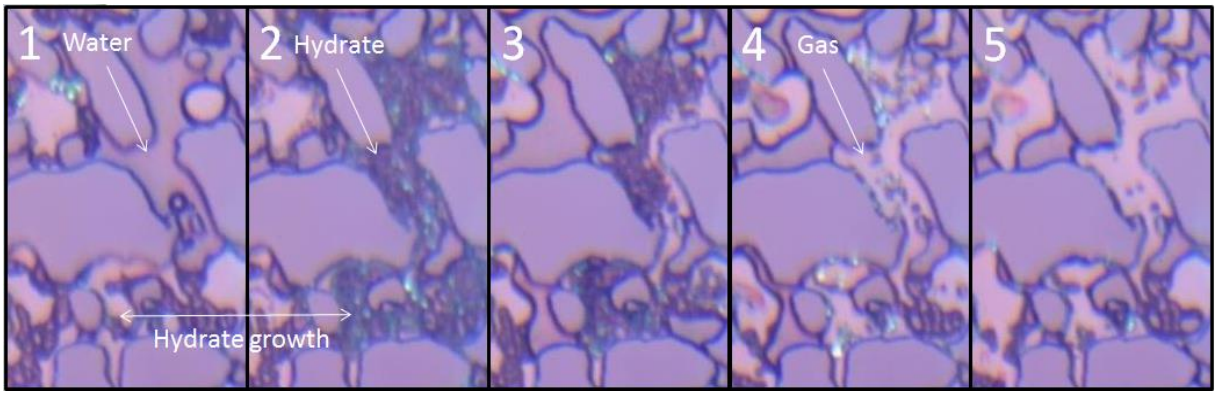

Figure 39: Magnification of image sequence in Figure 34, where redistribution of hydrate and/or hydrate growth took place during dissociation, at 49.1 bar and with a constant temperature of 3.9 °C. Image 1 shows the initial hydrate and water distribution at 52.6 bar. In image 2, at 49.1 bar, hydrate has displaced the water, and possible hydrate growth was observed as a consequence. Precipitated salt were observed surrounding the hydrate. Image 3 shows initial hydrate dissociation after 26 minutes at 49.1 bar. In images 4 and 5 further dissociation occured, and salt crystals were observed to disappear over time.

Hydrate films in the center of the pores due to water films

If water films were present on top of gas bubbles, hydrate films remained in the center of the pores when hydrate was being dissociated, as shown in Figure 40. The hydrate associated with water films were often the last hydrate to be dissociated. This behavior may be explained by the local water salinity in the water surrounding the hydrate film after initial dissociation, and is illustrated in Figure 41 . When hydrate is formed, salt is precipitated to the surrounding water. Subsequently, when hydrate is dissociated from the center of the pores (center of the gas) to the pore walls, the surrounding water is diluted by the liberated water. The hydrate film in the center of the gas is then dependent on the connectivity between itself and the water surrounding the gas, in order to dissociate. If the connectivity is high, the hydrate film will dissociate as the local water salinity is increasing. If the connectivity is low, probably caused by the gas between the hydrate film and the surrounding water, the hydrate film may develop local boundary conditions. Consequently, the hydrate film may be stable towards the dissociation pressure for deionized water. Hydrate films that form due to water films in the center of the pores, may be harder to initially dissociate because water films provide a high supply of water. Hydrate that initially dissociate in the gas, absorbs much of the heat. As a consequence, the remaining hydrate film in the center of the pore has to acquire heat from the surroundings in order to dissociate. The transport of heat may be delayed due to the surrounding gas and water.

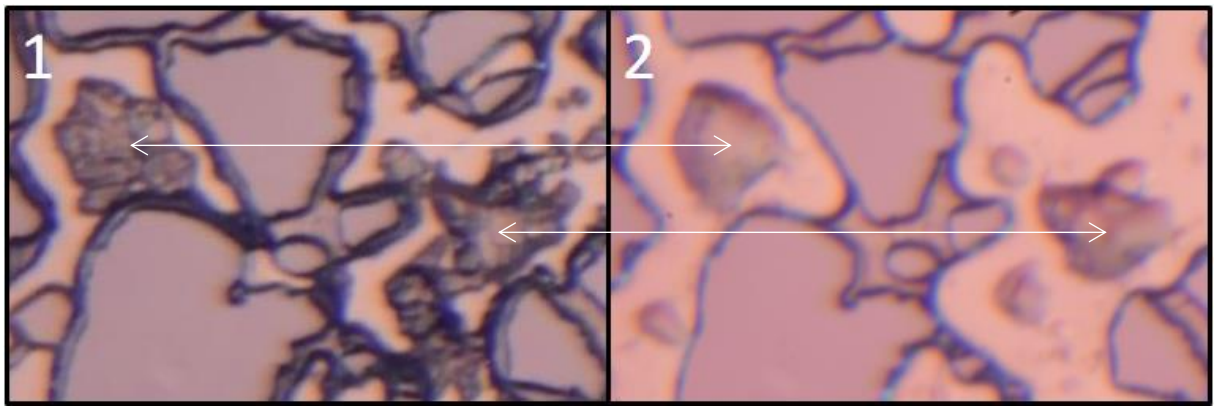

Figure 40: Magnification of image sequence in Figure 32, where hydrate films remained in the center of the pores. Image 1 shows two distinct hydrate films in the center of the gas phase at 40.0 bar and with a constant temperature of 4.0°C. In image 2, when the hydrate films were dissociating at 39,3 bar, water films remained on the gas phase.

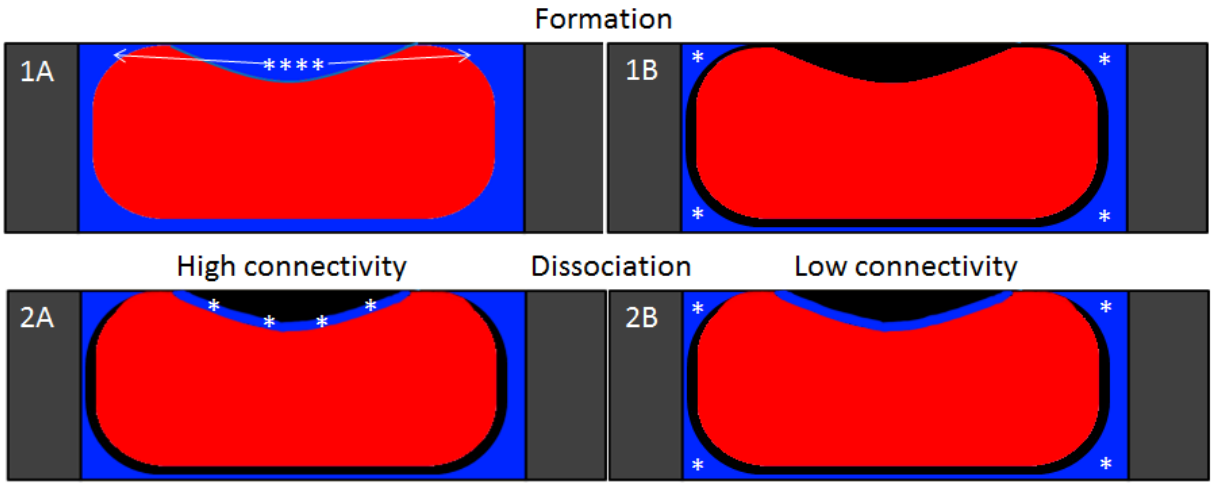

Figure 41: Cross-sectional illustration of hydrate films that grow in the center of the pores due to water films on gas bubbles. The white stars represent salt, gas is red, water is blue and hydrate is black. Image 1A shows the initial conditions where salt ions were located in the water films. Image 1B shows salt being liberated from the water films to the surrounding water. Image 2A shows a dissociation scenario where the connectivity between the surrounding water and water from the dissociating hydrate film is high. In this scenario, the hydrate film becomes continuously stable towards the salinity of the water from the surrounding water. Image 2B shows a dissociation scenario where the connectivity between the surrounding water and water from the dissociating hydrate film is low. In this scenario, the hydrate film remains stable towards the deionized water, which is being liberated from the dissociating hydrate film.

Hydrate films connected to water films seemed to persist with increased water salinity. With deionized water, hydrate films that were associated with water films, dissociated simultaneously with hydrate on the water-gas interface. In contrast, with saline water of 3.5 wt% NaCl and higher, hydrate films that were associated with water films, remained in the center of the pores, although hydrate was being dissociated on the water-gas interface. This observed behavior is illustrated in Figure 42. In depressurization experiment 6 (3.5 wt% NaCl), hydrate films remained in the center of the pores. Dissociation was not complete until the pressure was 41.6 bar at 4.2°C, which is 1.0 bar above the dissociation pressure for deionized water (39.6 bar at 4.2°C). Similar observations were made in depressurization experiment 8. If a porous network has isolated water pockets, equivalent to the water films in the micromodel, they might be the main reason why dissociation is delayed in high-saline pore-networks.

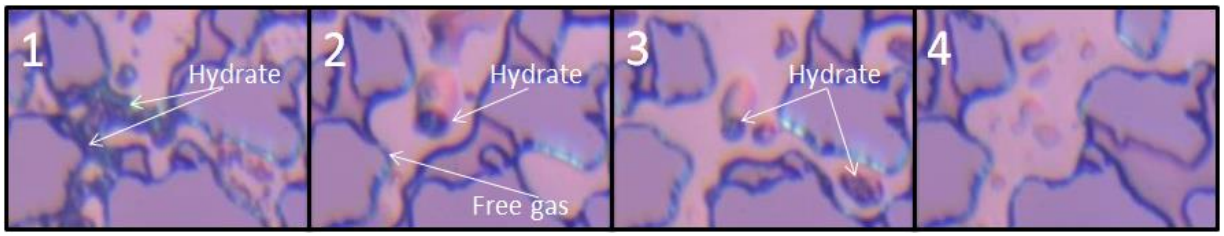

Figure 42: Magnification of image sequence in Figure 34, where hydrate was dissociated on the water-gas interface before dissociating in the center of the pore. Image 1 shows the hydrate distribution during dissociation at 49.1 bar. Image 2 shows hydrate films in the center of the pore at 48.4 bar. Here, hydrate on the water-gas interface has been dissociated. Image 3 shows hydrate films remaining in the center of the pore at 47.7 bar. In image 4, all the hydrate has been dissociated at 44.2 bar.

4.3 Hydrate dissociation by thermal stimulation

There were performed a total of five methane hydrate dissociations by thermal stimulation, whereof two with 0 wt% NaCl, one with 2.0 wt% NaCl, one with 3.5 wt% NaCl and one with 5.0 wt% NaCl. All the dissociation by thermal stimulation experiments are summarized in Table 7. A stepwise-temperature-increase technique was used when hydrate was being dissociated. The temperature was increased to approximately 2°C below the theoretical dissociation temperature, and then increased in increments of 0.1°C. It was observed that hydrate dissociation took place over several temperature steps. The initial dissociation temperature was identified when a significant change in hydrate occurred. Since the dissociation temperatures were estimated visually, the temperature values may be uncertain. The pressure was kept constant at 40.0 and 50.0 bar for deionized water and 60.0 bar for saline water. Four of the hydrate dissociations by thermal stimulation are presented as image sequences in section 4.3.1, and each one represents a different saline solution. The uncertainties of the values are discussed in appendix 7.1. The dissociation temperature-path from initial dissociation to complete dissociation is illustrated in Figures 51 to 54 in appendix 7.2.

Table 7: Methane hydrate dissociation by thermal stimulation with water salinities of 0 to 5.0 wt% NaCl. The column titled "Temperature steps" in the table refers to the number of temperature steps it took from initial dissociation to complete dissociation.

Exp.	**Salinity ±0.01 [wt%]**	**Initial temperature ±0.2 [°C]**	**Initial dissociation temperature ±0.2 [°C]**	**Complete dissociation temperature ±0.2 [°C]**	**Temperature steps (0.1°C)**	**Pressure ±1.4 [bar]**
1	0.0	4.1	4.2	4.4	2	40
2*	0.0	4.2	6.1	6.9	8	50
3*	2.0	4.0	7.0	8.3	13	60
4*	3.5	4.2	6.5	7.8	13	60
5*	5.0	3.9	5.6	7.9	23	60

**The dissociations being presented as image sequences.*

4.3.1 Image sequences for dissociation by thermal stimulation

Following are four image sequences for hydrate dissociation by thermal stimulation, presented in Figures 43 to 46 with increasing salinity. Each hydrate dissociation experiment conducted by thermal stimulation is presented in sequences with increasing temperature. The experiments were conducted to observe if there were any differences between the dissociation patterns of deionized water and saline water. Also, the experiments were conducted to compare dissociation by depressurization with dissociation by thermal stimulation. The observed dissociation trend was that hydrate melted from the water-gas interface at the pore walls to the pore center. A detailed interpretation of the saturation profiles follows in section 4.3.2, and the observations of the image sequences are discussed in 4.3.3.

Deionized water

Methane hydrate was dissociated with deionized water by increasing the temperature in increments of 0.1°C intervals under a constant pressure of 50 bar, as illustrated in Figure 43. The initial temperature was 5.0°C, and hydrate was completely dissociated when the temperature was 6.9°C. The initial hydrate saturation was low (0.34), and most of the pore space was saturated with water. From 5.0 to 6.1°C, minimal changes in the hydrate, gas and water were observed. Hydrate was observed to be in direct contact with free gas, indicated by the red circle (1) in Figure 43. Initial hydrate dissociation occurred between 6.1 and 6.2°C, and started from where the free gas was in direct contact with hydrate. At 6.3°C it seemed as if the dissociation was complete, but local hydrate was observed to remain in between four grains. Consequently, complete hydrate dissociation did not occur until the system had reached 6.9°C. The local hydrate indicates that connectivity is an important factor when hydrate is being dissociated.

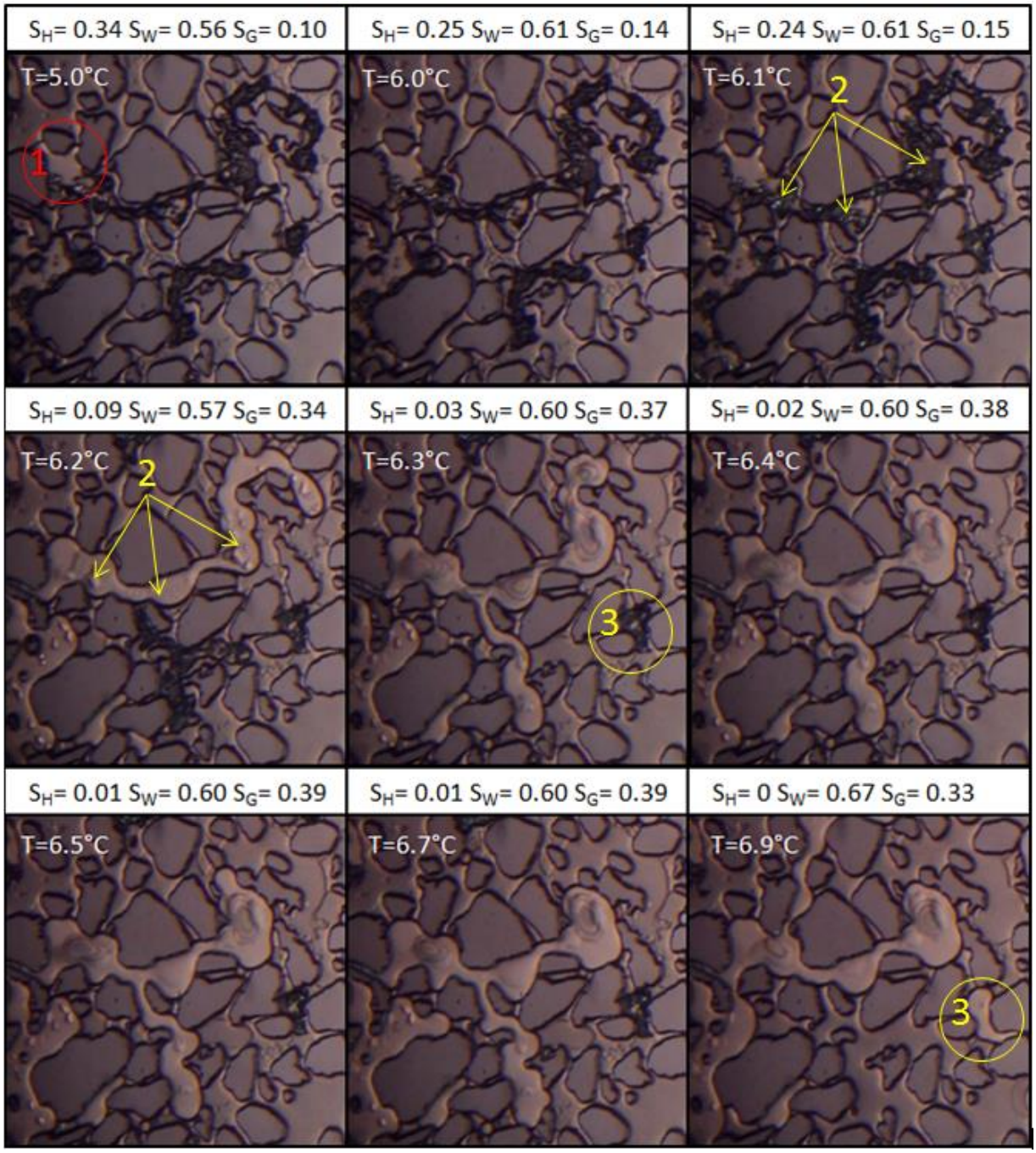

Figure 43: Image sequence for methane hydrate dissociation by thermal stimulation with deionized water under a constant pressure of 50.0 bar (Thermal stimulation experiment 2). Average porosity of 0.47±0.01. The sequence is dark because the images were taken from the outer part of the microscope video frame. Image T=5.0°C shows the initial hydrate distribution, and free gas in direct contact with hydrate is illustrated by the red circle (1). Images T=6.1°C and T=6.2°C show the initial hydrate dissociation, indicated by the six yellow arrows (2). Image T=6.3°C shows a local hydrate, illustrated by the first yellow circle (3). The local hydrate dissociated at 6.9°C, illustrated by the second yellow circle (3).

Water salinity of 2.0 wt% NaCl

Methane hydrate was dissociated with a water salinity of 2.0 wt% NaCl by increasing the temperature in increments of 0.1°C under a constant pressure of 60 bar, as illustrated in Figure 44. The initial temperature was 4.0°C, and hydrate was completely dissociated when the temperature was 8.3°C. The initial hydrate saturation was 0.60, and in the field of view images, hydrate was observed to be divided into two areas by gas. Consequently, the connectivity of hydrate might be low, and hydrate dissociation might be highly dependent on mobilized gas and water. The gas dividing the two hydrate phases resulted in a local dissociation pattern rather than a global one. From 4.0 to 6.9°C, minimal changes in the hydrate, gas and water distribution were observed. Initial hydrate dissociation occurred at 7°C, and from this point the hydrate saturation was reduced from 0.53, to 0.45 at 7.5°C. Hydrate was observed to dissociate from the water-gas interface at the pore walls to the center of the pores. A local hydrate saturation was observed to persist in the porous media after the initial hydrate dissociation until the hydrate had been completely dissociated, indicated by the yellow circles (3) in Figure 44. Even though the surrounding hydrate dissociated, the local hydrate remained, and this observation will be discussed further in section 4.3.3.

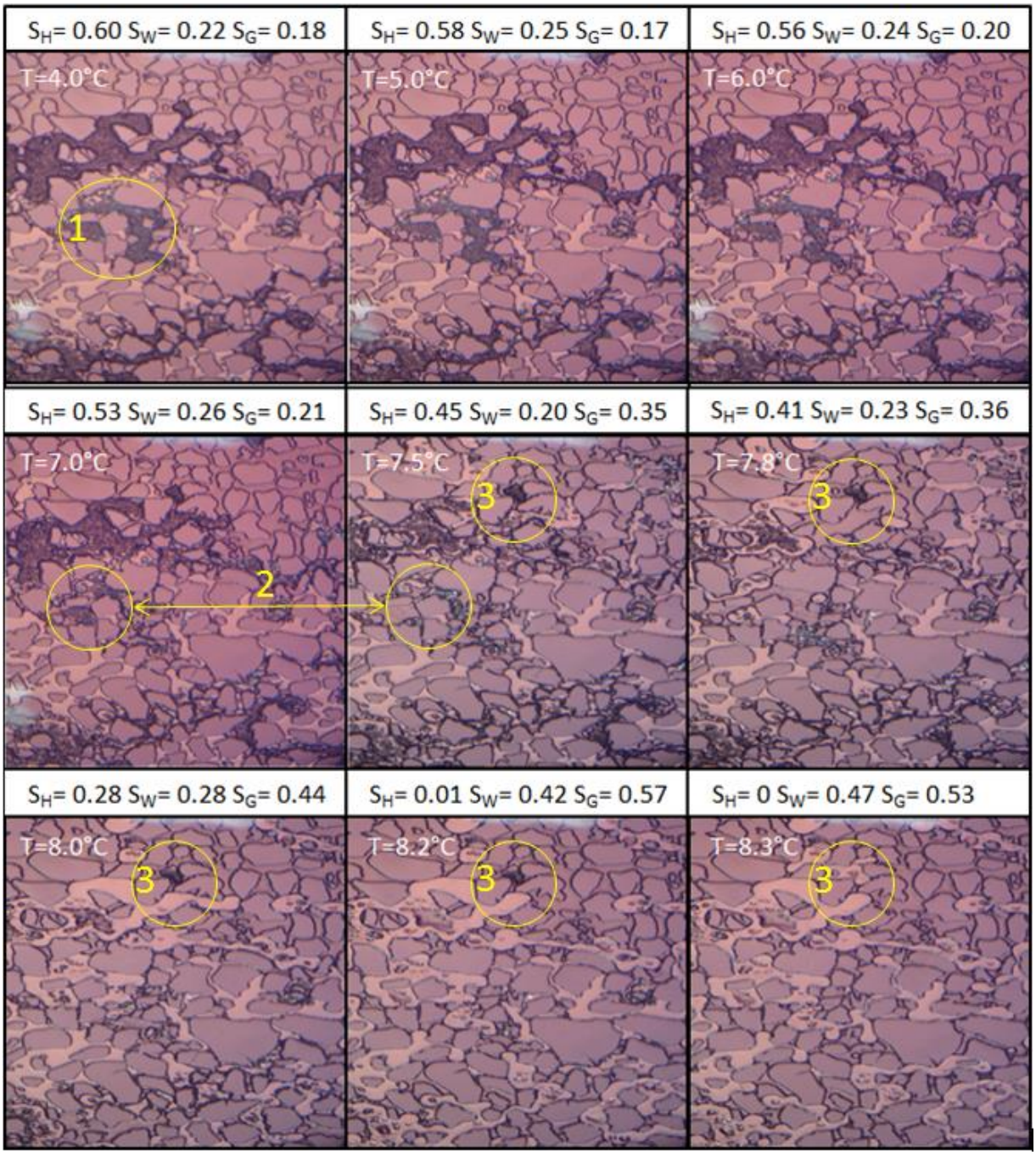

Figure 44: Image sequence for methane hydrate dissociation by thermal stimulation with a water salinity of 2.0 wt% NaCl under a constant pressure of 60 bar (Thermal stimulation experiment 3). Average porosity of 0.44±0.01. Image T=4.0°C shows the initial hydrate distribution. Some hydrate is observed to be surrounded by salt crystals, illustrated by the yellow circle (1). Images T=7.0°C and T=7.5°C show initial hydrate dissociation, illustrated by two yellow circles (2). In images T=7.5°C to T=8.3°C, hydrate generally continues to dissociate, but a local hydrate, indicated by five yellow circles (3), remains until complete dissociation.

Water salinity of 3.5 wt% NaCl

Methane hydrate was dissociated with a water salinity of 3.5 wt% NaCl by increasing the temperature in increments of 0.1 °C under a constant pressure of 60 bar, as illustrated in Figure 45. The initial temperature was 4.5°C, and hydrate was completely dissociated at 7.8°C. The initial hydrate saturation was 0.80, and the connectivity of hydrate was high. Precipitated salt crystals were observed to surround hydrates during the entire dissociation process, ending up at the water-gas interface. Initial hydrate dissociation took place at 6.5°C, at the same time as mobilized gas was observed to invade the field of view images. The invading gas may have originated from another dissociating hydrate, or expansion due to increased temperature. Hydrate was observed to dissociate from the water-gas interface at the pore walls to the center of the pores. During the hydrate dissociation, gas and water was observed to redistribute a lot in the pore space. The final water saturation was 0.34, and the final gas saturation was 0.66.

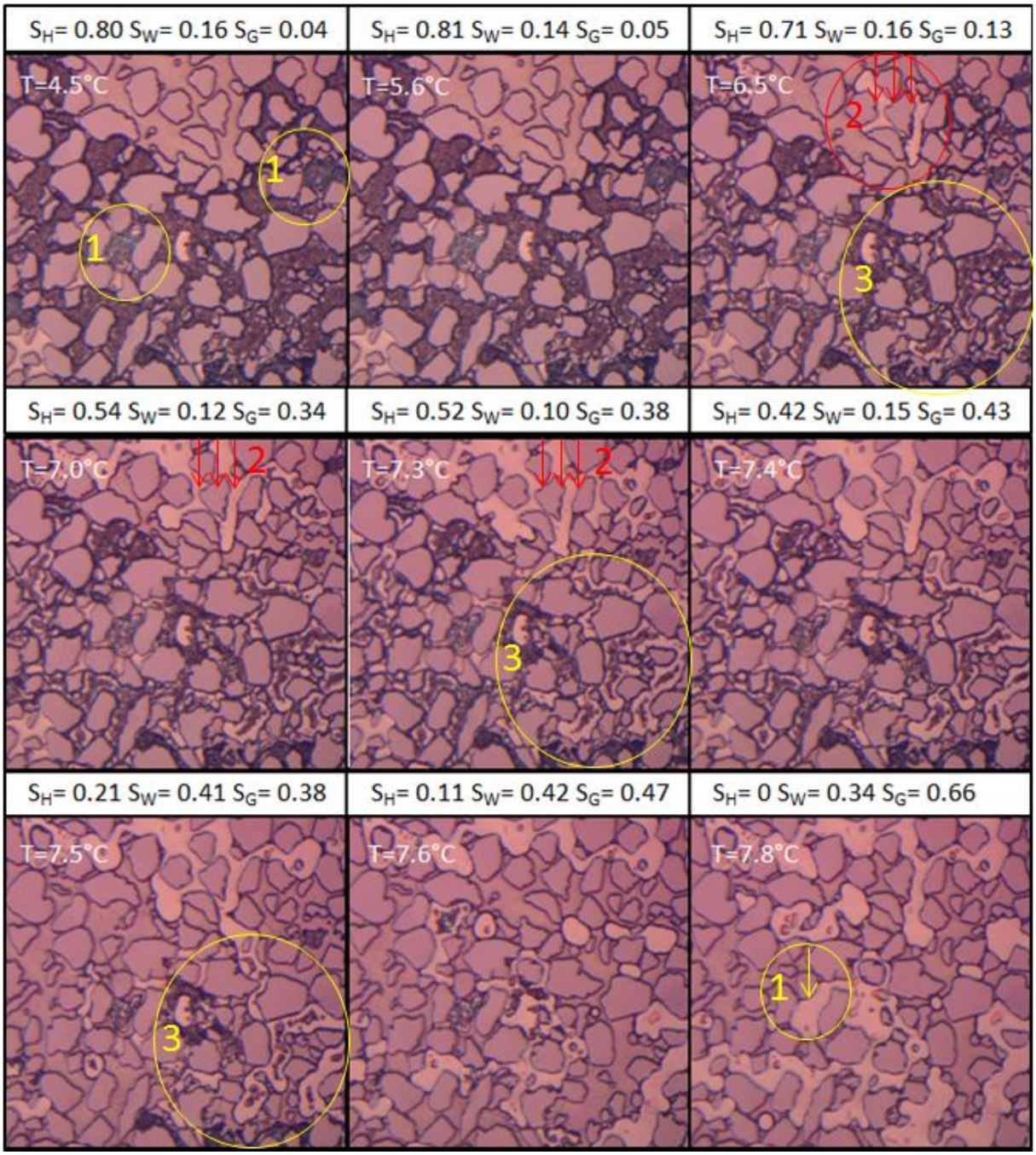

Figure 45: Image sequence for methane hydrate dissociation by thermal stimulation with a water salinity of 3.5 wt% NaCl under a constant pressure of 60 bar (Thermal stimulation experiment 4). Average porosity of 0.45±0.05. Image T=4.5°C shows the initial hydrate distribution, and salt ions were observed to surround two hydrate zones, illustrated by two yellow circles (1). The salt ions ended up on the water-gas interface. Images T=6.5°C to T=7.3°C show mobilized gas invading the field of view pore space, illustrated by the red arrows (2). Image T=6.5°C shows the initial hydrate dissociation, illustrated by a yellow circle (3). Following the yellow circles (3), the hydrate dissociation trend may be observed.

Water salinity of 5.0 wt% NaCl

Methane hydrate was dissociated with a water salinity of 5.0 wt% NaCl by increasing the temperature in increments of 0.1 °C under a constant pressure of 60 bar, as illustrated in Figure 46. The initial temperature was 3.9°C, and hydrate was completely dissociated when the temperature was 7.9°C. Hydrate was initially scattered in the pore space, and the initial hydrate saturation was 0.48. Initial hydrate dissociation occurred at 5.6°C, and hydrate was observed to dissociate from the water-gas interface at the pore walls to the center of the pores. Further dissociation was slow, and a significant change was not observed until the temperature was 6.2°C. From 6.2 to 6.9°C, the hydrate reduced significantly, and may have caused redistribution of gas and water. Hydrate was observed to cement the pore walls, indicated by the yellow arrows (3) in Figure 46. The hydrate cementation will be discussed further in section 4.3.3. Hydrate persisted in the center of the pores, and this was the last remaining hydrate before complete hydrate dissociation occurred at 7.9°C.

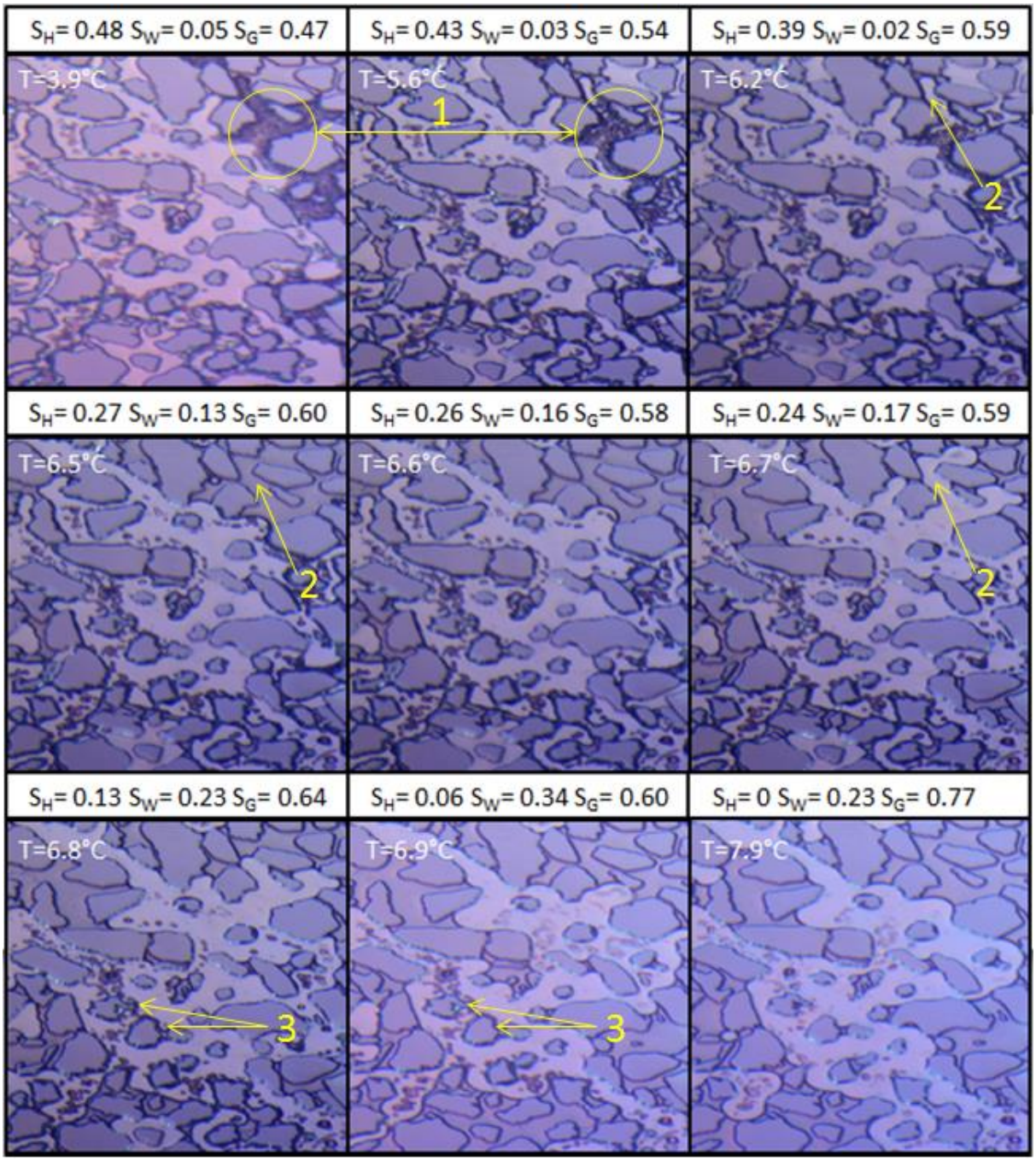

Figure 46: Image sequence for methane hydrate dissociation by thermal stimulation with a water salinity of 5.0 wt% NaCl under a constant pressure of 60 bar (Thermal stimulation experiment 5). Average porosity of 0.53±0.01. Image T=3.9°C shows the initial hydrate distribution. Image T=5.6°C shows the initial hydrate dissociation, illustrated by the two yellow circles (1). In images T=6.2°C to T=6.7°C, gas was observed to mobilize and redistribute the hydrate and water, illustrated by yellow arrows (2). In images T=6.8°C and T=6.9°C, hydrate is cementing the grains, illustrated by yellow arrows (3).

4.3.2 Saturation profiles of hydrate dissociation by thermal stimulation

Following are four saturation profiles of water, gas and hydrate during hydrate dissociation by thermal stimulation, illustrated in Figure 47. These are saturation profiles for the same hydrate dissociations by thermal stimulation that were presented above in section 4.3.1.

The saturation profiles for hydrate and gas were mostly a reflection of each other. In all four cases, the gas saturation increased when the hydrate saturation decreased. Generally, the water saturation increased slightly when there were small changes in the hydrate saturation, but when initial hydrate dissociation occurred, there was a sudden increase in the water saturation. However, for dissociation with deionized water, there was no distinct change in the water saturation. In this case the initial water saturation was already high, compared to the dissociation with saline water. When hydrate had been completely dissociated, the water and gas saturations varied between 0.23-0.67 and 0.33-0.77, respectively. This randomness of the end saturations was probably due to redistribution after initial dissociation and the value of the initial hydrate saturation. If the initial hydrate saturation was high, the final gas saturation was mostly high and the final water saturation mostly low. If the initial hydrate saturation was low, the final gas saturation was often low and the final water saturation often high.

Saturation profiles of hydrate dissociation by thermal stimulation were less chaotic compared to saturation profiles of hydrate dissociation by depressurization, in section 4.2.2. The behavior may indicate that dissociation by thermal stimulation is more uniform than dissociation by depressurization. Previous dissociation experiments performed by Almenningen et al. (2016) Flatlandsmo (2015) reported similar observations.

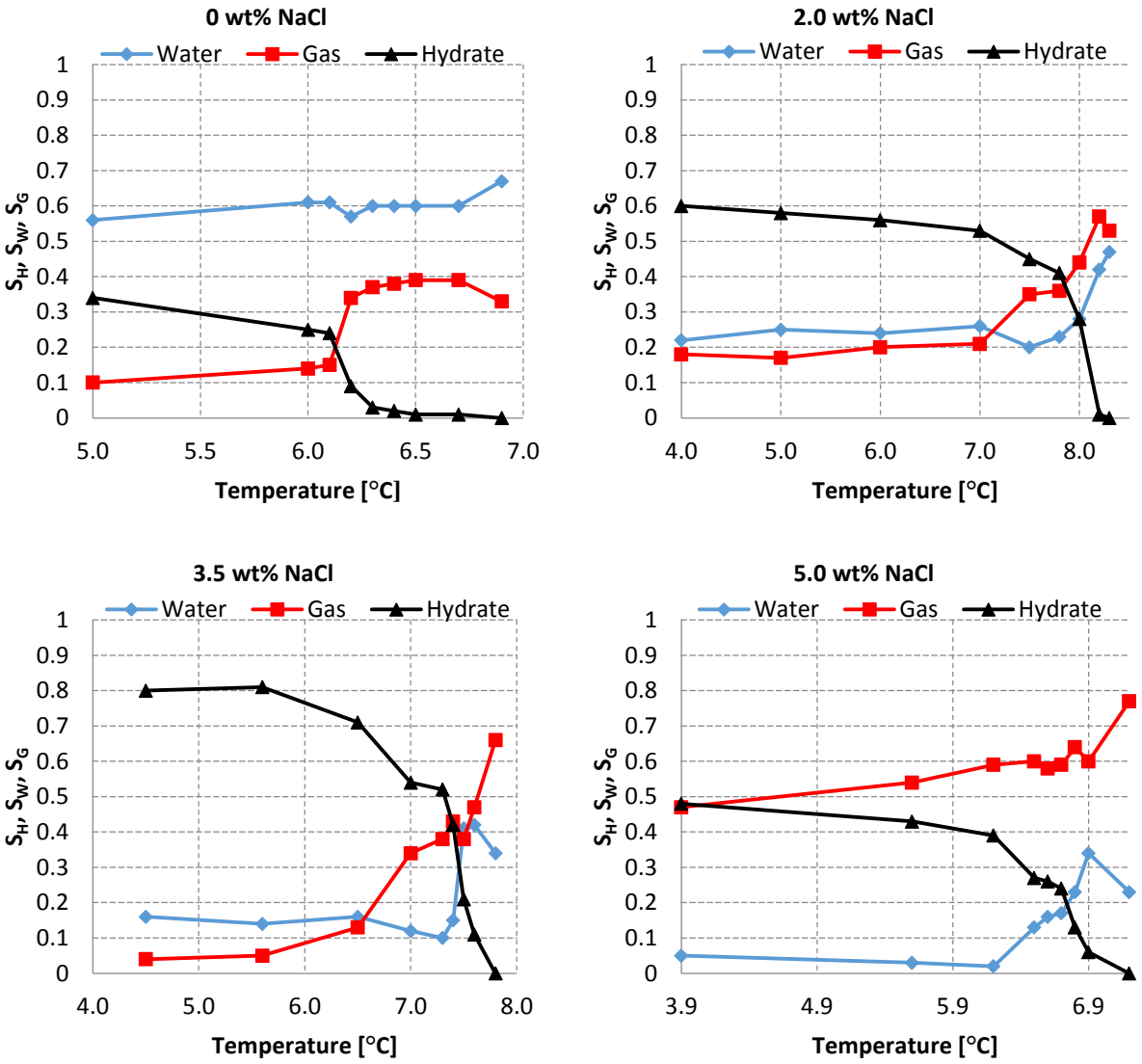

Figure 47: Estimated 2D saturation profiles for water salinities of 0, 2.0, 3.5 and 5.0 wt% NaCl during methane hydrate dissociation by thermal stimulation. Hydrate, water and gas are represented by the colors black, blue and red, respectively.

4.3.3 Interpretation of the observations

In this section, key observations from the image sequences in section 4.3.1 will be interpreted. First, the hydrate dissociation patterns during thermal stimulation will be discussed, then the observed differences between hydrate dissociation by thermal stimulation with deionized and saline water, and last, local isolated hydrate saturations.

Dissociation by thermal stimulation patterns

When hydrate was dissociated by thermal stimulation, hydrate generally dissociated from the water-gas interface at the pore walls to the center of the pores, as illustrated in Figure 48. The thermal stimulation dissociation pattern was the opposite of the depressurization dissociation pattern, and is believed to be a consequence of the thermal conductivity of the silicon wafer. Because the thermal conductivity is high in the silicon wafer, heat may have been transported evenly through the wafer. Consequently, the hydrate may have been melted from underneath and along the grains, even though the hydrate films are believed to be thickest on the water-gas interface. In addition, water has higher heat conductivity than gas, so hydrate phases surrounded by water may experience a better heat transport than hydrate phases surrounded by gas.

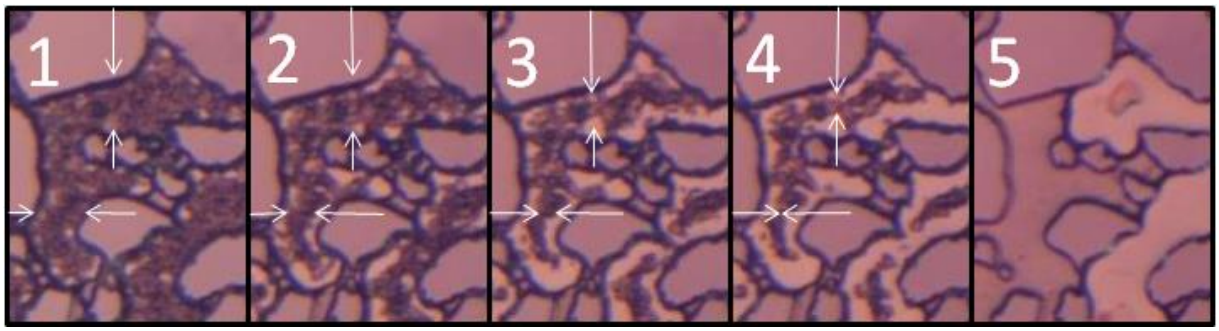

Figure 48: Magnification of image sequence in Figure 45, where hydrate dissociates from the pore walls to the center of the pores, indicated by the white arrows. Image 1 shows hydrate before hydrate was dissociated at 5.6°C. Image 2 shows initial hydrate dissociation at 6.5°C. Images 3 and 4 show how the hydrate dissociated towards the center of the pores from 7.2 to 7.4°C. Image 5 shows the pore space after complete hydrate dissociation at 7.8°C.

Differences between hydrate dissociation by thermal stimulation with deionized and saline water

The technique of increasing the temperature stepwise during all thermal stimulation experiments showed that dissociation transpired over several temperature steps. The stepwise temperature technique indicated that water solutions with higher salinity content required more temperature steps before hydrate was completely dissociated. With deionized water, dissociation took place over two to eight steps, and with water salinities of 2.0, 3.5 and 5.0 wt% NaCl, dissociation took place over 13, 13, and 23 steps, respectively. The dissociation temperature steps, with respect to theoretical hydrate stabiliy in bulk conditions, are illustrated in Figure 51 to 54 in Appendix 7.2. Initial hydrate dissociation occurred above the theretical dissociation temperature for all four water solutions, and hydrate was completely dissocatiated when the system was below the theoretical dissocation temperature. The prolonged dissociation behavior for thermal stimulation due to pore water freshening is believed to be similar to that explained for depressurization. Hydrate films connected to water films seemed to be the main reason why the pressure reduction with saline water ranged over several pressure steps. However, for thermal stimulation, local hydrate saturations seemed to play an important role.

Local hydrate saturations

Local hydrate saturations prolonged the dissociation process for every water solution. Even though it is believed that the heat transport is homogeneous throughout the model, local hydratesaturations were observed to remain in the pores after most of the surrounding hydrate had dissociated. The dissociation pattern seemed to depend on the size and distribution of the hydrate, and the connectivity between hydrates. In Figure 49, there are two examples where local hydrate saturations persisted, while the surrounding hydrate was dissociating. In example A, the neighbor hydrate dissociated at 7.5°C, while the local hydrate remained, and dissociated later at 8.3°C. In example B, the local hydrate initially dissociated simultaneously with the neighbor hydrate at 6.5°C, but persisted until 7.6°C. In both cases, the local hydrate was located in between several grains in the periphery of a large hydrate phase, which may lead to low connectivity to the neighbor hydrate. The larger hydrate phases may have absorbed much of the heat during the temperature increase.

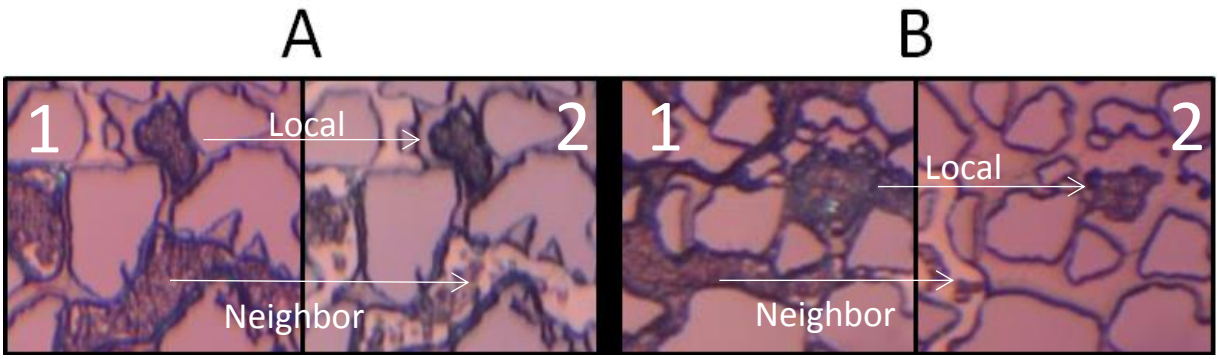

Figure 49: Magnification of images from Figure 44 and Figure 45. A: Water salinity of 2.0%. The neighbor hydrate dissociates between images 1-2 (7.0 to 7.5°C), while the local hydrate remains. B: Water salinity of 3.5%. Both the local and the neighbor hydrate initially dissociate between images 1-2 (5.6 to 7.5°C), but the local hydrate stabilizes and remains until 7.6°C.

In Figure 46 (thermal stimulation experiment 5), hydrate was observed to cement the walls of two grains. The observation of cementation was not expected, as hydrate generally dissociated from the pore walls to the center of the pores, but cementation may be caused by cracked hydrate films during hydrate formation (Jin et al., 2012). Jin et al. (2012) observed that hydrate initially grew as films, but cracked over time causing hydrate to cement the grains. The cemented hydrate films were the last remaining before all hydrate was completely dissociated. Seeing as the grains were surrounded by gas, the cementation may also be a result of low connectivity between the local hydrate and free water. There were several occasions during all the dissociation experiments where gas totally surrounded grains, with no observation of hydrate cementation. In thermal stimulation experiment 5, since the hydrate generally was scattered in the porous network in the, the dissociation characteristics seemed to be more local than global. The cemented hydrate phases from this experiment are presented in Figure 50. There were some small hydrate phases in the gas which may have restricted the heat transfer to the cemented hydrate at 6.9°C. The hydrate dissociated completely ten temperature steps later (1.0°C).

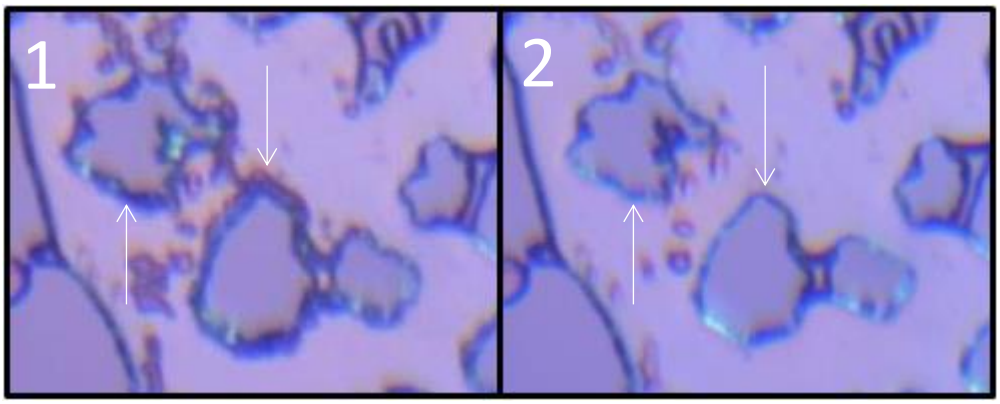

Figure 50: Magnification of cemented hydrate films near the grains in Figure 46. Image 1 shows the cemented hydrate, indicated by the arrows. Low connectivity between the free water and hydrate films near the grains may have caused the cemented hydrate. Temperature of 6.9°C. In image 2, the cemented hydrate was dissociated at 7.9°C.

5 Conclusion

Methane hydrate formation

- Sixteen hydrate formations, with salinities ranging from 0 – 5.0 wt% NaCl, were successfully conducted in a synthetic micromodel, where ten were primary hydrate formations and six were secondary formations. Primary hydrate formation was faster and more homogeneous than secondary hydrate formation. This observation was independent of water content, and is explained by higher driving forces for primary formation compared to secondary formation.
- Initial hydrate growth occurred on the water-gas interface along the pore walls and continued to grow in the gas phase towards the pore center. The presence of water films in gas sometimes resulted in initial hydrate growth within the gas phase.
- Hydrate formation with saline water of 3.5 and 5.0 wt% NaCl required greater driving forces to commence than hydrate formation with deionized water and water with a salinity of 2.0 wt% NaCl. The hydrate formation rate decreased with increasing salinity.
- Hydrate crystals were observed to grow from the water-gas interface into the free water phase. Initially the hydrate crystals were faceted before they gained a dendritic characteristic.

Methane hydrate dissociation

- Eight hydrate dissociations by depressurization and five hydrate dissociations by thermal stimulation were successfully conducted in a synthetic micromodel, with salinities ranging from 0 – 5.0 wt% NaCl.
- Hydrate was observed to generally dissociate from the center of the pores towards the water-gas interface at the pore walls during depressurization. Further hydrate dissociation was favored when the hydrate was in direct contact with free gas rather than when hydrate was surrounded by water. The high mobility of gas is believed to contribute to a greater heat transport in gas than water.
- During thermal stimulation, hydrate was observed to generally dissociate from the water-gas interface at the pore walls towards the center of the pores. The high thermal conductivity of the silicon wafer is believed to transport heat homogeneously through the micromodel, and melt the hydrate from beneath.
- Hydrate was dissociated over a range of pressure or temperature steps, and the number of required steps from initial hydrate dissociation to complete hydrate dissociation, increased with increased salinity. This is believed to be due to a continuous decrease in salinity in the local water phases when pure water was being liberated from the dissociating hydrate structure. As a consequence of the pore water freshening, hydrate became more stable towards the low-saline water, and thus hydrate required higher driving forces to dissociate. Local hydrate saturations within the gas, as well as isolated hydrate saturations in the pore space, are believed to be the main reason why dissociation was prolonged with saline water.
- Local hydrate was observed to grow during dissociation, which might be caused by local-high saline phases and/or redistribution of gas and water.
- Connectivity between the hydrate was observed to play an important role for both dissociation methods. With high connectivity, hydrate dissociated more uniformly, and with low connectivity, hydrate dissociated more locally.
- Saturation profiles for water, gas and hydrate during formation and dissociation showed that gas and hydrate saturation behavior were highly dependent on each other, while the water saturation decreased and increased more randomly. Also, the saturation profiles indicated that dissociation by thermal stimulation is more uniform than dissociation by depressurization.

6 Future work

Observing experiments visually on pore-level can give valuable information about gas hydrates, and here are some suggestions for future experiments:

- CH_4 hydrate formation with saline water at higher driving forces, and aging of the hydrate.
- CO_2 hydrate formation with saline water compared with CH_4 hydrate formation with saline water.
- CO_2-CH_4 exchange experiments, if it is possible. It would be interesting to see if there were any changes in the methane hydrate phase when CO_2 is being introduced.
- CH_4 hydrate formation with other thermodynamic inhibitors, such as alcohols and glycols, or polymers.
- CH_4 hydrate formation in a neutral-wet and oil-wet micromodel, to observe to what degree the wetting would affect the formation pattern.
- Numerical pore scale modelling of the hydrate growth rate.

7 Appendix

7.1 Uncertainties

This section will give an overview of the uncertainties in the experiments performed in this thesis and their possible influence on the results. In Table 8, the known uncertainties for the equipment are presented.

Table 8: Equipment uncertainties specified by manufactures

Equipment	**Parameter**	**Uncertainty**	**Unit**
Quizix Q5000 pump	Pressure	0.2	%
HH506RA Thermometer	Temperature	0.1	°C
GF-3000 Digital Balance	Weight	0.02	g
Slide caliper	Length	0.01	cm

The uncertainties of the pore volume of the micromodel and the salinity were calculated by the following equation:

$$\sigma_R = \sqrt{\left(\frac{\partial R}{\partial x_1}\sigma x_1\right)^2 + \cdots + \left(\frac{\partial R}{\partial x_n}\sigma x_n\right)^2} \tag{7.1}$$

where R is the composite value and σx_i is the uncertainty for each measurement. The salinity was estimated to have an uncertainty of ±0.01 wt% NaCl and the pore volume was estimated to have an uncertainty of ±0.0006ml.

The stepwise pressure and temperature-techniques used in this work, are highly sensitive to pressure and temperature fluctuations in the system. The two pressure pumps have a 0.2% uncertainty of the full scale pressure limit (689 bar), which yields an uncertainty of ±1.4 bar for every pressure value. During depressurization, fluctuations in the pressures were observed, especially between each pressure step. When the system was induced thermally, the pressure was kept constant and became more stable. Temperature variations in the micromodel will have a great impact on the dissociation pressure. The thermometer generally has an uncertainty of ±0.1°C, but the temperature was observed to differ depending on whether it was day or night, and the temperature was estimated to have an uncertainty of ±0.2°C.

7.2 Experimental dissociation pressure and temperature steps

The experimental dissociation pressure and temperature steps in relation to the theoretical stability curve for methane hydrate, calculated by CSMGem, are presented in Figure 51 to 54. The pressure and temperature steps are indicated by red and blue, respectively. The straight line shows the path from initial hydrate dissociation to complete hydrate dissociation.

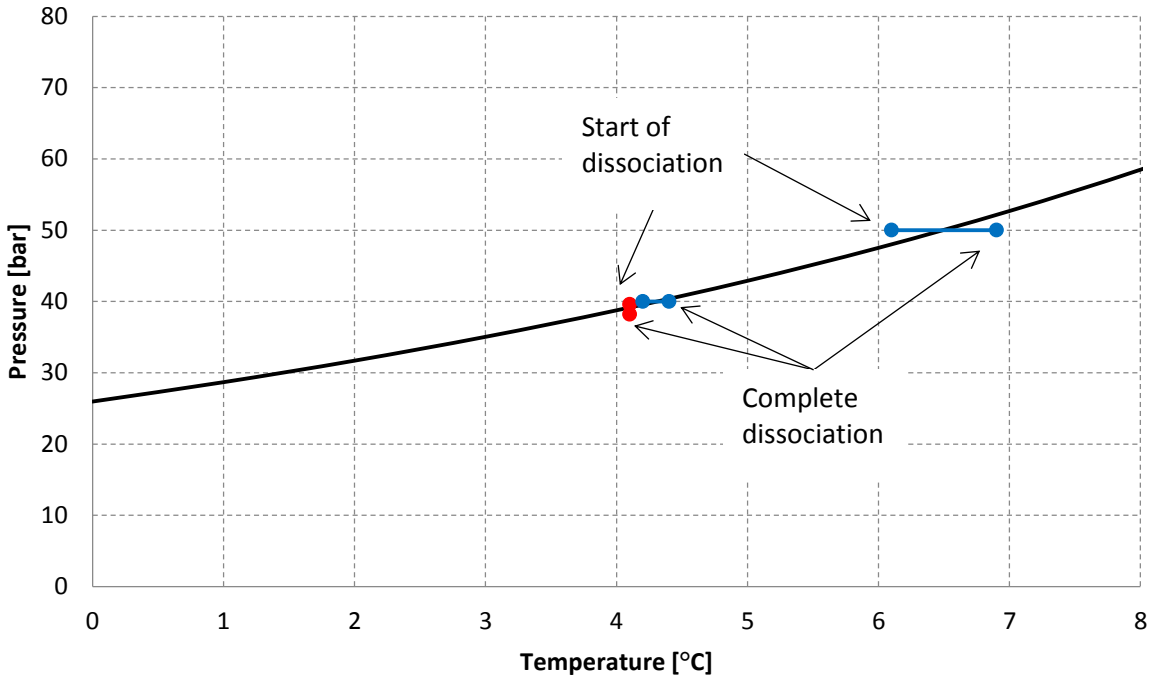

Figure 51: Dissociation pressure steps (red) and temperature steps (blue) for deionized water. The theoretical stability curve is calculated by CSMGem (Colorado School of Mines, 2015).

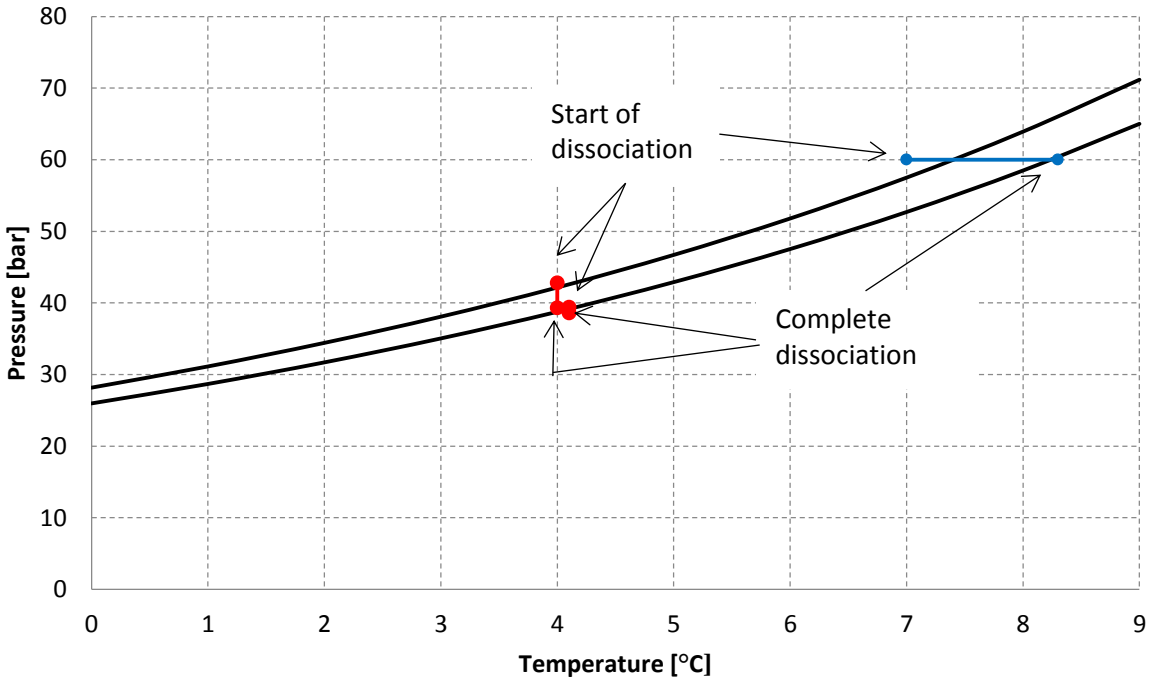

Figure 52: Dissociation pressure steps (red) and temperature steps (blue) for 2.0 wt% NaCl. The theoretical stability curves are calculated by CSMGem (Colorado School of Mines, 2015). The lower curve represents deionized water, and the upper curve represents water with 2.0 wt% NaCl.

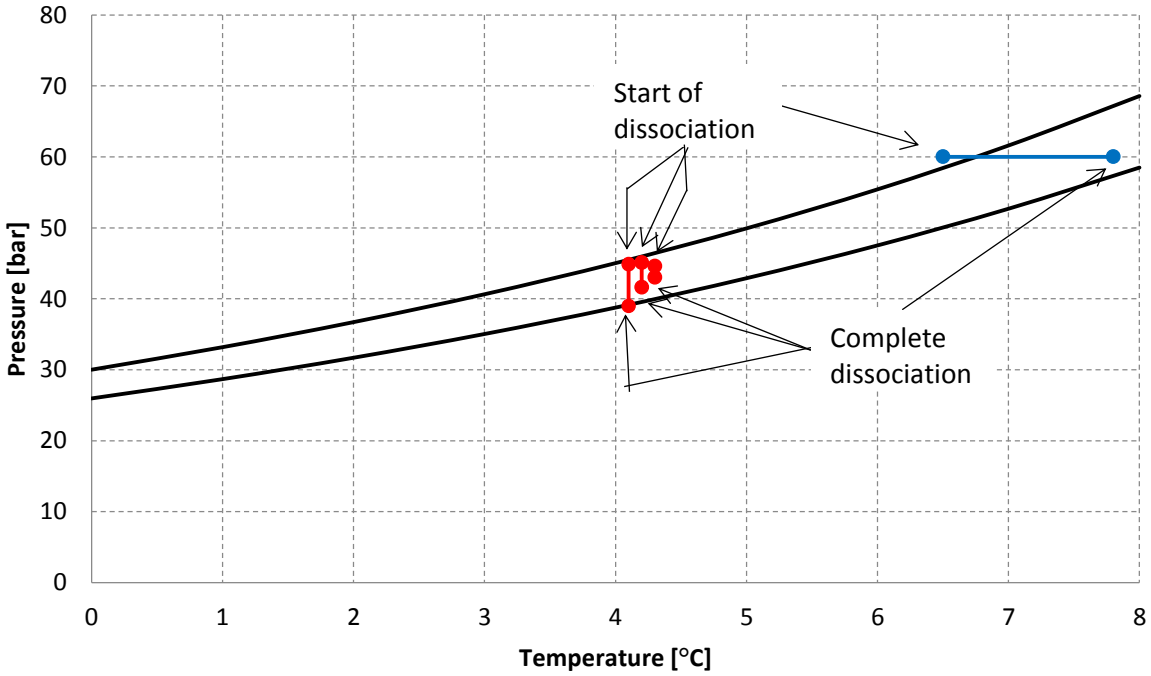

Figure 53: Dissociation pressure steps (red) and temperature steps (blue) for 3.5 wt% NaCl. The theoretical stability curves are calculated by CSMGem (Colorado School of Mines, 2015). The lower curve represents deionized water, and the upper curve represents water with 3.5 wt% NaCl.

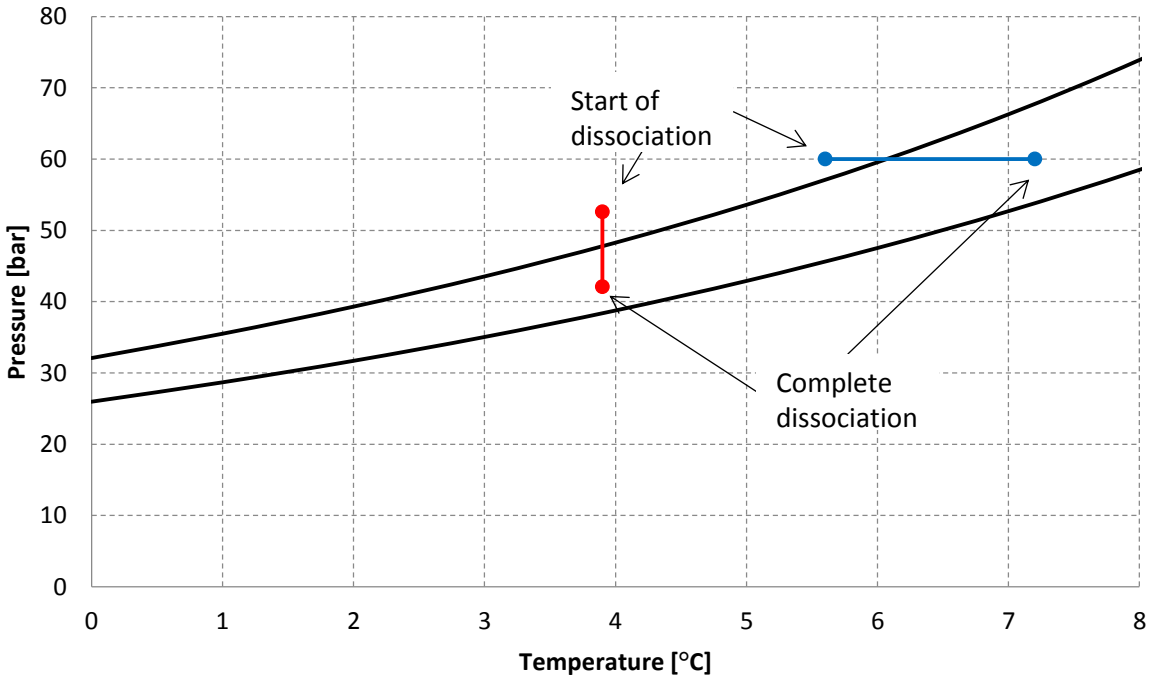

Figure 54: Dissociation pressure steps (red) and temperature steps (blue) for 5.0 wt% NaCl. The theoretical stability curves are calculated by CSMGem (Colorado School of Mines, 2015). The lower curve represents deionized water, and the upper curve represents water with 5.0 wt% NaCl.

7.3 Nomenclature

S_w	Water saturation	-
S_g	Gas saturation	-
S_h	Hydrate saturation	-
ϕ	Porosity	-
V_p	Pore volume	[ml]
r	Radius	[m]
H	Height	[m]
W	Width	[m]
L	Length	[m]
ΔG	Gibbs free energy	[J]
ρ_N^H	Molecular density	[mole/m^3]
γ	Interfacial free energy	[J/m^2]
n	Refraction index	-
ε	Pixel	-

7.4 Abbreviations

Wt%	Weight percent
Å	Ångstrøm
CSMGem	Colorado School of Mines Gibbs free energy minimization
GHSZ	Gas hydrate stability zone
GHOZ	Gas hydrate occurrence zone
HON	Homogeneous nucleation
HEN	Heterogeneous nucleation

8 Bibliography

ALLRED, A. & ROCHOW, E. G. 1958. A Scale of Electronegativity Based on Electrostatic Force. *Journal of Inorganic and Nuclear Chemistry,* 5**,** 264-268.

ALMENNINGEN, S., FLATLANDSMO, J., FERNØ, M. A. & ERSLAND, G. 2016. Multiscale Laboratory Verification of Depressurization for Production of Sedimentary Methane Hydrates. *SPE,* 22.

AZOM. 2009. *Borosilicate Glass - Properties of Borosilicate Glass (Pyrex/Duran) by Goodfellow Ceramic & Glass Division* [Online]. Available: http://www.azom.com/article.aspx?ArticleID=4765 [Accessed 2 May 2017].

BIRKEDAL, K. A., FREEMAN, C. M., MORIDIS, G. J. & GRAUE, A. 2014. Numerical Predictions of Experimentally Observed Methane Hydrate Dissociation and Reformation in Sandstone. *Energy & Fuels,* 28**,** 5573-5586.

BUCHGRABER, M., AL-DOSSARY, M., ROSS, C. & KOVSCEK, A. R. 2012a. Creation of a dual-porosity micromodel for pore-level visualization of multiphase flow. *Journal of Petroleum Science and Engineering,* 86-87**,** 27-38.

BUCHGRABER, M., CASTANIER, L. M. & KOVSCEK, A. R. 2012b. Microvisual Investigation of Foam Flow in Ideal Fractures: Role of Fracture Aperture and Surface Roughness. *SPE Annual Technical Conference and Exhibition.* San Antonio, Texas, 8-10 October: SPE.

BYLOV, M. & RASMUSSEN, P. 1997. Experimental determination of refractive index of gas hydrates. *Chemical Engineering Science,* 52**,** 3295-3301.

CLENNELL, M. B., HOVLAND, M., BOOTH, J. S., HENRY, P. & WINTERS, W. J. 1999. Formation of natural gas hydrates in marine sediments: 1. Conceptual model of gas hydrate growth conditioned by host sediment properties. *Journal of Geophysical Research,* 104**,** 22985-23003.

COLLETT, T. S. 2002. Energy Resource Potential of Natural Gas Hydrates. *AAPG Bulletin,* 86**,** 1971-1992.

COLORADO SCHOOL OF MINES. 2015. *Center for Hydrate Research Software* [Online]. Available: http://hydrates.mines.edu/CHR/Software.html [Accessed 22. January 2017].

DURHAM, W. B., KIRBY, S. H., STERN, L. A. & ZHANG, W. 2003. The strength and rheology of methane clathrate hydrate. *Journal of Geophysical Research,* 108**,** 2182.

EL-CAT. n.d. *Properties of silicon and silicon wafers* [Online]. Available: https://www.el-cat.com/silicon-properties.htm [Accessed 2 May 2017].

ENGLEZOS, P., KALOGERAKIS, N., DHOLABHAI, P. & BISHNOI, P. 1987. Kinetics of Formation of Methane and Ethane Gas Hydrates. *Chemical Engineering Science,* 42**,** 2647-2658.

FLATLANDSMO, J. 2015. *Visualization and interpretation of methane hydrate growth and dissociation in synthetic porous media.* Master's thesis, University of Bergen, Bergen, Norway.

GRAUE, A., KVAMME, B., BALDWIN, B., STEVENS, J., HOWARD, J. J., ASPENES, E., ERSLAND, G., HUSEBO, J. & ZORNES, D. 2008. MRI Visualization of Spontaneous Methane Production From Hydrates in Sandstone Core Plugs When Exposed to CO2. *SPE,* 13**,** 146-152.

HAUGE, L., GAUTEPLASS, J., HØYLAND, M., ERSLAND, G., KOVSCEK, A. & FERNØ, M. 2016. Pore-level hydrate formation mechanisms using realistic rock structures in high-pressure silicon micromodels. *International Journal of Greenhouse Gas Control,* 53**,** 178-186.

HESTER, K. C. & BREWER, P. G. 2009. Clathrate Hydrates in Nature. *Annual Review of Marine Science,* 1**,** 303-327.

HORNBROOK, J., CASTANIER, L. & PETTIT, P. 1991. Observation of Foam/Oil Interactions in a New, High-Resolution Micromodel. *SPE Annual Technical Conference and Exhibition.* Dallas, 6-9 October: SPE.

HUSEBØ, J., ERSLAND, G., GRAUE, A. & KVAMME, B. 2009. Effects of salinity on hydrate stability and implications for storage of CO 2 in natural gas hydrate reservoirs. *Energy Procedia,* 1**,** 3731-3738.

JEFFREY, G. & MCMULLAN, R. 1967. The Clathrate Hydrates. *Progress in Inorganic Chemistry, Volume 8*, 43-108.
JIN, J., KIM, J. W., KANG, C.-S., KIM, J.-A. & EOM, T. B. 2010. Thickness and refractive index measurement of a silicon wafer based on an optical comb. *Optics Express,* 18**,** 18339-18346.
JIN, Y., KONNO, Y. & NAGAO, J. 2012. Growth of Methane Clathrate Hydrates in Porous Media. *Energy & Fuels,* 26**,** 2242-2247.
KASHCHIEV, D. & FIROOZABADI, A. 2003. Induction time in crystallization of gas hydrates. *Journal of Crystal Growth,* 250**,** 499-515.
KATSUKI, D., OHMURA, R., EBINUMA, T. & NARITA, H. 2007. Methane hydrate crystal growth in a porous medium filled with methane-saturated liquid water. *Philosophical Magazine,* 87**,** 1057-1069.
KATSUKI, D., OHMURA, R., EBINUMA, T. & NARITA, H. 2008. Visual observation of dissociation of methane hydrate crystals in a glass micro model: Production and transfer of methane. *Journal of Applied Physics,* 104**,** 083514.
KVAMME, B. Initiation and growth of hydrate. 4th International Conference on Natural Gas Hydrate, Yokohama, Japan, 2002.
KVAMME, B. 2016. *RE: PTEK232: Fundamentals of Natural Gas Hydrates and Practical Implications.*
KVAMME, B., GRAUE, A., BUANES, T., KUZNETSOVA, T. & ERSLAND, G. 2007. Storage of CO 2 in natural gas hydrate reservoirs and the effect of hydrate as an extra sealing in cold aquifers. *International Journal of Greenhouse Gas Control,* 1**,** 236-246.
KVENVOLDEN, K. A. 1988. Methane hydrate—A major reservoir of carbon in the shallow geosphere? *Chemical Geology,* 71**,** 41-51.
LILLESTØL, E., HUNDERI, O. & LIEN, J. R. 2001. *Generell fysikk for universiteter og høgskoler,* Oslo, Universitetsforlaget.
MAKOGON, Y. F. 2010. Natural gas hydrates–A promising source of energy. *Journal of Natural Gas Science and Engineering,* 2**,** 49-59.
MORIDIS, G. & COLLETT, T. 2003. Strategies for Gas Production from Hydrate Accumulations Under Various Geologic Conditions. *TOUGH Symposium 2003.* Berkeley, California, 12-14 May.
MORIDIS, G. J. 2011. Challenges, Uncertainties and Issues Facing Gas Production From Gas Hydrate Deposits. *SPE Reservoir Evaluation and Engineering,* 14**,** 76-112.
NOTHNAGLE, P. E., CHAMBERS, W., FELLERS, T. J. & DAVIDSON, M. W. 2016. *Reflected (Episcopic) Light Illumination* [Online]. Nikon MicroscopyU. Available: https://www.microscopyu.com/techniques/stereomicroscopy/reflected-episcopic-light-illumination [Accessed 24. April 2017].
OHMURA, R., MATSUDA, S., UCHIDA, T., EBINUMA, T. & NARITA, H. 2005. Clathrate Hydrate Crystal Growth in Liquid Water Saturated with a Guest Substance: Observations in a Methane + Water System. *Crystal Growth & Design,* 5**,** 953-957.
OHMURA, R., OGAWA, M., YASUOKA, K. & MORI, Y. H. 2003. Statistical Study of Clathrate-Hydrate Nucleation in a Water/Hydrochlorofluorocarbon System: Search for the Nature of the "Memory Effect". *The Journal of Physical Chemistry B,* 107**,** 5289-5293.
OHMURA, R., SHIMADA, W., UCHIDA, T., MORI, Y. H., TAKEYA, S., NAGAO, J., MINAGAWA, H., EBINUMA, T. & NARITA, H. 2004. Clathrate hydrate crystal growth in liquid water saturated with a hydrate-forming substance: variations in crystal morphology. *Philosophical Magazine,* 84**,** 1-16.
POLYANSKIY, M. 2016. *Optical Constans of HIKARI - BK (Borosilicate Crown)* [Online]. Available: https://refractiveindex.info/?shelf=glass&book=HIKARI-BK&page=J-BK7A [Accessed 30 April 2017].
REES, E. V., KNEAFSEY, T. J. & SEOL, Y. 2011. Methane Hydrate Distribution from Prolonged and Repeated Formation in Natural and Compacted Sand Samples: X-Ray CT Observations. *Journal of Geological Research,* 2011.
RIPMEESTER, J. A. 2000. Hydrate Research-From Correlations to a Knowledge-based Discipline: The Importance of Structure. *Annals of the New york Academy of Sciences,* 912**,** 1-16.

RUPPEL, C. 2011. Methane Hydrates and the Future of Natural Gas. *MITEI Natural Gas Report, Supplementary Paper on Methane Hydrates,* 4**,** 25.

SLOAN, E. D. 2003. Fundamental principles and applications of natural gas hydrates. *Nature,* 426**,** 353-363.

SLOAN, E. D. K., C. A. 2008. *Clathrate Hydrates of Natural Gases,* 3rd ed. United States of America, Taylor & Francis Group.

STILLINGER, F. H. 1980. Water Revisited. *Science,* 209**,** 451-457.

THE ENGINEERING TOOLBOX. n.d. *Refractive Index for Some Common Liquids, Solids and Gases* [Online]. Available: http://www.engineeringtoolbox.com/refractive-index-d_1264.html [Accessed 30 April 2017].

TOHIDI, B., ANDERSON, R., CLENNELL, M. B., BURGASS, R. W. & BIDERKAB, A. B. 2001. Visual observation of gas-hydrate formation and dissociation in synthetic porous media by means of glass micromodels. *Geology,* 29**,** 867-870.

TURNER, D. J., CHERRY, R. S. & SLOAN, E. D. 2005. Sensitivity of methane hydrate phase equilibria to sediment pore size. *Fluid Phase Equilibria,* 228**,** 505-510.

UCHIDA, T., TAKEYA, S., CHUVILIN, E. M., OHMURA, R., NAGAO, J., YAKUSHEV, V. S., ISTOMIN, V. A., MINAGAWA, H., EBINUMA, T. & NARITA, H. 2004. Decomposition of methane hydrates in sand, sandstone, clays, and glass beads. *Journal of Geophysical Research,* 109**,** 1-12.

U.S. ENERGY INFORMATION ADMINISTRATION. 2016. *International Energy Outlook 2016* [Online]. U.S. Energy Informaiton Administration. Available: https://www.eia.gov/outlooks/ieo/world.cfm [Accessed 21. March 2017].

VON STACKELBERG, M. 1956. Die Struktur der Einschlussverbindungen des Wassers (Gashydrate) und des Phenols. *Recueil des Travaux Chimiques des Pays-Bas,* 75**,** 902-905.

WORDPRESS. 2011. *Water; Non Cocalent Bonds; Hydrogen Bonds & Hydrophobic Interactions* [Online]. Available: https://learnbiochemistry.wordpress.com/category/hydrogen-bond/ [Accessed 18 January 2017].

WU, Q. & ZHANG, B. 2010. Memory effect on the pressure-temperature condition and induction time of gas hydrate nucleation. *Journal of Natural Gas Chemistry,* 19**,** 446-451.